Universität Bremen

marum
Zentrum für Marine Umweltwissenschaften

# Hydrocarbon Seepage at Campeche-Sigsbee Salt Province, Southern Gulf of Mexico

## Detection, Mapping, and Seafloor Manifestation

Dissertation
zur Erlangung des
Doktorgrades der Naturwissenschaften
Doctor rerum naturalium
(Dr. rer. nat.)
am Fachbereich Geowissenschaften
der Universität Bremen

vorgelegt von
**Chieh-Wei Hsu**

Bremen, November 2019

**Gutachter**

Prof. Dr. Gerhard Bohrmann
Universität Bremen
MARUM – Zentrum für Marine Umweltwissenschaften
Klagenfurter Straße 4
28359 Bremen, Deutschland

Dr. habil. Ingo Klaucke
GEOMAR | Helmholtz-Zentrum für Ozeanforschung Kiel
Gebäude 8/C, Ostufer
Wischhofstraße 1-3
24148 Kiel, Deutschland

Datum des Kolloquiums: 19 Dezember 2019

# Preface

The Gulf of Mexico (GoM) is one of the most important prolific oil-producing regions. Therefore it has attracted attention and interest not only from industry but also from scientists to investigate and understand its nature. Due to technical limitations, efficiency, and cost considerations, there is a lack of extensive research in deeper areas such as the central and southern Gulf of Mexico. The submarine asphalt volcanism has been an object of research since it was first discovered in 2003 at “Chapopote Knoll” in the southern Gulf of Mexico during the cruise R/V SONNE 174. In the wake of the Deepwater Horizon incident 2010, which was the world’s first and largest deep water well blowout, scientific research within the deep GoM was much more intensified. In the context of the accident, occurrences of larger hydrocarbon deposits like the asphalt accumulation, their retention on the seabed and their interaction with the environment are of great interest, became the driving force for leading and attracting us to explore this area.

Research cruise M114 of R/V METEOR (from 12 February to 28 March 2015) has surveyed roughly 33,500 $km^2$ of the southern Gulf of Mexico. This successful cruise brought fruitful results and hence initiated this PhD study. These results provide the first direct evidence for the occurrences of widespread gas emission sites in the Campeche-Sigsbee salt province. By analyzing the hydroacoustic data and the visual seafloor observations obtained from this cruise and integrating the datasets from previous studies, we provide a better understanding of the hydrocarbon seepage in this study area. The investigations at Challenger Knoll revealed both, the occurrence of gas bubble emissions and living chemosynthetic communities at the seafloor. Extensive asphalt deposits have been investigated in detail at the so-called Mictlan Knoll, which is considered to yield even larger areas covered by asphalt deposits than Chapopote Knoll in the southern Gulf of Mexico.

This cumulative PhD thesis was written at the Department of Geosciences at the University of Bremen in Germany. The work has been carried out from December 2014 until October 2019. My PhD was supported by a scholarship from the Deutscher Akademischer Austausch Dienst (DAAD) (program ID: 57048249). The research cruise M114 and the PhD project was funded by the German Research Foundation (DFG – Deutsche Forschungsgemeinschaft) through the proposal “Hydrocarbons in the southern Gulf of Mexico“. Additional funding was provided through the DFG-Research Center/Excellence Cluster “The Ocean in the Earth System”.

# Table of Contents

# Table of Abbreviations

| | |
|---|---|
| ASSMO | Autonomous Scanning Sonar Module |
| AUV | Autonomous Underwater Vehicle |
| CTD | Conductivity, Temperature, Depth (indicative for Pressure) |
| DAAD | Deutscher Akademischer Austausch Dienst |
| DFG | Deutsche Forschungsgemeinschaft |
| DSDP | Deep Sea Drilling Project |
| GBS | Gas Bubble Sampler |
| GEBCO | General Bathymetric Chart of the Oceans |
| GH | Gas Hydrate |
| GHSZ | Gas Hydrate Stability Zone |
| GoM | Gulf of Mexico |
| MBES | Multibeam Echosounder |
| mbsf | Meters Below Seafloor |
| mbsl | Meters Below Sea Level |
| MV/MVs | Mud Volcano/-es |
| P-T | Pressure / Temperature |
| ROV | Remotely Operated Vehicle |
| SAR | Synthetic Aperture Radar |
| SMTZ | Sulfate-Methane Transition Zone |
| TAMOC | Texas A&M Oil spill Calculator |
| USBL | Ultra Short Base Line |
| VTLC | Video Time-Lapse Camera |

## Abstract

Hydrocarbon seepage is a process during which hydrocarbon fluids are emitted from the seafloor into the water column. This phenomenon has been observed globally from continental margins to the deep abyssal. Hydrocarbon seepage has significant impacts on the marine environment such as (a) influence on sediment composition and dynamics at the seafloor, (b) increasing the habitat heterogeneity on seep biodiversity and (c) contributes to the global carbon cycle. However, the occurrence, distribution, and dynamics of hydrocarbon seepage in the marine environment, especially in the deep ocean remains unclear due to limited investigation.

The northern Gulf of Mexico is a well-known prolific petroleum-producing region where numerous gas and oil emissions, associated with salt tectonism, have been observed. The Campeche-Sigsbee salt province in the southern GoM is considered to be an analog to the salt province in the northern GoM, but there has been very little research conducted in this region. Based on the occurrence of natural oil slicks on the sea surface resolved by satellite images, previous studies suggested that there is a widespread distribution of oil seeps in the Campeche-Sigsbee salt province. However, there is still a lack of direct evidence for the presence and the distribution of gas emissions. In addition to gas and oil seepage, Chapopote asphalt volcanism, a novel type of hydrocarbon seepage was first introduced in 2003. Since then, submarine asphalt deposits have attracted considerable research interest.

This study aims to have a comprehensive understanding of the hydrocarbon seepage system and dynamics in the southern GoM. The objectives are to investigate the distribution of gas emissions and to understand the controlling factors on the distribution. Furthermore, detailed investigations were carried out at Challenger Knoll and Mictlan Knoll to gain a better understanding of the diverse hydrocarbon seepage system including gas and oil emissions, as well as asphalt deposits. Consequently, the research questions about the fate of the methane bubbles and the quantity of gas bubble released from gas emission site are finally addressed in this study.

During research cruise M114 of R/V METEOR, a multidisciplinary approach was conducted, including hydroacoustic surveys, visual seafloor observations, and sampling of gas bubbles. Ship-based multibeam echosounder was used for seafloor bathymetry, backscatter and water column flare mapping in the Campeche-Sigsbee salt province. In addition, multibeam echosounder mounted on Autonomous Underwater Vehicle (AUV) was utilized to obtain high-resolution seafloor bathymetry, backscatter, and water column data at Mictlan Knoll. Remotely Operated Vehicle (ROV) and TV-sled were applied for investigating and documenting seafloor manifestations of hydrocarbon seepage at the seafloor. Gas bubbles were collected by pressure-tight gas bubble samplers operated by ROV at the seafloor of Mictlan Knoll for gas analyses, quantification of gas bubble emissions, and finally gas flux calculation.

The first study focuses on the distribution of gas emission sites associated with geological features in the Campeche-Sigsbee salt province. According to the seafloor morphology, more than 40 individual seafloor features were categorized into four principle structure types. A total of 202 individual flares were observed in the study area, providing the first direct evidence for widespread gas emissions in the southern GoM. The distribution patterns of gas emissions at the seafloor were found to be associated with the present geological features and a schematic gas migration model has been introduced to interpret the geological and structural controls on

the distribution of gas emissions. Moreover, none of the gas bubbles emissions reached the sea surface based on our water column imaging, indicating that a direct contribution of methane from the rising bubbles to the atmosphere is insignificant in the southern GoM.

The second study aims to investigate the characteristics of hydrocarbon seepage detected at knolls located in the Sigsbee Knolls area. Flares in the water column have been detected at three flat-top knolls associated with salt diapirism including Challenger Knoll, knolls H2327 and H2320. Gas emission sites are exclusively located near the edges of the knolls, inferring that the edges of salt diapirs might provide effective fluid migration pathways. Visual seafloor observations conducted with a TV-sled are used to investigate the seafloor manifestations of the seep sites at Challenger Knoll. The occurrence of chemosynthetic fauna at the seafloor indicate that dissolved methane was present in shallow sediment close to the area where also flares have been documented to be sourced at the seafloor. Oil slicks on the sea surface were observed in 2002, however, in this study, neither satellite imagery nor ship-based observation detected floating oil, which suggests that oil seepage in this area occurs intermittently.

The third study focuses on the diverse hydrocarbon seepage at a knoll called Mictlan Knoll, which was documented to be associated with asphalt volcanism. The seafloor structure of Mictlan Knoll is characterized by a distinct crater-like depression at its top. The micro-structures and accurate flare locations were mapped and characterized based on AUV-driven multibeam echosounder. The flares are distributed around the crater-like depression at Mictlan Knoll, which is similar to the findings at Chapopote Knoll. Extensive asphalt deposits covering several hundreds of square meters are observed by visual seafloor observation in the northeastern part of the depression. Within this extensive asphalt area, various facies of asphalt deposits including fresh asphalt deposits, weathered asphalt, asphalt flow structures as well as recently emitted oil seeps were observed visually and mapped in detail. TV-sled surveys were used to investigate asphalt deposits across the entire depression. Based on the visual seafloor observation associated with changing backscatter intensity we suggest that Mictlan Knoll hosts the largest area of extensive asphalt deposits known so far in the GoM.

In summary, gas emissions are found in large numbers in the Campeche-Sigsbee salt province. Their distributions are controlled by the present geological structures. The case study in the Sigsbee Knolls suggests that the edges of flat-top knolls might provide an effective migration pathway for hydrocarbons. As there is no direct evidence for the presence of current oil seepage in the Sigsbee Knolls, we suggested that oil seepage occurs intermittently. Gas, oil seepage and asphalt volcanism are found to occur close together at the Mictlan Knoll, indicating that this diverse hydrocarbon seepage system might be a common phenomenon in the Campeche Knolls. This thesis shows the complex association between the dynamics of diverse hydrocarbon seepage and the geological controls in the southern GoM.

## Outline and contributions to manuscripts

The focus of this cumulative thesis is to characterize the hydrocarbon seepage in the Campeche-Sigsbee salt province in the southern GoM by using high-resolution seafloor mapping, water column flares mapping as well as visual seafloor observations.

The thesis is divided into seven chapters. Chapter 1 introduces the general concepts of marine cold seeps as well as their seafloor manifestation and summarizes the methods conducted for investigating seeps in this work. Chapter 2 summarizes the current scientific questions and the knowledge gaps that illustrate the motivation for this study. Chapter 3 provides an overview of the Campeche-Sigsbee salt province, including regional setting, formation, deformation, and sedimentation history as well as hydrocarbon seepage in this area. The following three chapters are the essence of this thesis and composed of three manuscripts. The first manuscript (Chapter 4) highlights the occurrence and distribution of widespread gas emissions associated with the seafloor morphologies in the Campeche-Sigsbee salt province. The second manuscript (Chapter 5) focuses on the characteristic oil and gas emissions at Challenger Knoll, and describes the deepest gas emission areas known from the GoM. A case study at Mictlan Knoll is presented in the third manuscript (Chapter 6), investigating detailed seafloor manifestations of diverse hydrocarbon seeps in an area of the extensive asphalt deposits. Chapter 7 provides an overall conclusion and summarizes the research outlook followed by the reference list and acknowledgment.

Chieh-Wei Hsu is the principal author of this cumulative thesis and designed all three manuscripts, which have been discussed and commented by several co-authors. The co-authors of the respective manuscripts and their contributions are listed below.

**Manuscript I: Widespread distribution of gas emissions at the Campeche and Sigsbee Knolls, Southern Gulf of Mexico**

| Author name | Statement of contribution |
|---|---|
| Chieh-Wei Hsu | The principal author of this manuscript and responsible for producing all figures; analyzing and integrating all data, designing and drafting the manuscript. |
| Miriam Römer | Hydroacoustic surveys, water column data analysis, involved in planning and supervised the study, provided critical feedback and helped shaping the manuscript |
| Ian MacDonald | SAR imaging and analysis, and helped shaping the manuscript |
| Markus Loher | Water column analysis, provided critical feedback and helped shaping the manuscript |
| Thomas Pape | Interpretation of the geochemical data (gas composition, stable carbon and hydrogen isotope ratios) provided critical feedback and helped shaping the manuscript |
| Paul Wintersteller | Hydroacoustic survey planning and processing of bathymetry data |

| | |
|---|---|
| Gerhard Bohrmann | Chief scientist of the cruise M114-2, contributed to the design and implementation of the research |

**Manuscript II: Hydrocarbon seepage at the Challenger Knoll in the Sigsbee basin, Gulf of Mexico**

| **Author name** | **Statement of contribution** |
|---|---|
| Chieh-Wei Hsu | The principal author of this manuscript and responsible for producing all figures; designing and drafting the manuscript; water column data analysis, seafloor image analysis |
| Ian MacDonald | Oil seepage analysis, visual seafloor investigation (VTLC), involved in planning and supervised the study, provided critical feedback and helped shaping the manuscript |
| Miriam Römer | Hydroacoustic surveys, sub-bottom profiling, helped shaping the manuscript; advising of water column flare mapping |
| Thomas Pape | Provided critical feedback and helped shaping the manuscript |
| Heiko Sahling | TV-sled surveys, contributed to the design and implementation of the research |
| Paul Wintersteller | Processing of bathymetry data and seafloor images, provided the sub-bottom data |
| Gerhard Bohrmann | Chief scientist of cruise M114-2, contributed to the design and implementation of the research |

**Manuscript III: Diversified hydrocarbon seepage at Mictlan asphalt volcano, southern Gulf of Mexico**

| Author name | Statement of contribution |
|---|---|
| Chieh-Wei Hsu | The principal author of this manuscript and responsible for producing all figures; designing and drafting the manuscript; seafloor images analysis, water cloumn flare mapping. |
| Yann Marcon | Involved in planning and supervised the study, mosaic processing and assembling, ROV-dive planning and helped shaping the manuscript |
| Miriam Römer | Involved in planning and supervised the study, ROV-dive planning, AUV flare mapping; provided critical feedback and helped shaping the manuscript |
| Paul Wintersteller | Processing of ship-based and AUV derived bathymetry and seafloor backscatter data, |
| Thomas Pape | Interpretation of the geochemical data (gas composition, stable carbon and hydrogen isotope ratios) provided critical feedback and helped shaping the manuscript |
| Ian MacDonald | Oil seepage analysis, visual seafloor investigation (VTLC), provided critical feedback and helped shaping the manuscript |
| Markus Loher | Water column flare mapping, mosaic processing and assembling |
| Christian Ferreira | Processing of AUV derived bathymetry and seafloor backscatter data, |
| Gerhard Bohrmann | Chief scientist of the cruise M114-2, contributed to the design and implementation of the research |

# 1. Introduction

## 1.1. Marine cold seeps

Marine cold seeps are geological structures characterized by focused fluid flow, which is considered as the product of highly vertical, nearly instantaneous, and relatively fast release of basin fluids and sediments (see e.g. reviews by Andresen 2012; Berndt 2005; Cartwright et al. 2007). Compared to hydrothermal vents, the emissions at cold seeps generally flow more slowly, so they are usually adjusted to ambient temperatures. However, if flowing more vigorously, they do have elevated temperatures (Suess 2018). Cold seeps are typically characterized by the occurences of authigenic carbonate deposits and host oasis-type ecosystems (Bohrmann et al. 1998; Hovland et al. 1987; Naehr et al. 2009; Paull et al. 1984; Sahling et al. 2002). They are distributed along active margins associated with plate convergent boundary, as well as strike-slip faulting and at passive margins associated with differential compaction as well as sediment loading (Fig. 1.1) (Suess 2018).

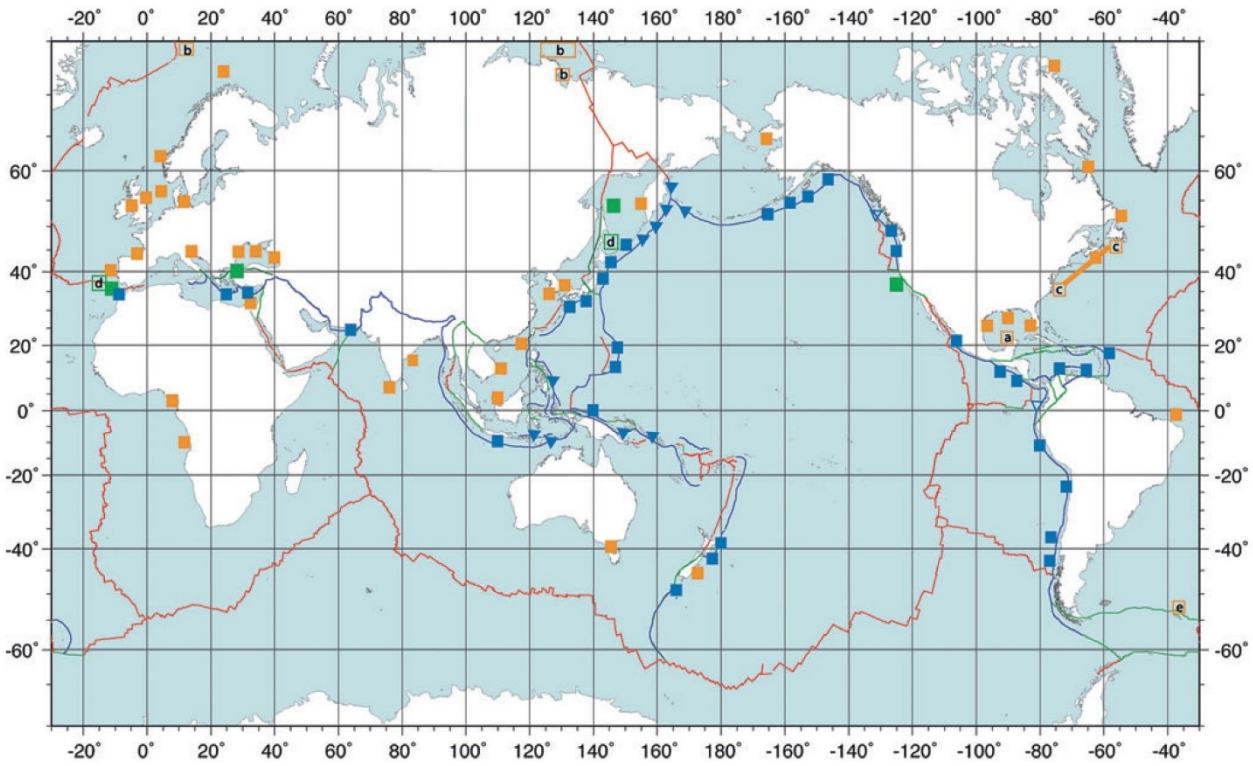


Fig. 1.1. Global marine cold seeps distribution; locations with hydrocarbon-metazoan-microbe-carbonate associations (■); Groundwater seeps (■); transform and strike-slip faults (■). Recently observed sites (□): (a) asphalt volcanos in the southern GoM (Sahling et al. 2016); (b) East Siberian Shelf (Shakhova et al. 2015) and Svalbard margin; (c) Atlantic margin (Skarke et al. 2014); (d) Sakhalin strike-slip faulting (Derkachev et al. 2015) and Africa-Eurasia strike-slip (Hensen et al. 2015); (e) South Georgia Island fjords (Römer et al. 2014b). (from Suess (2018))

Fluids released at cold seeps include various types: liquid and gaseous, organic and inorganic, which derive from geological processes, biogeochemical reactions and biological activities (Judd and Hovland 2009). For example, on passive margins (Fig. 1.2), the nature as well as the thickness of the accumulating sediments determine the types of seepage. Manifestations at the seafloor also vary strongly and include mud volcanoes, pockmarks, gas hydrate mounds, salt diapirs, authigenic carbonates and asphalt volcanoes (Bohrmann et al. 2003; MacDonald et al. 2004; Moore 1999; Pape et al. 2011; Suess 2014). At passive margin, the fluid expulsion is driven by differential compaction, sediment loading, overpressure, and facies changes (Suess 2014). Fluid migration pathways can occur at any permeability change in the strata involving fluid-rich strata, ash layers, turbidities, sands and silts, drifting sediments, as well as buried reefs intersecting faults (Suess 2018). Other forces driving the fluid flow are free or dissolved gas movement due to their buoyancy (Matthews 1996), tidal and hydrological pumping (Römer et al. 2016), and thermally driven circulation (Shakhova et al. 2015).

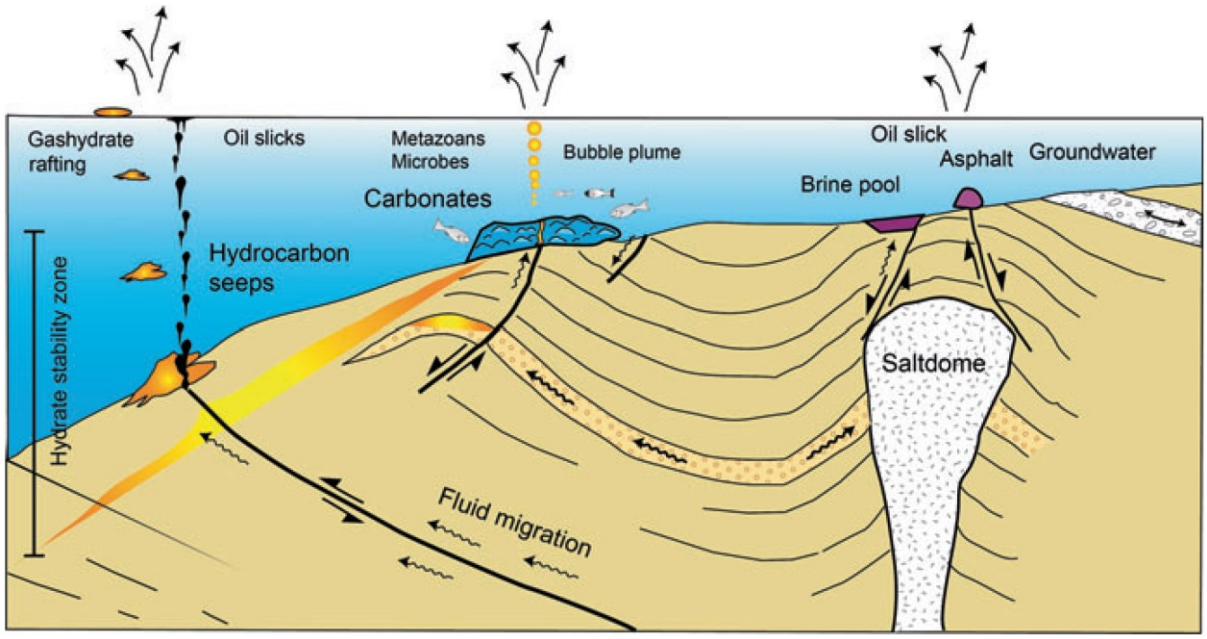


Fig. 1.2. Seeps at a passive margin; geologic settings and driving forces for fluid expulsion lead to form different types of seepage; Carbonates, asphalt deposits, gas hydrate mounds, and gas bubble and oil droplets in the water column are common manifestations of cold seeps (modified from (Suess 2018)).

## 1.2. Types of hydrocarbon seepage

### 1.2.1. Gas bubble emissions

Gas bubble release from the seafloor into the water column (or commonly termed as gas bubble emissions) have been documented at numerous locations globally from continental shelves to abyssal depths (Judd and Hovland 2009). The emitted gases can comprise various hydrocarbon compounds as well as $CO_2$, $N_2$, and $H_2S$. However, gas emissions are mostly composed of methane due to the fact that methane is the most abundant hydrocarbon compound in the marine environment (Kvenvolden and Rogers 2005). Since methane represents a potent greenhouse gas, several studies have been conducted to understand its sources and sinks (IPCC 2013).

Gas emissions can occur in various geological settings where over-pressure in the sediments controls the emission of fluids enriched in methane or other hydrocarbons to the seafloor and hydrosphere (Suess 2014). These gas emissions are associated with different geological features such as gas hydrates, pockmarks, salt diapirs and mud volcanoes (MVs) (Loher et al. 2018a; MacDonald et al. 2002; Marcon et al. 2014; Suess et al. 2001). Most of the studies on gas emissions were conducted in shallow waters (Fleischer et al. 2001) because they are relatively easy to access and several sites have been quantified for the amount of emitting gas entering in to the water column (Hornafius et al. 1999; Hovland et al. 1993; Schneider von Deimling et al. 2011). However, with rapid advancement in sonar technology as well as in underwater instruments in recent years, there has been a growing number of publications focusing on the gas emissions in deep-waters, e.g. in the Black Sea (Römer et al. 2012a; Sahling et al. 2009), the Gulf of Mexico (Leifer and MacDonald 2003; Weber et al. 2014), the Makran continental margin (Römer et al. 2012b), off the west Svalbard margin at Vestnesa Ridge (Bünz et al. 2012) as well as Hydrate Ridge (Torres et al. 2002).

It is well known that gas production involves basic biogeochemical processes. In marine sediments methane is generated predominantly by two process (e.g. summarized by Claypool and Kaplan 1974; Hovland et al. 1993): (i) generation of methane by methanogenic archaea at low temperatures (~< 80°C), which is known as ‘biogenic’ methane; and (ii) through the decomposition or breakdown of organic molecules at high temperatures which may exceed 150°C, termed ‘thermogenic’ methane (Claypool and Kvenvolden 1983; Stolper et al. 2014). Gas of predominantly biogenic origin is considered to constitute more than 20% of the world's natural gas reserves (Claypool and Kvenvolden 1983; Rice and Claypool 1981). The biogenic methane formation in marine sediment is from methanogenic archaea utilizing fermentative end products such as $CO_2$ along with hydrogen (Equation 1-1) or acetate (Equation 1-2). The geological conditions that favor significant generation and accumulation of biogenic gas in the sediment are anoxic and sulfate-deficient environment, low temperature, and the availability of organic matter (Rice and Claypool 1981).

$$CO_2 + 4H_2 \rightarrow CH_4 + 2H_2O \quad \text{(Eq. 1-1)}$$

$$CH_3COO^- + H^+ \rightarrow CH_4 + CO_2 \quad \text{(Eq. 1-2)}$$

In general, thermogenic hydrocarbons are produced at greater depths and temperatures in deep anoxic sediment that may exceed 2 km (Floodgate and Judd 1992). The types of hydrocarbon (including methane) generation depends upon the nature of the original organic matter from which it is derived. For example, thermogenic methane can be formed by the thermal degradation of oil and the maturation of coal (see e.g. Galimov 1988; Hovland et al. 1993).

Thermogenic and biogenic gases can be distinguished using stable carbon ($\delta^{13}C$) and hydrogen ($\delta D$) isotope compositions combined with the molecular ratio of methane ($C_1$) to higher hydrocarbons ($C_{2+}$) (Bernard et al. 1976; Pape et al. 2010; Schoell 1988; Stolper et al. 2015; Whiticar 1999). For instance, the activity of microbial methane production is associated with a kinetic isotope effect, which discriminates against $^{13}C$, and thus the lighter $^{12}C$ is preferentially consumed and causes to more depleted $\delta^{13}C$ of the produced methane. To characterize the source of methane, models are based on cross-plots of $\delta^{13}C\text{-}CH_4$ versus $C_1/C_{2+}$ (Bernard et al. 1976) and $\delta^{13}C\text{-}CH_4$ versus $\delta D\text{-}CH_4$ (Whiticar 1999) as shown in Fig. 1.3. According to these diagrams, biogenic methane is characterized by $C_1/C_{2+}$ ratios >1000, $\delta^{13}C\text{-}CH_4$ values < -60‰, and $\delta D\text{-}CH_4$ values from -170‰ to -250‰ for methane production within the marine sediments. The thermogenic methane is characterized by relatively low $C_1/C_{2+}$ ratios <100, with less depletion of $\delta^{13}C\text{-}CH_4$ (>-50‰) as well as $\delta D\text{-}CH_4$ values >-170‰.

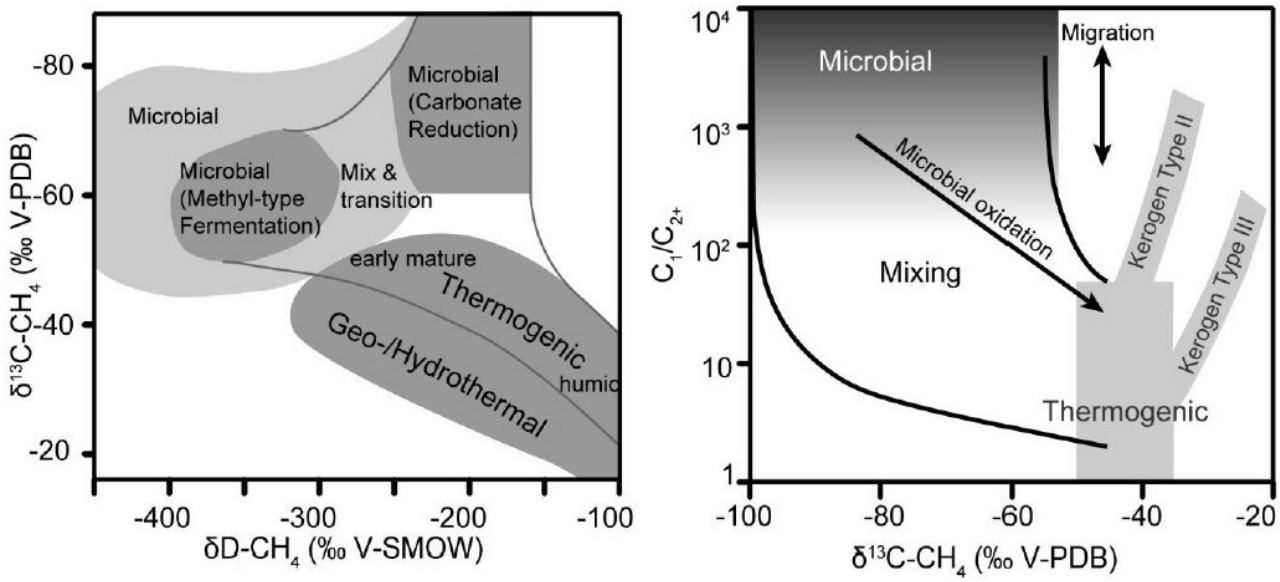


Fig. 1.3. Left: Stable Carbon-hydrogen isotope diagram for classification of biogenic and thermogenic methane (modified after Whiticar (1999)); Right: "Bernard" diagram for classification of hydrocarbon gas are based on $\delta^{13}C\text{-}CH_4$ values and $C_1/C_{2+}$ ratios with theoretical mixing lines and relative compositional effects of oxidation as well as migration (modified after Whiticar (1999)).

Gas migration or accumulation are two major processes after its formation in the sediment. Gas may be present in solution in the pore water (under saturated), or as free gas bubbles (saturated). The gas transport direction is usually vertical (upwards or toward the seafloor) as the primary driving force for gas movement is the buoyancy based on the differences in density between gas and water (Khilyuk et al. 2000; Matthews 1996). The pressure decrease during upward migration may cause dissolved gas to come out of solution to form free gas bubbles. Free gas is strongly buoyant and overpressure at depth may provide an additional driver for its migration (Clennell et al. 2000). Gas can also migrate within the sediment via conduits, such as porous and permeable stratigraphic sediment layers, fault zones, and mud diapirs (Judd and Hovland 2009; Moore and Vrolijk 1992), or by geomorphologically focused flow (Naudts et al. 2006; Orange and Breen 1992). Although some gas may escape through the seafloor forming gas seeps, the majority will be trapped on its way up to form natural gas reservoirs.

### 1.2.2. Oil seeps

Oil slicks at the sea surface may result from natural oil seeps at the seafloor as well as from human activities such as spill from ships or from oil and gas platforms. Natural seepage of oil contributes nearly half of the entire oil input to the ocean (Kvenvolden and Cooper 2003). Oil seeps are known to occur in clusters globally from the continental shelves (Allen et al. 1970; Vis 2017) to continental slopes (Garcia-Pineda et al. 2010; Kennicutt II et al. 1988; Körber et al. 2014) and deep basins (Didyk and Simoneit 1989; MacDonald et al. 2015; Williams et al. 2006). The annual global oil seepage rate was estimated to be 600,000 metric tons, with a uncertainty range from 200,000 to 2,000,000 metric tons per year (Kvenvolden and Cooper 2003; NAS 2003). This estimation was based on global surveys and extrapolations from the seepage quantified at a few known sites.

Natural oil seeps and associated fluid emissions have a significant influence on the composition of the oceans and atmosphere and may support chemosynthetic communities at the seafloor (Judd and Hovland 2009; Valentine et al. 2010). Oil and gases from the oil reservoir flow upward through conduits (e.g. faults and cracks) within the sediment forming different types of oil seeps at the seafloor (Fig. 1.4). Released heavy oil can lead to the formation of submarine asphalt deposits (Brüning et al. 2010) (see Chapter 1.4.5). Light hydrocarbons such as oil droplets may remain or degrade in the water column or further transport through the entire water column and form oil slicks on the sea surface. Lighter petroleum hydrocarbons may evaporate to the atmosphere and heavy petroleum hydrocarbon may return into the water column and further deposit at seafloor (Fig. 1.4).

Since 2 decades, advances in remote sensing technology, for example, the active microwave sensors like Synthetic Aperture Radar (SAR) enable more accurate detection and estimation the amount of natural oil slicks at the sea surface (Brekke and Solberg 2005; De Beukelaer et al. 2003). SAR is a space-borne tool that allows nearly real-time imagery over extensive terrain and marine footprints in areas hundreds of kilometers wide. SAR also enables for continuous observation of the oil discharges process, benefiting from (i) day and night observability, (ii) cloud cover independence and (iii) high revisit frequency. Therefore, the SAR method is the primary tool for assessing the release of intense hydrocarbon discharges, for example in the

Caspian Sea (Ivanov et al. 2007), the NE Atlantic margin (Vis 2017), Offshore Angola (Jatiault et al. 2017), the Black Sea (Körber et al. 2014), and the Gulf of Mexico (Garcia-Pineda et al. 2010; Macdonald et al. 1993).

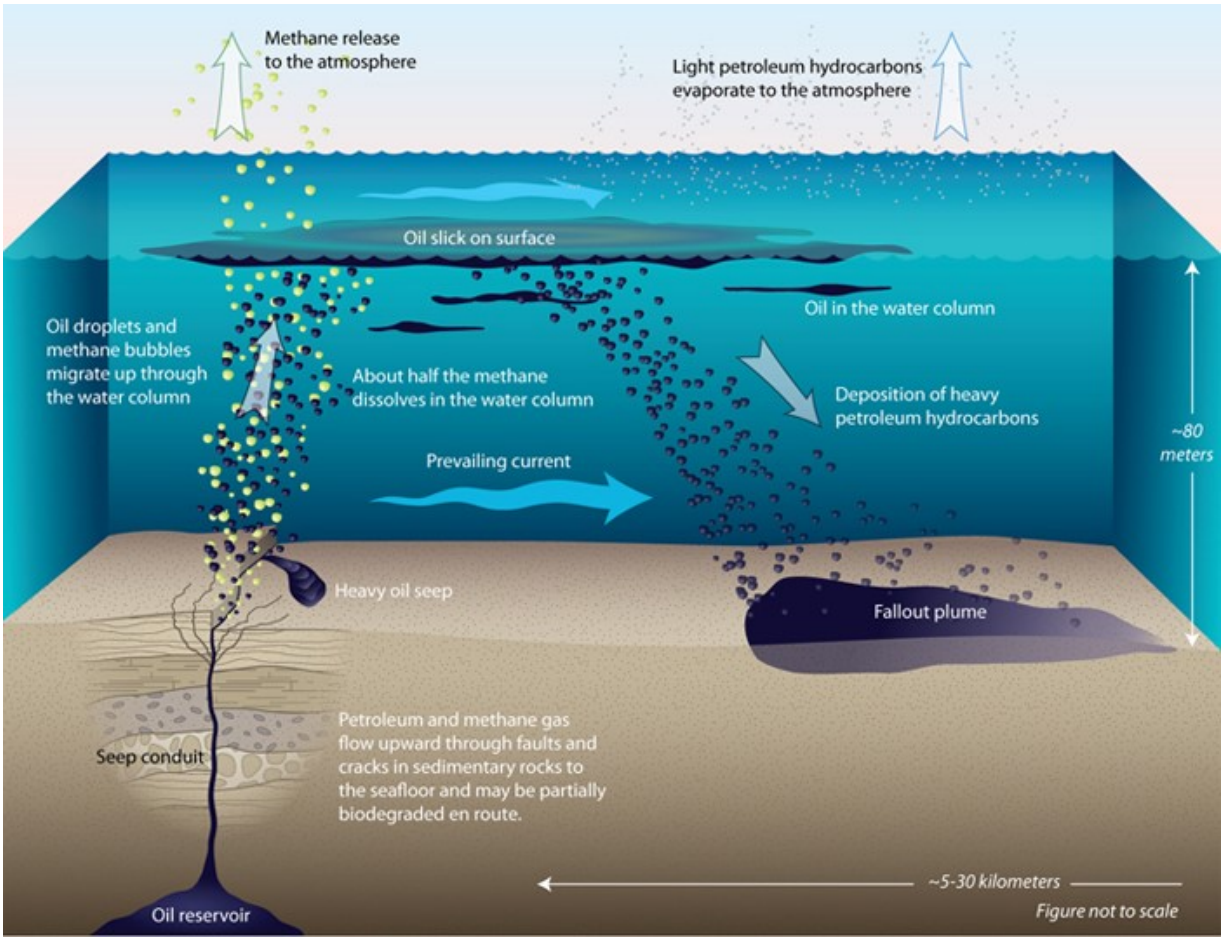


Fig. 1.4. This illustration shows the natural oil seepage in the marine environment (from Cook (2014), Woods Hole Oceanographic Institution).

## 1.3. Gas hydrates

Gas hydrates are naturally occurring solid crystalline compounds (Sloan 1998) comprised of water molecules forming a rigid lattice of cages (also called clathrates) in which each cage contains a gas molecule, most often methane (Fig. 1.5 left). The natural gas hydrate was first discovered in a permafrost region of northern Russia (Makogon et al. 1971), and subsequently found in the sediments of the Caspian Sea and Black Sea (Yefremova and Zhizchenko 1974). Since then, gas hydrates in the marine environment have been studied extensively since it might serve as an important energy resource in the future (Collet and Bardwell 2002; Kvenvolden 1998). Also, understanding the role of gas hydrates and their impact on carbon cycling, climate change, and slope stability has also been attracting considerable interest (Bohrmann and Torres 2006).

Three different hydrate types have been found in nature: Structure I, II and H (Sloan 1998), each is formed by a specific combination of cage types (Fig. 1.5 right). Gas hydrate can contain various types of gas molecules in separate cages, based on the sizes as well as the composition of gases in the forming environment. Structure I gas hydrate is the most commonly found type in marine deposits, and it can only contain small guest molecules such as methane, ethane, $CO_2$ and $H_2S$ (Bohrmann and Torres 2006), due to the size of its cages.

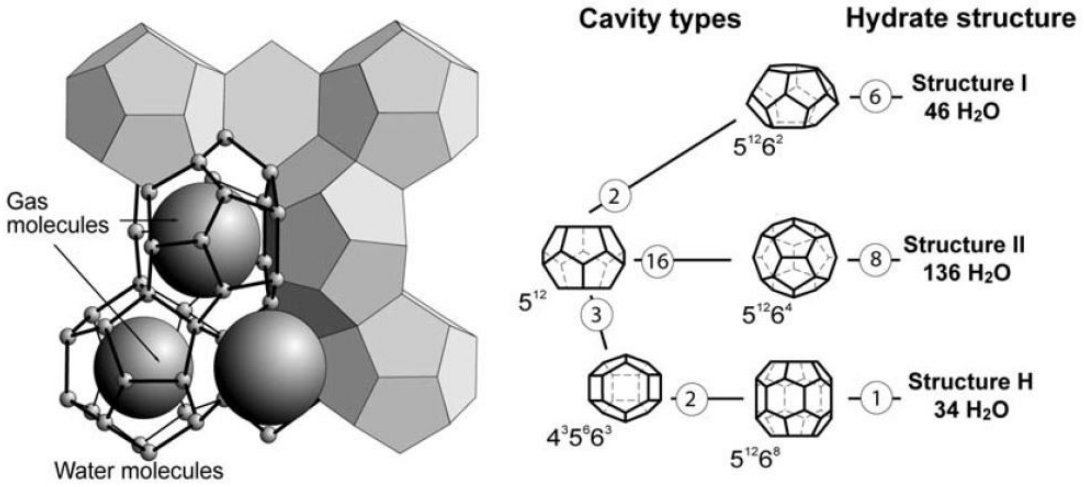


Fig. 1.5. Left: Structure I gas hydrate; small spheres represent water molecules which are forming cages; large spheres represent gas molecules. Right: Three major hydrate crystal structures (I, II and H) are composed of different cage types. The circled numbers indicate that the numbers of the cages are used to form the different hydrate structures. (from Bohrmann and Torres (2006)).

Gas hydrates are formed and preserve only under specific pressure and temperature conditions of the environment, with the availability of appropriate water and gas molecules (Fig. 1.6 left) (Sloan 1998). In the marine environment, gas hydrates are present at continental margins or in the deep sea wherever adequate pressure/temperature (P-T) conditions occur with the over-saturated low weight molecular gases in the sediment (Bohrmann and Torres 2006). The P-T conditions and phase boundary for the presence of pure methane hydrate in the marine environment are shown in Fig.1.6. Intersections of the profiles of the water column

temperature (stippled lines) with the phase boundary (solid line) indicate the gas hydrate stability zone (GHSZ) in the sediments as well as in the water column. The upper boundary of the GHSZ is controlled by the local temperature profile in the water column and the lower boundary of the GHSZ is constrained by the local geothermal gradient in the sediments (Kvenvolden 1993). Other factors such as the salinity of the water column and gas composition also affect the accurate boundaries of the GHSZ.

The thickness of the GHSZ in the marine sediment is fairly constant at the same water depth since the geothermal gradient is generally quite uniform over a broad area below the seafloor (Bohrmann and Torres 2006). However, changes in water depth significantly influence the thickness of the GHSZ in the sediments (Figure 1.6). According to the P-T conditions for hydrate stability, the thickness of the GHSZ can reach 0.8 to 1 km below the seafloor in deepwater regions, and as water depths decrease, the thickness of the GHSZ also gradually decreases (Fig. 1.6).

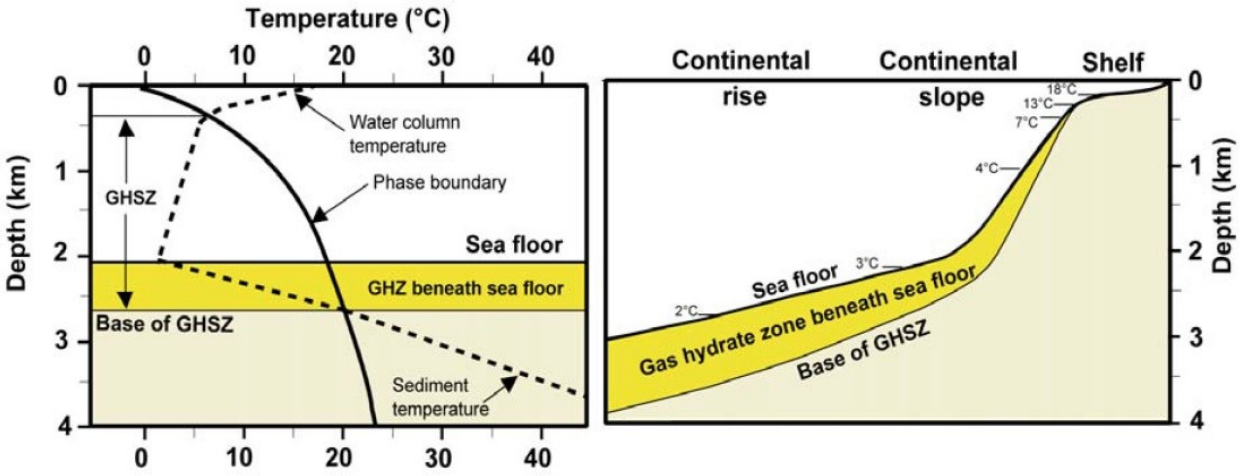


Fig. 1.6. Left: Calculated stability field of gas hydrate (pure methane), as defined by pressure (expressed as water depth) and temperature. Right: Assuming a typical geothermal gradient of 28°C/ km, the inferred thickness of the gas hydrate zone beneath the seafloor at the continental margin is shown. Typical bottom water temperatures are marked, ranging from 2 °C at the bottom of the continental rise to 18° C at the shelf (after Bohrmann and Torres (2006) and Kvenvolden and McMenamin (1980)).

The occurrences of gas hydrate in shallow sediments as well as at the seafloor surface involve the formation and evolution of methane seep systems. For example, formation and dissociation of gas hydrate cause the changes in the pore water chemistry of the surrounding sediment. Slow gas hydrate destabilization in shallow sediments or at the seabed can alter the methane release and provide a stable supply to the ecosystem at cold seeps (Sahling et al. 2002; Suess et al. 2001). Furthermore, gas hydrate growth and dissociation also involve mechanisms to form and shape seafloor morphologies. For example, the dissociation of gas hydrates is associated with the pockmark formation and evolution in deep waters off Nigeria (Sultan et al. 2014; Wei et al. 2015) and the craters and mounds formed in the northern Barents Sea (Andreassen et al. 2017).

## 1.4. Seafloor manifestation of seep sites

### 1.4.1. Mud volcanoes

Mud volcanoes (MVs) are geological structures that are characterized by the surface expressions of cold seeps and the focused upward flow of over-pressured fluids inside hydrocarbon-bearing sedimentary basins (Mazzini and Etiope 2017). The main driving force for the dynamics of MVs is given by a combination of gravitational instability of shales and fluid overpressure (Kopf 2002). MVs are distributed globally both onshore and offshore in tectonically active settings (e.g. accretionary prisms, convergent orogens, thrust belts), deep sedimentary basins and delta regions (Dimitrov 2002; Kopf 2002; Mazzini and Etiope 2017; Milkov 2000).

The seafloor morphologies of MVs vary in size as well as shape and reflect the extrusion rate and intensity of mud breccia accumulated at the seafloor over time (Mazzini and Etiope 2017). Their sizes may range from a square meter up to several square kilometers. The surface structures of MVs can be characterized by their positive morphologies (e.g. cone, dome) or negative (e.g. caldera) morphologies as shown in Fig. 1.7. Although the MVs vary in appearances, Kopf (2002) suggested that they have many common features: (1) they are associated with rapidly deposited, over-pressured, thick argillaceous sequences; (2) the incorporated fragments of underlying rocks and other structural associations; (3) a relationship with regional tectonic and seismic activities or to petroleum reservoirs; and (4) the presence or influx of fluids to facilitate diapiric intrusion and extrusion.

Fig. 1.7. Various morphologies of MVs: (A) conical, (B) elongated, (C) pie-shaped, (D) multicrater, (E)

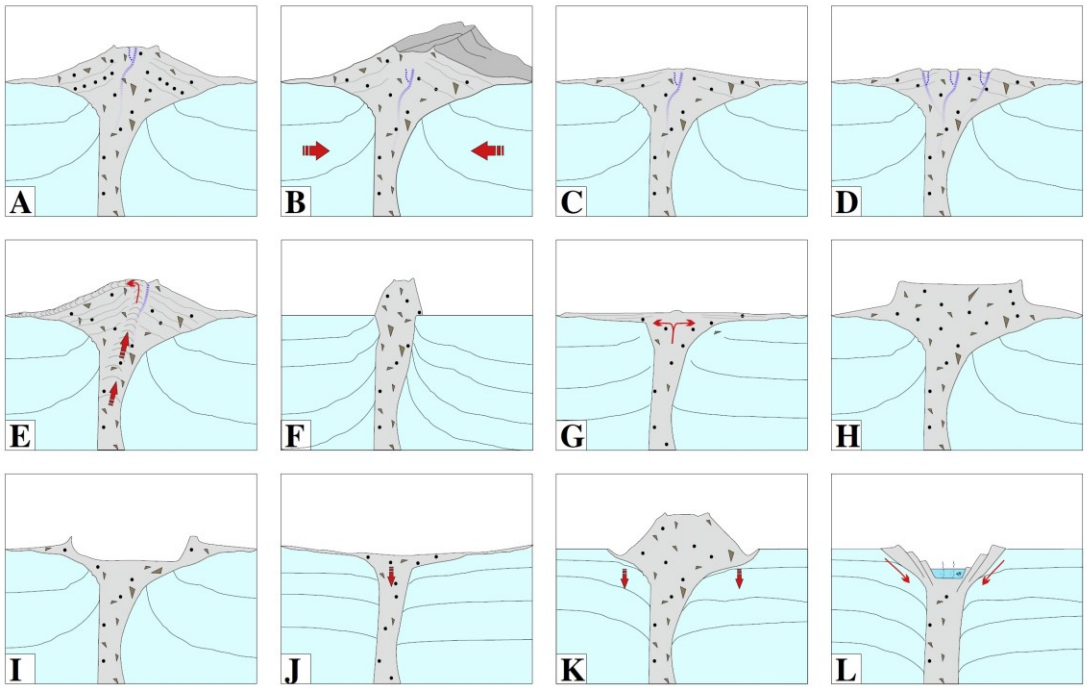


growing diapir-like, (F) stiffneck, (G) swamp-like, (H) plateau-like, (I) impact crater-like, (J) subsiding structure, (K) Subsiding flanks, (L) sink-hole type. (from Mazzini and Etiope (2017))

Submarine MVs are typically developed into pie-shapes with concentric mud breccia ridges (Dupré et al. 2008; Praeg et al. 2009), cone-shapes with single or multiple extrusion locations (Loher et al. 2018c; Paull et al. 2015), and negative or flat morphologies (Graue 2000). Due to the water-saturated conditions (i.e. low viscosity) and the lack of desiccation process, the extruded material of offshore MVs can extend more laterally and flows farther than onshore MVs (Mazzini and Etiope 2017). In addition, the pre-existing local topography may significantly influence the size and morphology of a MV as extruded mud breccia tends to flow along downslope pathways (Graue 2000), and MV flanks can be subject to gravity-induced sedimentary destabilizations (Dupré et al. 2008; Roberts et al. 2011).

Gas escaping from MVs is typically dominated by methane, which may support the MVs to host chemosynthetic communities (Olu-Le Roy et al. 2004), induce authigenic carbonate deposits (Haffert et al. 2013; Loher et al. 2018b) as well as gas hydrate formation (Bohrmann et al. 2003; Sahling et al. 2009) at the seafloor under suitable conditions. The amount of hydrocarbons released by deep sea MVs remains poorly documented, only a few sites have been investigated in detail so far, for example: Håkon Mosby mud volcano (Sauter et al. 2006), Vodyanitskii mud volcano (Sahling et al. 2009) and Venere mud volcano (Loher et al. 2018c). Detailed seafloor mapping and investigation of deep sea MVs are critical to understand the state of their activities and estimate the rate and frequency of extrusions as well as the flux of hydrocarbons released.

### 1.4.2. Pockmarks

Pockmarks are common manifestations of cold seeps and characterized by seafloor depressions connected with the fluids released from the subsurface into the water column (Hovland and Judd 1988; King and MacLean 1970). They can occur where focused fluid flow exists and escapes from low permeability, fine-grained sediments (Hovland and Judd 1988). Pockmarks been found globally in various geological settings, for instance, in the deep sea (Marcon et al. 2014; Sahling et al. 2008a), continental slopes (Macdonald et al. 1990) and shelves (King and MacLean 1970), as well as estuaries (Rogers et al. 2006; Ussler III et al. 2003) and fjords (Forwick et al. 2009).

The morphologies of pockmarks vary widely in shapes and sizes. Hovland et al. (2002) subdivided them into six morphological classes as shown in Fig. 1.8. These seafloor features are controlled by factors such as expulsion fluids process, local conditions as well as regional geological settings. For instance, the orientation of elongated pockmarks is often influenced by bottom currents and surrounding topography (Gontz et al. 2002; Hovland et al. 1984), the “eyed pockmarks” contain coarse material in the central part remaining after erosive processes, including biological activity (skeleton remains, shells, etc.) or from precipitation of authigenic carbonate (Hovland et al. 2002).

Several theories about pockmark formation have been proposed. However, the most common formation mechanism is resulting from erosion by escaping fluid (gas or pore water) and removal of the extrusive sediment by bottom currents (Judd and Hovland 2009). In addition, a number of studies have been suggested that dissociation of gas hydrate can also trigger the formation and evolution of pockmarks in deep waters (Panieri et al. 2017; Roy et al. 2012; Sahling et al. 2008a; Sultan et al. 2014; Wei et al. 2015).

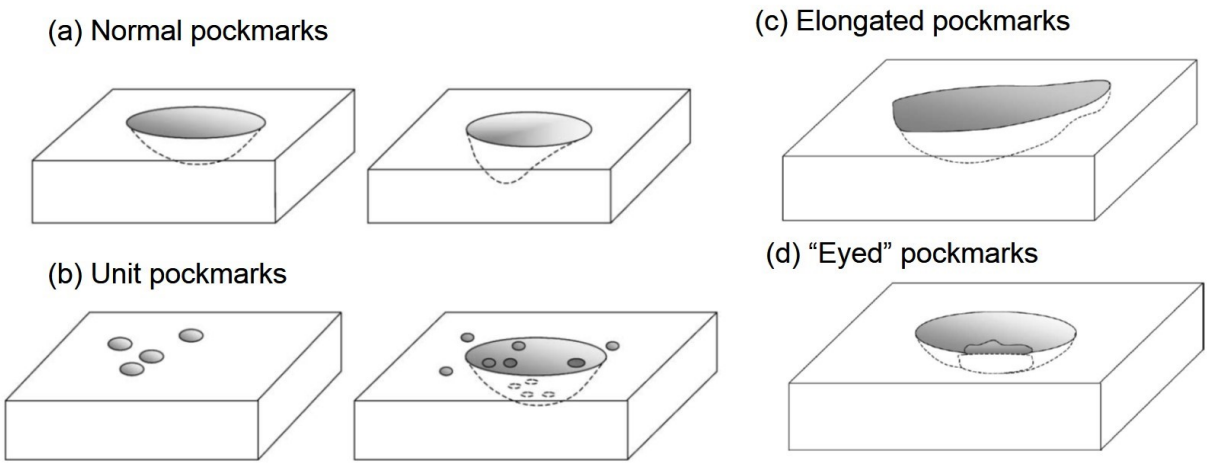


Fig. 1.8. Illustration of the major classes of pockmarks. (a) Normal pockmarks, regular (left) and asymmetric (right); (b) unit pockmarks, without (left) and with ‘parental’ normal pockmark (right); (c) elongated pockmark (can also be a composite pockmark); (d) ‘eyed’ pockmark contains an acoustically high reflective object or region in its central part. (modified from Hovland et al. (2002))

### 1.4.3. Gas hydrate mounds

Gas hydrate mounds are submarine dome structures, also known as gas hydrate pingoes, that have been observed in numerous seep sites from continental margins (Hovland and Svensen 2006; Paull et al. 2008; Serié et al. 2012; Suess et al. 2001) to deep basins (Ryu et al. 2009; Sahling et al. 2016) as well as the Arctic region (Andreassen et al. 2017; Paull et al. 2007). Their sizes vary widely ranging from a few meters to a few hundreds of meters in diameter and centimeters to tens of meters in height (MacDonald et al. 2003).

Hydrate mounds are typically formed by gas hydrate accumulation in the shallow subsurface. Some of the pingo-like features are related to the dissociation of gas hydrate and subsequent extrusion of sediments (Paull et al. 2007). The mechanism for gas hydrate mounds formation can be analogized with pingoes in permafrost regions. The formation of pingoes is attributed to the hydrostatic pressure by the expansion of refreezing water which may cause the frozen ground to rise and the ice core to form. Some pingoes are linked to additional water sources supplied from the subsurface, increasing the volume of ice core and enhancing their size (Paull et al. 2007). The formation of gas hydrate mounds is suggested to be associated with gas hydrate formation rather than ice (Hovland and Svensen 2006). The free gas accumulation beneath the seafloor within the GHSZ may cause the gas hydrate formation which increases the hydrostatic pressure in the subsurface and may result in the surrounding seafloor to dome up (Bohrmann and Torres 2006; Hovland and Svensen 2006; Paull et al. 2008). Different seafloor morphologies and geophysical characteristics can account for different development stages associated with the dynamic formation and dissociation of shallow gas hydrate. Besides the gas hydrate mounds, other seafloor features are suggested to be associated with the formation and dissociation of gas hydrate in the subsurface, for example: giant gas mounds (Kvenvolden 1988; McConnell and Kendall 2002), disruption craters (Andreassen et al. 2017; Prior et al. 1989; Sultan et al. 2014), sediment slides (Brown et al. 2006; Paull et al. 2000; Schmuck and Paull 1993) and collapse features (Berndt et al. 2005; Dillon et al. 1998).

### 1.4.4. Asphalt volcanos

Submarine asphalt volcanos (also known as asphalt mounds) are considered to be a distinct type of geological structure, consisting of asphalt deposits with morphologies similar to volcanic lava flows. Seepage of heavy hydrocarbons which alter by chemical, biological and physical weathering can lead to the formation of asphalt deposits at the seafloor (Schubotz et al. 2011b). Submarine asphalt deposits have been attracted considerable interest since asphalt volcanism was first discovered in 2003 at Chapopote Knoll, southern Gulf of Mexico (Bohrmann and Schenck 2004; MacDonald et al. 2004). Extensive lava-like solidified asphalt emanated from the seafloor along the southern rim of a broad, crater-like depression near the crest of Chapopote Knoll. The extrusion of heavy oil forms characteristic sub-circular to linear flow structures that are 'ropy' or 'rough' similar to magmatic lava flows at the seafloor. Subsequently, asphalt volcanism has been introduced as a unique form of natural hydrocarbon seepage at the seafloor (MacDonald et al. 2004).

Marcon et al. (2018) suggested that the extensive asphalt flow at Chapopote Knoll likely erupts during phases of intensified activity separated by periods of reduced activity. However, the asphalt deposits can also be subject to sequential alterations after extrusion of heavy oil from the seafloor. As a model described by Brüning et al. (2010), the heavy oil is a transition compound between mobile and immobile; the mobile phase material can spread smoothly over the seafloor and due to its density slightly less than ambient seawater, local domes and whips can be formed. As a result of the loss of volatiles, the viscosity of heavy hydrocarbons increases and the volume decreases. Further solidification and subsequent shrinkage lead to the formation of surface fracturing at the asphalt surfaces, followed by fragmentation of the entire deposit (Fig. 1.9). Fragmentation of asphalt fragments proceeds until cobble-to-boulder-sized pieces become buried by sedimentation (Brüning et al. 2010).

Despite the importance of oil seeps as major sources of hydrocarbons to the ocean and atmosphere as well as a large number of oil seeps have been documented globally (Kvenvolden and Cooper 2003; Suess 2018), to date only a small number of seafloor submarine asphalt deposits have previously been observed. After Chapopote asphalt volcanism was introduced, asphalt deposits have been also observed at ten other sites in the southern GoM (Sahling et al. 2016). In the northern GoM, extensive asphalt deposits have also been discovered at Puma (Weiland et al. 2008) and Shenzi (Williamson et al. 2008) in the Green Canyon Blocks, as well as two other sites (NOAA 2017) near the Sigsbee Escarpment. The evidence of submarine asphalt deposits has been reported at a growing number of locations worldwide, including submarine tar mounds (Vernon and Slater 1963) and 7 extinct asphalt volcanoes (Valentine et al. 2010) in the Santa Barbara Basin off the coast of southern California, and more than 2000 asphalt mounds at the Angolan Margin, southern Congo Fan (Jones et al. 2014) as well as the asphalt seeps at the 2700 meters deep North São Paulo Plateau, Southwest Atlantic off Brazil (Fujikura et al. 2017).

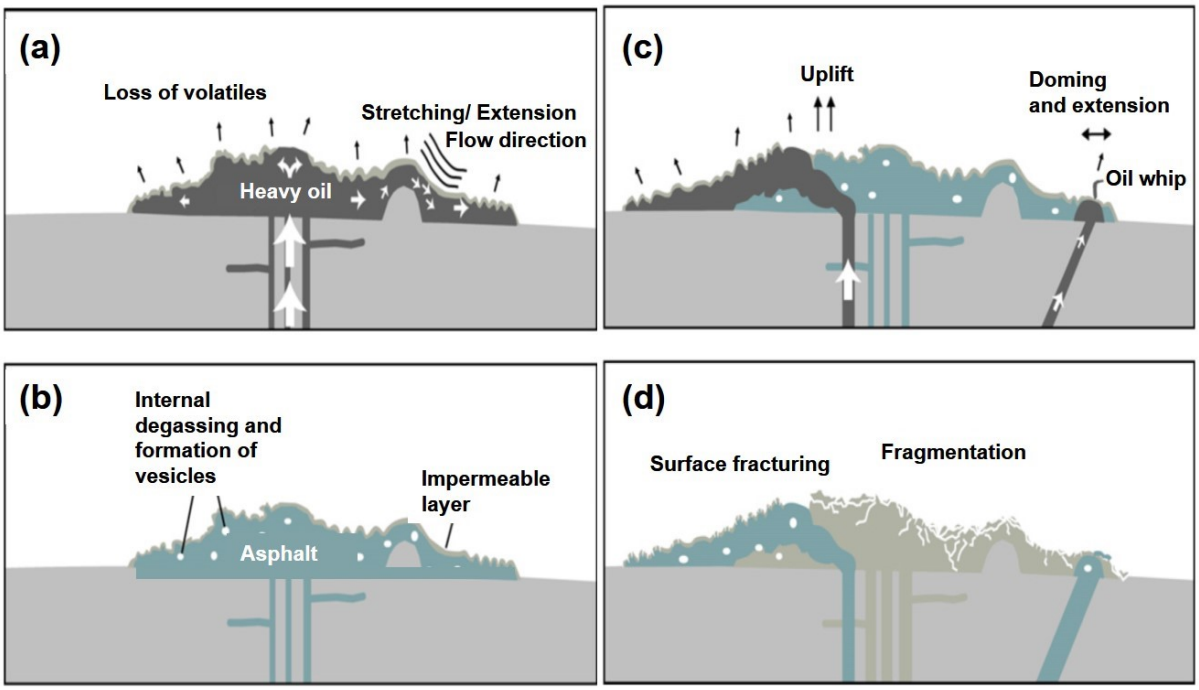


Fig. 1.9. Model of the formation of asphalt deposits at Chapopote Knoll. (a) Extrusion of heavy oil forms characteristic flow structures due to a higher viscosity at the surface of the flow compared to the interior during deposition; the asphalts lose volatiles into the water column. (b) The impermeable layer prevents further loss of volatiles or degassing into the water column. (c) Further heavy oil extrusions cause local up-doming and piercing through the older deposit and form oil whips at the seafloor. (d) The asphalts are further altered due to chemical, biological and physical weathering, which causes shrinkage and surface fracturing; finally, the fragmentation of the asphalt deposit. (modified after Brüning et al. (2010))

Asphalt mounds in the GoM and Angolan Margin are located in areas associated with salt tectonism (Ding et al. 2010; Gay et al. 2004; Weiland et al. 2008; Williamson et al. 2008), whereas those described in the Santa Barbara Basin and at the North São Paulo Plateau are related in the compressional tectonics (Eichhubl et al. 2002; Fujikura et al. 2017). These dynamic geological processes can lead to form effective conduits for asphalt, oil and gas migrating through the sediment to the seafloor and into the water column (Ding et al. 2008; Gay et al. 2004; Keller et al. 2007). Further exploration is needed to investigate such features and to determine the abundance, distribution, function, formation and evolution of asphalt deposits.

## 1.5. Methods to investigate seeps

### 1.5.1. Hydroacoustic investigations

Datasets used for bathymetry and backscatter were acquired by systematic hydroacoustic survey using ship-based multibeam echosounder (MBES) during R/V METEOR cruise M114 in the southern GoM. The hull-mounted deep-sea system Kongsberg EM122 (operating at 12 kHz) was mounted on the R/V METEOR, configured for 1 by 2 degrees, with a swath angle up to 150 degrees and maximum coverage of 6 times the water depth. In addition, Autonomous Underwater Vehicle (AUV) -derived MBES (MARUM AUV SEAL 5000 with Kongsberg EM2040, operating at 300 kHz) was deployed at an altitude of 80 meters above the seafloor at the Mictlan Knoll to investigate the micro-bathymetry and seafloor backscatter. Bathymetric data and seafloor backscatter were post-processed with an open-source package MB-system developed by Caress and Cheyes (2017). Ship-based bathymetry (water depth from ~1000 to ~3700 mbsl) was gridded to 25 meter resolution and AUV-based bathymetry (water depth from ~3100 to ~3300 mbsl) was gridded to 1 meter resolution.

Specific frequency acoustic waves emitted by a transmit transducer array of MBES travel through the water column toward the seafloor and reflect or scatter off a target, and then return to the receive transducer array. After receiving the returning waves by receive transducer array, the computer module of MBES determines length of the sonar-to-seafloor-to-sonar propagation path (i.e., range) and the associated time delay then translates them to bathymetry data. Apart from the bathymetry, the returning acoustic waves reflected energy (amplitude), provide the information of the acoustic reflectivity of the seafloor (e.g. seafloor backscatter) as well as the water column (see chapter 1.5.2) (Mayer 2006; Mitchell et al. 2018). In contrast to the bathymetric measurement, interpreting the physical characteristics of seafloor from backscatter data is more complex and requires more parameters to be known or estimated and depends on many factors: (1) amplitude of the acoustic signal projected into the water; (2) The loss and redistribution of acoustic energy; (3) The sensitivity of the sonar receiver to acoustic signals (4) The contribution of unwanted signal fluctuations and (5) The physical phenomena of interaction of the pulse arriving at the seafloor that generate the echo itself (see e.g. review by Lurton and Lamarche (2015)). In general, a “rough” seafloor morphology scatters more acoustic energy than a “smooth” one (Augustin et al. 1996; Mitchell 1993). Therefore, the seafloor backscatter signature is usually considered as an indicator or proxy for the seafloor substrate, physical composition and fine-scale geometry (Lurton and Lamarche 2015).

Analyzing the seafloor backscatter has also been utilized for hydrocarbon seeps studies (Naudts et al. 2008; Nikolovska et al. 2008; Orange et al. 2002; Römer et al. 2014a; Sahling et al. 2008a). For example, high seafloor backscatter signature was associated with vestimentiferan tubeworms and authigenic carbonates at the pockmark in the northern Congo Fan area (Sahling et al. 2008a). Gay et al. (2007) proposed a model illustrating that the intensity of seafloor backscatter is generally enhanced by the occurrence of hard substrates like authigenic carbonates, tubeworm as well as bivalve shells, but decreases with the presence of hemiplegic sediments (Fig. 1.10).

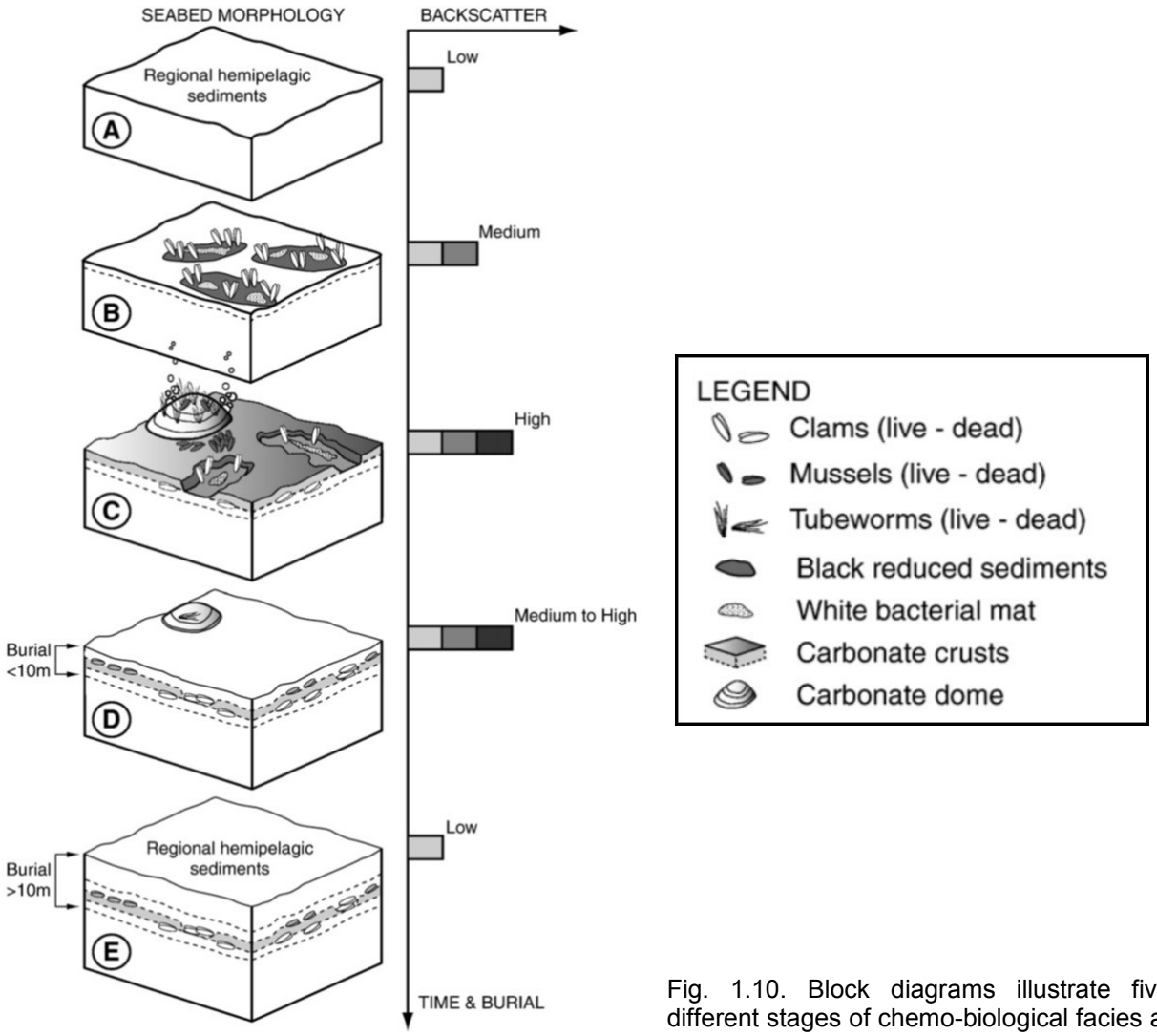


Fig. 1.10. Block diagrams illustrate five different stages of chemo-biological facies at the seabed associated with fluid seep activity (from Gay et al. (2007)).

### 1.5.2. Water column imaging

The water column datasets were collected simultaneously by the ship-based MBES during hydroacoustic surveys for bathymetry and seafloor backscatter during M114 cruise in the southern GoM. In addition, the manuscript III (Chapter 6) present the water column data (80 meters above the seafloor) obtained by the AUV-derived MBES at the Mictlan Knoll. The datasets were imaged and processed with the Fledermaus FMMidwater Interface (Version 7.4.1; Quality Positioning Services B. V., the Netherlands) to inspect hydroacoustic anomalies caused by the presence of gas bubbles in the water column. These hydroacoustic anomalies are also termed as “flares” due to their “flame-like” acoustic appearances on the echograms of the water column (Fig. 1.11) (Greinert et al. 2002; Nikolovska et al. 2008).

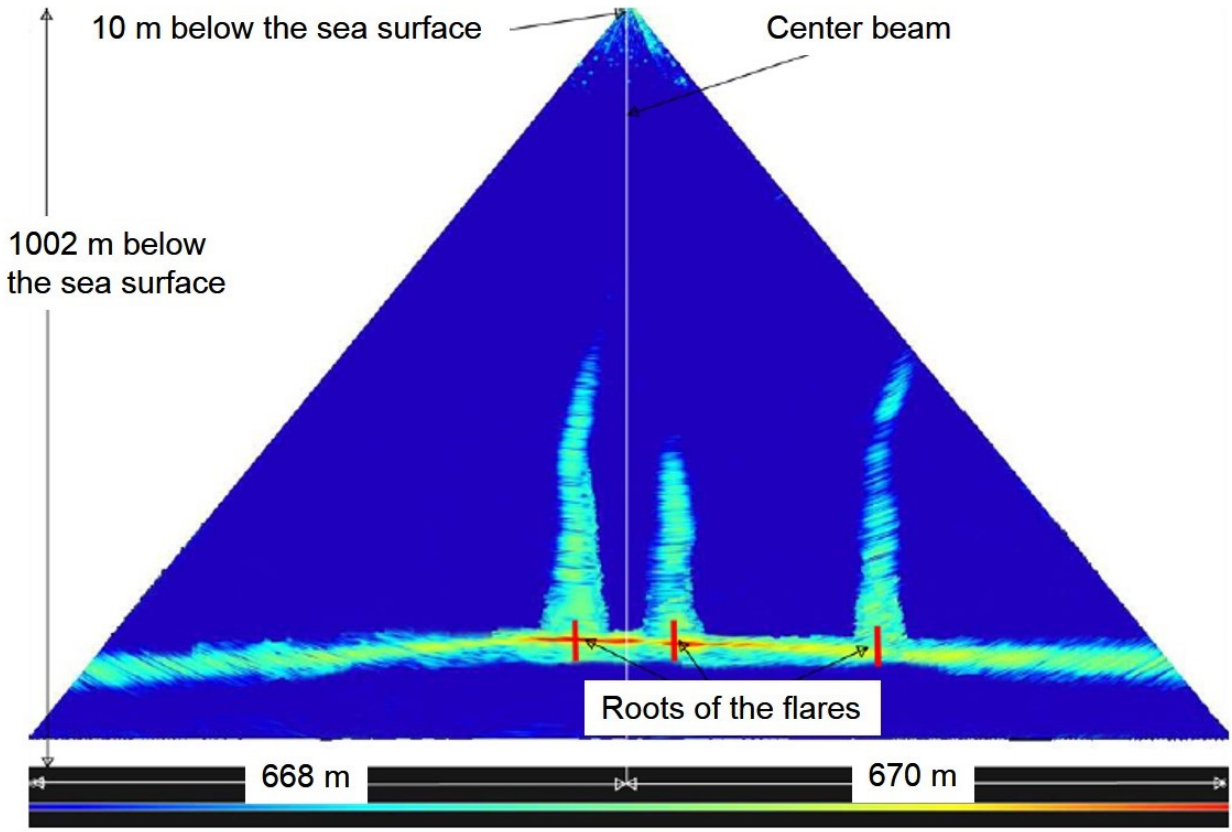


Fig. 1.11. Illustration of the acoustic anomalies on the water column echogram from ship-based MEBS, appearing like flares. (from Nikolovska et al. (2008))

Gas bubbles in the water column resonate at a frequency dependent on their size causing strong acoustic reflectors due to the differences of sound velocity and density between water and free gas phase (Medwin and Clay 1998). Such acoustic character allows the ship-based or vehicle-mounted echosounders to investigate the locations of gas bubble emission remotely. Modern MBES system provides large angular coverage (typically 120 ~150°), which facilitates large-scale exploration of hydrocarbon seeps by research vessels surveying at the sea surface (Colbo et al. 2014). Moreover, the underwater vehicle-mounted echosounder such as AUV-derived MBES could provide higher resolution of water column data near the seafloor, allowing for more accurate positioning of the gas bubbles emission (Mayer 2006; Mitchell et al. 2018). Recently, analyzing the midwater acoustic reflector of MBES has been a common application for investigating hydrocarbon seeps (Schneider von Deimling et al. 2007). For example, numerous gas emissions occurred at the continental margin west of Svalbard (Sahling et al. 2014), and 357 gas emissions sites were found in a region of 6000 $km^2$ of the northern GoM (Weber et al. 2014).

### 1.5.3. Visual seafloor observations

Visual seafloor observation can provide direct evidence for the occurrence of the hydrocarbon seeps and obtain detailed information to characterize the seafloor environment. In this work, visual seafloor observations were carried out by the deep-water remotely operated vehicle (ROV) MARUM Quest 4000m (Fig. 1.12 left) and a TV-sled (Fig. 1.12 right).

ROV Quest 4000m is highly maneuverable and its control system provides certain auto flight function to increase the stability for exploring, sampling and video mosaicking above the seafloor. The underwater positioning of the vehicle was acquired by the shipboard IXSEA Posidonia ultra short base line (USBL) positioning system. During the M114 cruise, high resolution seafloor images (2.2 mega-pixel spatial resolution at 59.94 Hz interlaced) were taken by the ROV mounted video camera INSITE PACIFIC ZEUS 3CCD HDTV (named Zeus). In addition, the photomosaic shown in Manuscript III (Chapter 6) was taken by a downward-looking camera Prosilica GT 6600 full-frame (35mm CCD sensor) photo camera (29-megapixel resolution).

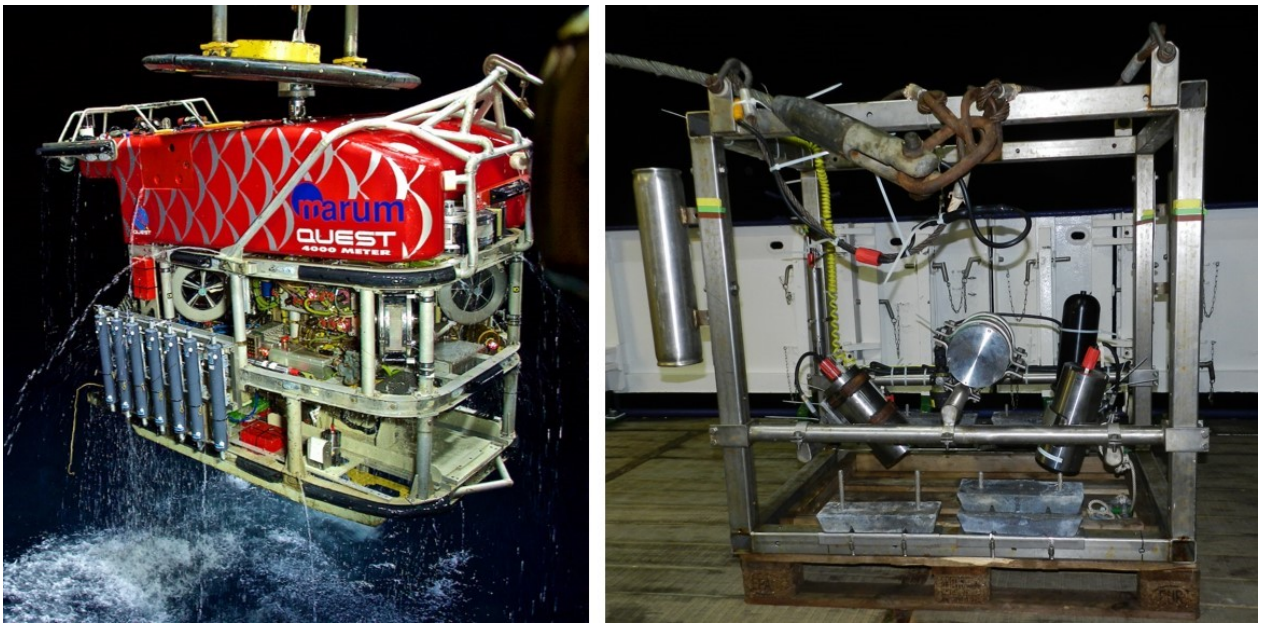


Fig. 1.12. (Left) MARUM Quest 4000m weighs about 45 tons and is equipped with sampling toolskid, niskin bottles and launched as well as recovered through the A-frame by an adapted launch and recovery system (photo courtesy S. v. Neuhoff); (Right) The TV-sled was equipped with a video telemetry and was connected to the vessel by a transmitting cable (photo courtesy H. Sahling).

During the M114 cruise, the TV-sled was used to investigate the evidence or indicators of hydrocarbon seeps prior to the ROV dives as well as inspect suspicious seafloor revealed from the information of bathymetry or seafloor backscatter. The TV-sled frame was equipped with a video telemetry by OKTOPUS, an Aqua Pix video time-lapse camera (VTLC), and lights. The TV-sled was connected to the vessel by a transmitting cable (Fig. 1.12 right) and usually towed along transects with a speed of 0.2 ~ 0.5 knots. During the survey, the online video stream (black and white) was recorded and transmitted simultaneously to the vessel. The higher resolution colored footages of the VTLC were saved in a portable memory. Although the quality of the videos from the TV-sled was not comparable to the videos taken from ROV, it was still

capable to differentiate the seafloor with and without indications of hydrocarbon seeps, such as carbonates, microbial mats, asphalt deposits, or benthic chemosynthetic fauna.

### 1.5.4. Gas bubble analysis

ROV Quest 4000m was deployed for gas bubble sampling as well as video documentation at the emission sites. ROV operated pressure-tight Gas Bubble Samplers (GBS) (Pape et al. 2010) were used to sample the gas bubbles at the emission sites in the southern GoM during M114 cruise. The molecular compositions (ratio of Methane: Ethane: propane: *i*-Butane) of gas bubbles were analyzed from five gas emission sites shown in Manuscript I (Chapter 4). The resulting data were further applied for the calculation of the GHSZ in the study area.

The videos sequences taken by ROV-mounted camera Zeus above a gas emission site at the Mictlan Knoll were analyzed frame by frame using the software ImageJ (Rasband 1997-2016) for determining the sizes of gas bubbles. A funnel of known size (16.2 cm in diameter) attached to a GBS (Fig. 1.13) was used as a reference for scale and focal plane to measure the major ($a$) and minor axes ($b$) of gas bubbles. The volumes of gas bubbles were calculated based on the assumption of a rotational ellipsoid with the equivalent spherical radius ($r_e$) (Leifer and Patro 2002) (Eq. 1-3).

$$r_e = (a^2 b)^{\frac{1}{3}} \qquad \text{(Eq. 1-3)}$$

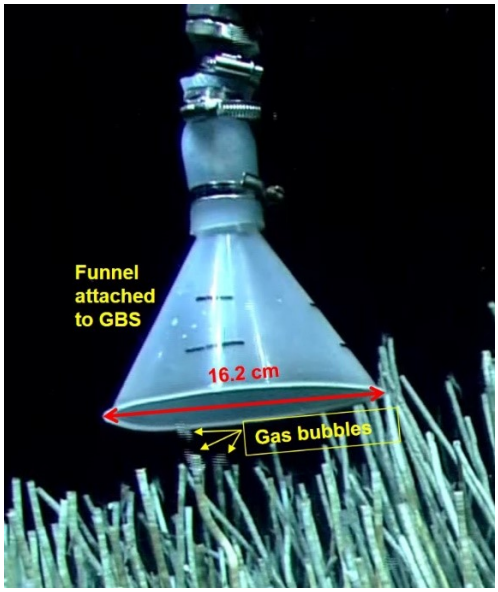


Fig. 1.13. Gas bubble measurement and sampling by using a GBS above a seep site at the Mictlan Knoll. The funnel of the GBS with known dimensions was used as a reference for focal plane and scale.

# 2. Motivation and objectives

The overarching goal of this work is to contribute to the understanding of the hydrocarbon seepage in a complex salt province by investigating the Campeche-Sigsbee salt province in the southern GoM. The previous chapter provides an overview of the current knowledge of various types of hydrocarbon seepage and their seafloor manifestations. However, there is a lack of direct evidence for gas bubble emissions in the southern GoM and the role of hydrocarbon seepage in this region remains unclear. The three manuscripts (Chapter 4, 5, 6) presented in this thesis are aimed to address the aspects outlined in the following.

## 2.1 Gas bubble emissions in the southern GoM

The first overarching objective of this work is to investigate gas bubble emissions in the southern GoM, particularly in the Campeche-Sigsbee salt province. This study area was considered to be an analog to the Mississippi-Texas-Louisiana salt province in the northern GoM, where widespread gas bubble emissions have been observed. Up to date, the occurrence and distribution of hydrocarbon seeps were only indicated by sea surface oil slicks resolved by satellite imagery. However, the origins of oil slicks cannot accurately refer to the seep sites located at the seafloor due to the uncertainties related to the lateral migration of oil in the water column. The following research questions derived:

- Is there any gas bubble emission in the study area?
- How many gas bubble emissions occur in the study area?
- Where are the gas bubble emission sites located?
- How is the spatial distribution of the gas bubble emissions?
- What is the fate of the gas bubble emissions?
- Do the gas bubbles travel from the seafloor up to the atmosphere?
- What are the factors controlling the fate of gas bubble emissions?

These research questions are highlighted in the first manuscript (Chapter 4) by integrating and analyzing the datasets from systemically seafloor and water column flare mapping in the study area. Furthermore, the behavior of gas bubbles in the water column and its fate are addressed by analyzing the composition of gas bubbles and the physical properties of the water column.

## 2.2 Geological structure control on the distribution of hydrocarbon seeps

The second overarching objective is to comprehensively analyze the geological structures controlling the distribution of the hydrocarbon seeps in the study area. The seafloor morphology in the Campeche-Sigsbee salt province is a result of the underlying salt tectonism and the regional deformation events. The different seafloor features indicate that they are related to different geological processes or related to their different stages of development. Furthermore, these geological structures and developments may also be related to hydrocarbon seepage. Therefore, the following research questions are raised:

- How do the salt tectonics and regional deformation affect the seafloor morphologies in the study area?
- Can the geological structures be categorized into different groups according to their seafloor morphologies?
- If the geological structures can be categorized into different groups, do the hydrocarbon seeps at the seafloor follow the different patterns?
- How do the different geological structures influence the fluid migration in the subsurface?

The above listed research questions are addressed in the first manuscript (Chapter 4), and a model was provided to interpret the distribution of hydrocarbon seeps controlled by different geological structures.

## 2.3 Diversified hydrocarbon seepage at the seafloor

The overarching goal is to gain a better understanding of the diverse hydrocarbon seepage system in the study area. Previous studies revealed that there is diverse hydrocarbon seepage, including gas and oil seepage as well as asphalt deposit in the southern GoM. In addition, the submarine asphalt volcanism has been an object of research and has attracted considerable interest since the Chapopote asphalt volcano was discovered in 2003. However, detailed investigations such as high-resolution seafloor mapping, visual seafloor observation, and sampling were only reported at Chapopote Knoll. A better understanding of some relevant research questions was raised:

- Do other submarine asphalt volcanoes beside Chapopote Knoll occur in the study area?
- If other submarine asphalt volcanoes exist, how are seafloor manifestations associated with hydrocarbon seepage?
- What are the similarities and differences compared to the Chapopote asphalt volcanism?

These research questions are addressed in the second and third manuscript. The second manuscript revealed water column flare mapping as well as visual seafloor observations at Challenger Knoll, known from DSDP drilling. The third manuscript reported about high-resolution mapping, visual seafloor observation, and sampling at Mictlan Knoll.

# 3. Study area

The Gulf of Mexico (GoM) is a nearly enclosed ocean basin with an area of about $1.6 \times 10^6$ $km^2$, connected to the Atlantic Ocean via the Florida Straits and connected to the Caribbean via the Yucatán Channel. The GoM is bounded on the north, northeast as well as northwest by the coast of the United States, on the south and southwest by Mexico and on the southeast by Cuba (Fig. 3).

The present GoM is commonly suggested to have originated from the Late Triassic time to early Jurassic as a result of rifting within the North American Plate as it began to break up and drift away from the African and South American plates (Pindell 1994; Salvador 1991a; Sánchez-Rivera et al. 2011; White 1980). The rifting process probably continued until Middle Jurassic times with the formation of "transitional" and "stretched" continental crust across the central part of the GoM. During the late Middle Jurassic to very early Late Jurassic, the basin was intermittently filled by seawater, resulting in the formation of extensive and thick salt deposits across a large area currently known in the GoM (Salvador 1991b).

The Sigsbee Abyssal Plain is located in the central-western GoM, which is the deepest part (~3700 mbsl) of the GoM with a generally flat seafloor morphology. Very thick sedimentary layers (5 km to 10 km) including the Miocene, Pliocene as well as Pleistocene sediments and recent turbidities are underlying the plain (Ewing et al. 1958; Ewing et al. 1969b; Shaub et al. 1984). The Sigsbee Abyssal Plain merges into the Mississippi Deep Fan to the east, terminated by the Sigsbee Escarpment to the north and rise gradually connecting to the continental slope to the west. The flat seafloor of the plain is interrupted by numerous salt diapirs and salt domes in an area about $7.5 \times 10^4$ $km^2$ that are known as the Campeche-Sigsbee salt province in the southern GoM.

The focus of this study is in the Campeche-Sigsbee salt province, which consists of the Campeche Knolls in the south and Sigsbee Knolls in the north, separated from the Mississippi-Texas-Louisiana salt province in the northern GoM by the Sigsbee Abyssal Plain (Fig. 3). The Campeche-Sigsbee salt province with water depths between 1600 and 3750 mbsl comprises a hummocky seafloor morphology, which has been suggested to be controlled by salt tectonism (Sánchez-Rivera et al. 2011; Worzel et al. 1968). The salt tectonism in this salt province is considered to be an analog to the Mississippi-Texas-Louisiana salt province in the northern GoM (Garrison and Martin, 1973). It has been speculated that these two salt provinces are parts of a formerly single salt deposition area that was split and separated in the early Late Jurassic times during the opening of GoM (Salvador 1991a). The tectonic evolution of Campeche-Sigsbee salt province corresponds to the regional deformation events affecting the sequences salt deposition during the Jurassic age (Angeles-Aquino et al. 1994; Cruz-Mercado et al. 2011), which is equivalent to the age of Louann Salt formation on the continental slope of the northern GoM (Garrison and Martin 1973; Salvador 1991a).

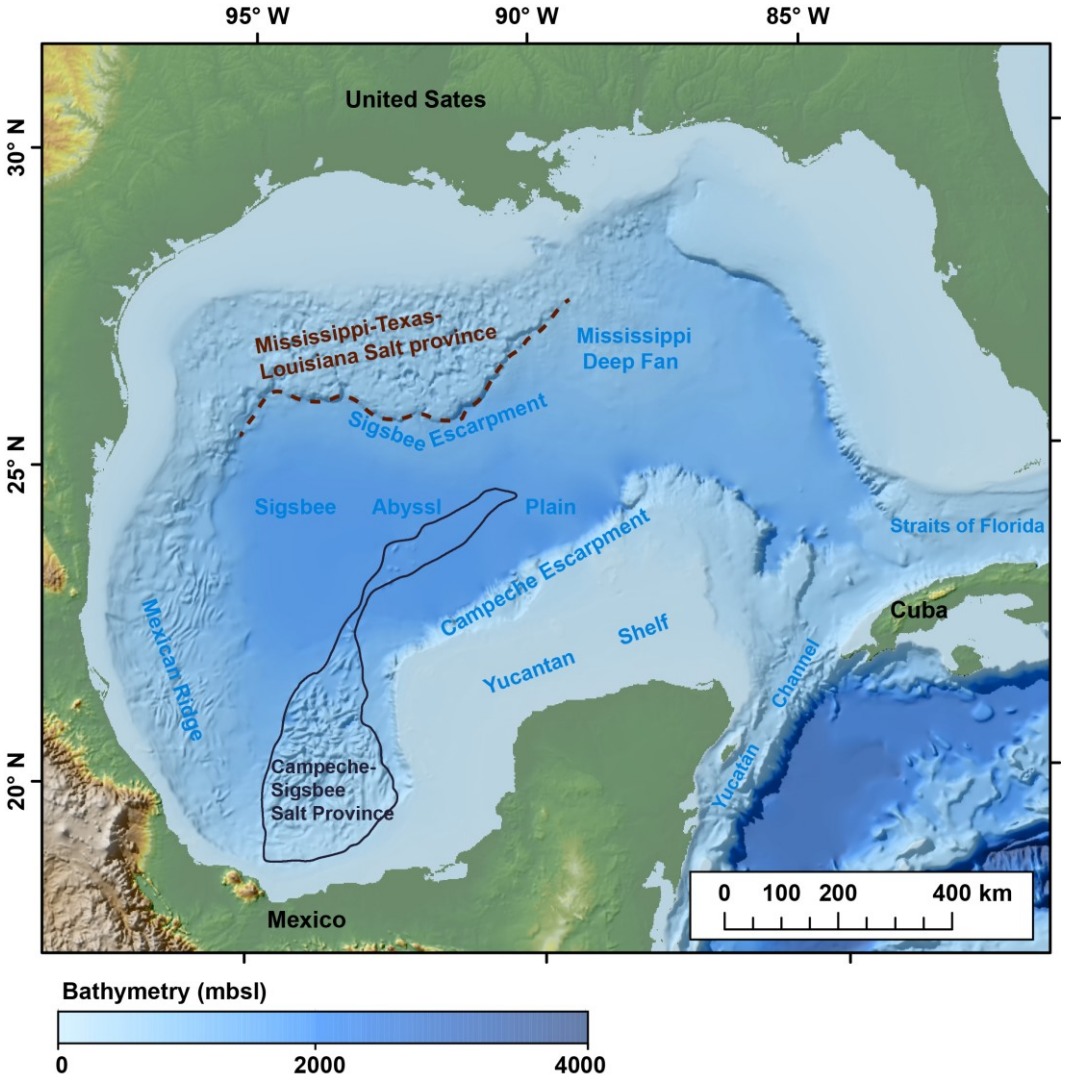


Fig. 3.1 Regional setting of Gulf of Mexico, the Campeche-Sigsbee Salt province is outlined in black.

The Campeche-Sigsbee salt province is characterized by active hydrocarbon seepage, including natural oil slicks on the sea surface (MacDonald et al. 2015; Suresh 2015; Williams et al. 2006), asphalt deposits at the seafloor (Brüning et al. 2010; MacDonald et al. 2004) and gas as well as oil emission from the seafloor (Sahling et al. 2016). The lithological report of the Deep Sea Drilling Project (DSDP) Leg 1 at site 2 revealed that the petroleum accumulations are associated with salt diapirism in the Sigsbee Knolls (Ewing et al. 1969a). In the Campeche Knolls, DSDP Leg 10 site 88 drilled into the top of the salt dome, which terminated before reaching the cap rock due to abundant natural gas encountered at 135 meters (Worzel et al. 1970). The major source of the hydrocarbon in this province is related to the source rock deposition during the Late Jurassic time (Magoon et al. 2001).

# 4. Manuscript I: Widespread gas emissions in the southern GoM

## Widespread distribution of gas emissions at the Campeche and Sigsbee Knolls, Southern Gulf of Mexico

Chieh-Wei Hsu*[,1], Miriam Römer[1], Ian MacDonald[2], Markus Loher[1], Thomas Pape[1], Paul Wintersteller[1], Gerhard Bohrmann[1]

**In preparation for submission to Marine and Petroleum Geology**

[1]MARUM – Center for Marine Environmental Sciences and Department of Geosciences at the University of Bremen, Klagenfurter Str. 4, 28359 Bremen, Germany

[2]Department of Earth, Ocean and Atmospheric Science, Florida State University, Tallahassee, Florida 32306-4320, USA

[†]Deceased April 23, 2018

*Corresponding author: Chieh-Wei Hsu
phone: +49 (0) 421/218 65055, e-mail: cwhsu@marum.de

Key words: hydrocarbon seepage, gas bubbles, oil leakage, salt province, Southern Gulf of Mexico

## 4.1 Abstract

Hydrocarbon leakage linked to sub-bottom reservoirs is known to occur at the Campeche and Sigsbee Knolls, Gulf of Mexico. The hydrocarbon deposits in the southern Gulf of Mexico are related to salt domes, providing various traps for petroleum. To gain a better understanding of the activity of hydrocarbon seepage in these salt provinces, it is important to consider various types of hydrocarbon seepage, including oil slicks, asphalt flows as well as gas emissions. Very little studies are known about seepage and gas emissions in this area. Our investigations present the first comprehensive analysis of the occurrence and distribution of widespread gas emissions in the Campeche and Sigsbee Knolls. In order to understand the presence of gas release from the seafloor and its relationship to geological structures, an extensive multibeam survey was conducted during R/V METEOR expedition M114. 209 gas emission sites were found to be widely distributed at the seafloor in areas of water depths between 1,000 and 3,750 meters below sea level. These also include the highest flare ever reported in the marine environment, the flare rising about 3,100 m from the Challenger Knoll. We characterized the morphological structures of over 40 individual knolls and ridges in detail and classified the seafloor elevations into four principal structure types. We introduce a gas migration model to interpret the distribution pattern of gas emissions at the seafloor of each structure type. We found that the geological structures control the distribution of hydrocarbon seepages in the salt provinces of the southern Gulf of Mexico. Furthermore, none of the gas emissions reached the sea surface, which indicated that a direct contribution of methane from rising gas bubbles to the atmosphere is insignificant in the area.

## 4.2 Introduction

Gases such as methane, released from the seafloor into the water column, have been documented globally from continental shelves to abyssal depths (Aharon 1994). Locations of methane seepage at the seafloor are expressions of sub-seafloor fluid and gas circulation systems which are often characterized by focused emission of gas from the seabed into the ocean known as cold seeps (Suess 2014). Since methane is representing a potent greenhouse gas, several research efforts have been made to understand its sources and sinks (IPCC 2013). Methane emission sites have been discovered in the ocean in many different geological settings at both passive and active continental margins. While in active subduction zones due to the convergence and resulting tectonic stresses the fluid and gas circulation of the continental margin deposits has tectonic causes (Ranero et al. 2008), the cases at passive margins are more diverse. At passive margins, where tectonic stress is comparatively lower than at active margins, seepage systems are largely operated by hydrological pumps that circulate large amounts of fluids. Rapid burial and associated heating of sediments at continental margins increase the probability of oil and gas generation. As a result, mobile organic compounds like methane are expelled upward by buoyancy and compaction, followed by migration in the uppermost sediments (Matthews 1996; Suess 2014). Gases may be trapped as gas hydrates in the hydrate stability field (Bohrmann and Torres 2006), may react with other substances like sulfate to produce hydrogen sulfide, or might be released as free gas from the seabed. Such scenarios of methane pathways are documented at many locations, like in the Black Sea (e.g. Pape et al. 2011; Römer et al. 2012a), in the North Atlantic (e.g. Bünz et al. 2012; Mau et al. 2017; Skarke et al. 2014), in South Atlantic (e.g. Miller et al. 2015;

Sahling et al. 2008a), in the Pacific (e.g. Suess et al. 2001), and Indian Ocean (e.g. Mazumdar et al. 2009; Römer et al. 2012b). In the northern Gulf of Mexico as well as in the Campeche and Sigsbee Knolls, petroleum formation associated with salt diapirism has been reported previous studies (Cruz-Mercado et al. 2011; Ding et al. 2010; Ewing et al. 1969a; MacDonald et al. 2003).

Continuous improvements of seafloor multi-beam and single-beam mapping have shown that hydrocarbon seepage is documented by distinct seafloor morphologies as well as backscatter strength representing typical geological sub-seabed structures (Bünz et al. 2012; Römer et al. 2012a). For instance, using high-resolution multi-beam surveys from the Campeche Knolls, Ding et al. (2010) identified several particular seafloor features and hypothesized their evolution related to hydrocarbon seepage.

Hydrocarbon seepage and gas hydrates were found at the Chapopote Knoll in the Campeche Knolls associated with massive asphalt deposits (Brüning et al. 2010; MacDonald et al. 2004). Recent visual seafloor investigations by remoted operated vehicle (ROV) at Chapopote Knoll using a powerful optical mosaicking technique documented several asphalt flow units representing distinct eruption phases of intensified asphalt flows (Marcon et al. 2018). The asphalt potentially erupts as a liquid of very heavy oil, which was altered at the seafloor by chemical, biological, and physical weathering (Schubotz et al. 2011a). Chemosynthetic communities, specifically tubeworms and mussels, are associated with asphalt deposits (MacDonald et al. 2004). Microbiological investigations on symbionts of chemosynthetic animals from Chapopote expanded the limited range of substrates known to power chemosynthetic symbioses (Rubin-Blum et al. 2017). A recent expansion of marine-geoscientific exploration work in the Campeche Knolls documented that Chapopote is not the only knoll, characterized by asphalt deposits and many knolls are associated with the asphalt seepage (Sahling et al. 2016).

In addition, the widespread occurrence of oil slicks at the sea surface illustrated by satellite imagery already suggested that the Campeche Knolls comprises extensive natural hydrocarbon seepage (Suresh 2015; Williams et al. 2006). Based on repeated Synthetic Aperture Radar (SAR) observations, oil slick origins (OSO) at sea surface can be localized by comparing the mean centers of several slicks. Concerning the interpretation limits of the remotely sensed data, Williams et al. (2006) interpreted three categories: definite seeps, probable seeps and possible seeps. Figures 4.1 and 4.2 show the postulated seep locations that were classified as definite and probable. Possible seeps were excluded in this study as the corresponding oil slicks are probably not caused by natural oil seepage, but, e.g. algae bloom, local wind field, or anthropogenic activity (Brekke and Solberg 2005). Ding et al. (2010) investigated over 20 knolls and ridges using seismic and bathymetric data and distinguished three types of shallow subsurface structures: Chapopote-type, Passive type, and Asymmetric Flap type. The analysis of their geometries revealed that hydrocarbons were accumulated at the center of the Chapopote-type and the subsided flaps of the Asymmetric Flap type. Based on the data set of oil slicks in Campeche Knolls, Ding et al. (2010) suggested that the locations of hydrocarbon seepages were strongly controlled by the shallow sediment structures and salt

tectonics. However, these previous studies focused on the occurrence of oil slicks, but the distribution and controlling factors of gas bubble emissions have not been investigated.

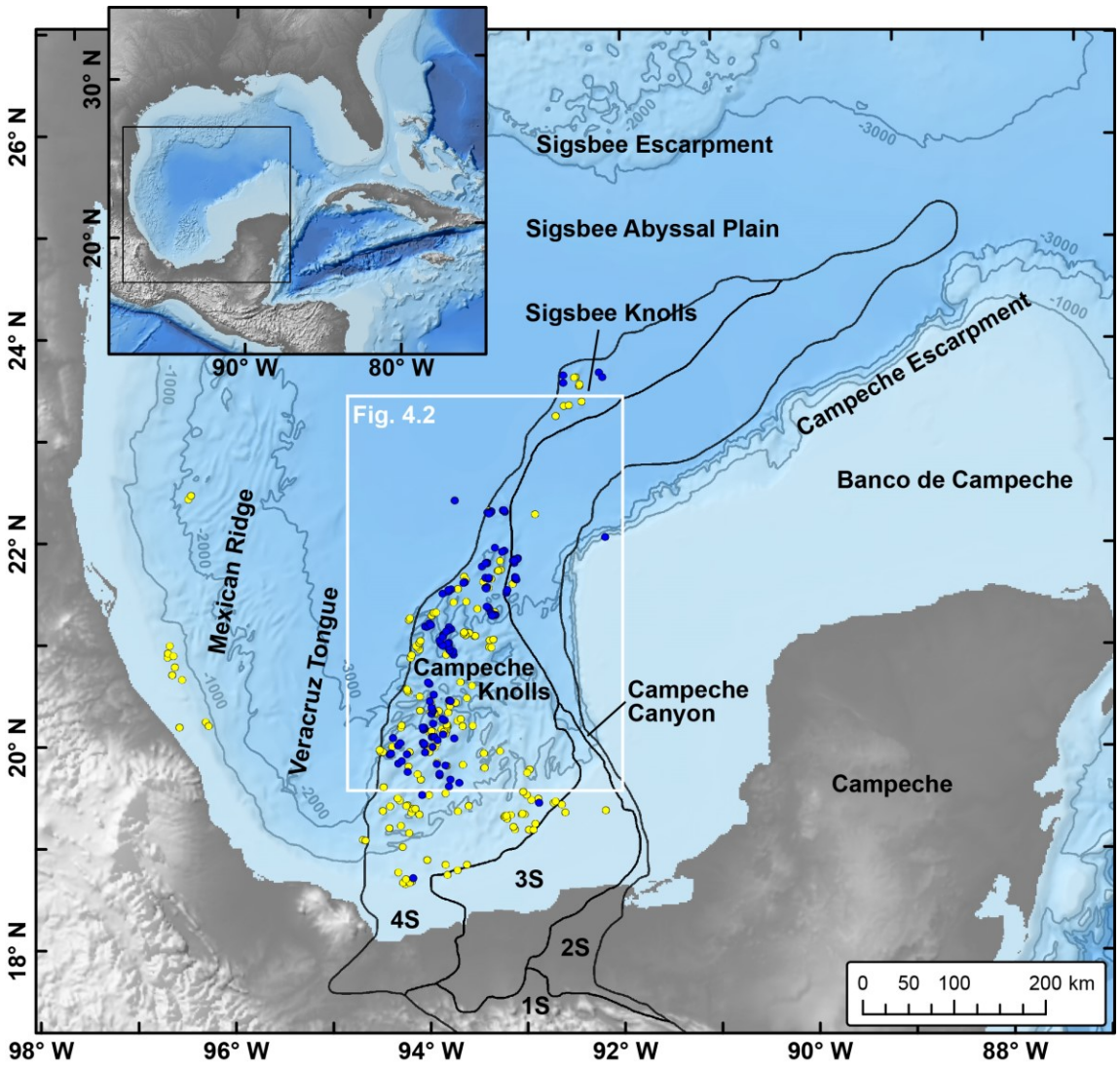


Fig. 4.1. Map of the study area with inset of the southern Gulf of Mexico, including region of the Campeche and Sigsbee Knolls areas in the central part of southern Gulf of Mexico. Note that the knolls are located within the sub-province 4S of the South Gulf Salt Province (outlined in black after Cruz-Mercado et al. (2011) White box indicates extent of Fig. 4.2. Location of origins of oil slick at the sea surface as identified on satellite (SAR) images by Williams et al. (2006) are shown as blue dots (definite slicks) and yellow dots (probable slicks), for explanations see text. Seafloor bathymetry is based on the GEBCO (General Bathymetric Chart of the Oceans) bathymetry data set.

Methane emitted from the seafloor in the water column could be transferred to the sea surface or atmosphere either directly through bubble transport or indirectly from dissolved methane (Mau et al. 2007; Schmale et al. 2005). Furthermore, the formation of hydrate-skin around bubbles within the Gas hydrate stability zone (GHSZ) is supposed to enhance their lifetime before finally being dissolved in the water column (Greinert et al. 2006; Sauter et al. 2006). The fate of methane bubbles can be investigated using hydroacoustic data from echosounders were shown at the Hakon Mosby mud volcano (Sauter et al. 2006) in areas of the Black Sea (Körber et al. 2014; Sahling et al. 2009). Using this method studies revealed that gas bubbles rise over 2,000 m above the seafloor close to or slightly above the upper limit of the GHSZ in Makran, offshore Pakistan (Römer et al. 2012b). Oil droplets or oil-coated bubbles can be transported large distances (> 100 meters) from seafloor to the sea surface due to the oil surfactant inhibiting bubble dissolution and therefore enhancing methane transport (Leifer and MacDonald 2003; Solomon et al. 2009). Previous studies have reported that significant methane transfer from bubbles without oil surfactant to the atmosphere is more probable from very shallow water depths of less than 100 m (McGinnis et al. 2006; Schmale et al. 2005).

This study concentrates on the occurrence of methane gas emissions and their source in relation to the geology structures at the seabed of the Campeche and Sigsbee Knolls in order to better understand how the geological and morphological settings can be related to the presence of methane gas emissions in these salt provinces. Evidence from these deepwater gas emissions was also studied to determine the expression of gas emissions and the fate of methane through the water column.

## 4.2 Geological setting

Campeche and Sigsbee Knolls are located at salt provinces with active salt diapirism in the southern GoM in water depths between 1600 m to 3750 m (Fig. 4.1). Drill sites 2 and 88 of the Deep Sea Drilling Project (DSDP) (Ewing et al. 1969a; Worzel et al. 1970) confirmed that these diapiric structures in the Sigsbee Knolls and Campeche Knolls represent salt domes associated with petroleum. These areas are separated from the Mississippi-Texas-Louisiana salt province by the Sigsbee Abyssal Plain. Salt tectonism in the southern GoM was considered to be an analog to the Texas–Louisiana slope in the northern GoM (Garrison and Martin 1973). Most of the salt in the Campeche and Sigsbee Knolls is inferred to have deposited in the Late Jurassic during the rifting stage of the Gulf, equivalent to the Middle Jurassic Louann salt at the Texas-Louisiana slope (Angeles-Aquino et al. 1994; Salvador 1991a). The Campeche Knolls is bounded to the west by flat abyssal seafloor of the salt-free Veracruz tongue (Bryant et al. 1991) and to the east by the Campeche Canyon. The canyon itself separates the Campeche Knolls from the huge area of the shallow-water carbonate platform, Banco de Campeche, surrounding the Campeche Peninsula. The Sigsbee Knolls is located in the abyssal plain represented by the deep basin of the southern GoM. To the south, the Sigsbee Abyssal Plain is bounded by the carbonate platform of the Banco de Campeche (Fig. 4.1). The Sigsbee Knolls are separated from the Campeche Knolls by a relatively flat seafloor in ~3700 m water depth.

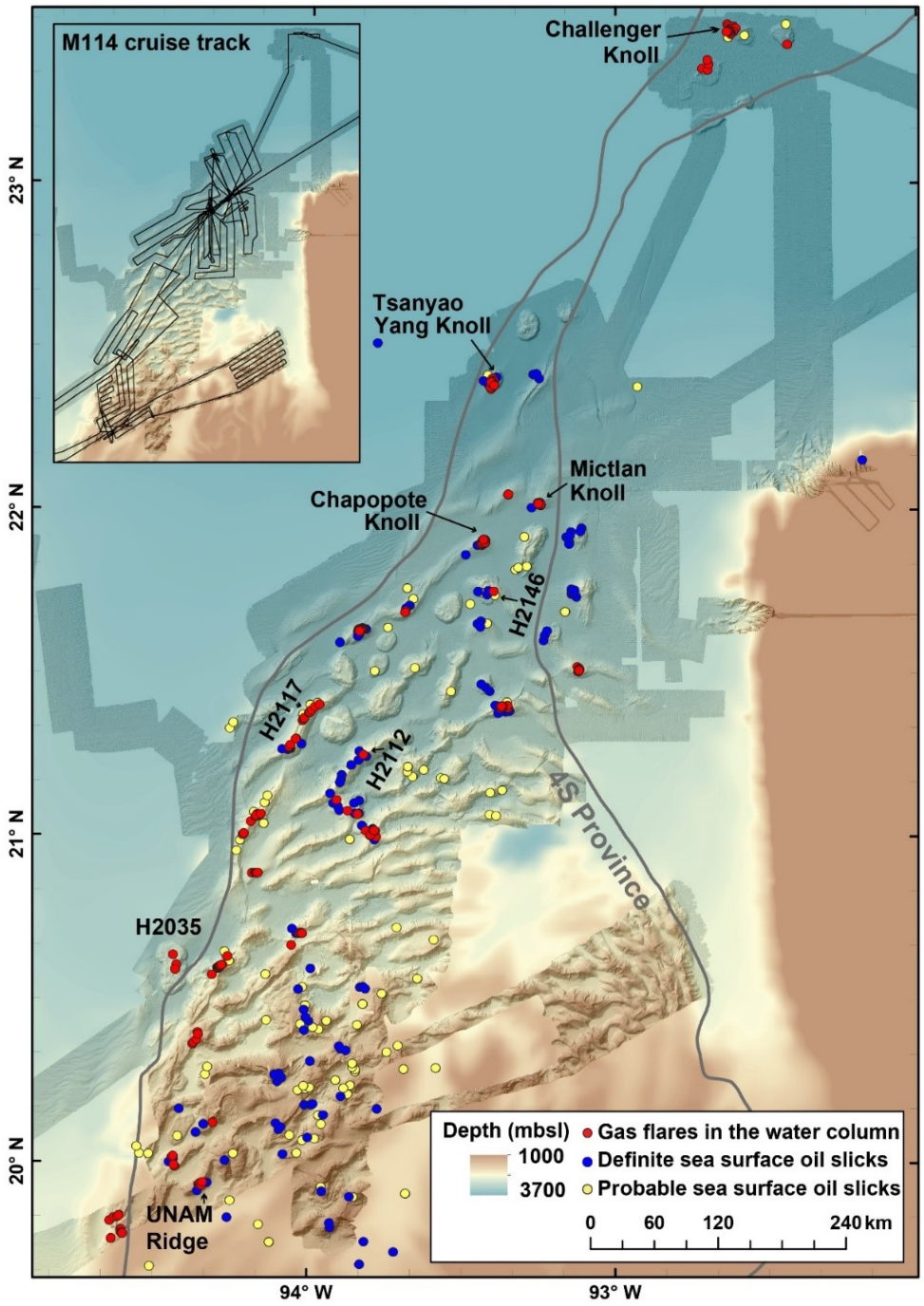


Fig. 4.2. Seafloor maps of Campeche and Sigsbee Knolls areas following the extent indicated in Fig. 4.1 and track of R/V METEOR cruise M114 shown as black lines in inset figure. A compilation of seafloor bathymetry datasets, acquired by ship-based swath echo-sounders during previous cruises SO174, M67/2 and newly in this study during M114, were used and draped on a base-map derived from GEBCO data. Red dots indicate positions of gas flares identified in the water column during hydroacoustic surveys during R/V METEOR cruise M114. Location of origins of oil slick at the sea surface as identified on satellite (SAR) images by Williams et al. (2006) are shown, see also Fig. 4.1.

Salt sub-provinces (Fig. 4.1) of the southern GoM were distinguished based on the original salt deposit thicknesses, shapes and geometries present in each province (Cruz-Mercado et al. 2011; Sánchez-Rivera et al. 2011). The 4S sub-province contains the largest allochthonous and autochthonous salt deposits (Sánchez-Rivera et al. 2011) and the actual density of the salt bodies increases from the southeastern to the northwestern region of Campeche Knolls (Cruz-Mercado et al. 2011). Sea surface oil slicks were found to be concentrated in the northwestern region of 4S sub-province, including Campeche Knolls and Sigsbee Knolls (MacDonald et al. 2015; Suresh 2015; Williams et al. 2006). In the southern deep GoM basin, the Jurassic salt units are overlain by approximately 5–10 km thick sediments (Ewing et al. 1958; Ladd et al. 1976; Shaub et al. 1984). The thickness of sediment varies with water depth and the distance from the southern coast. This sequence of sediment deposits contains prolific petroleum source rocks with the most productive being of the latest Jurassic and Cretaceous age (Magoon et al. 2001).

Campeche and Sigsbee Knolls present an area with complex seafloor morphology comprising numerous bathymetric highs. Some of the structures are named, for example, Challenger Knoll (Ewing et al. 1969a), Tsanyao Yang Knoll (Sahling et al. 2016), Mictlan Knoll (Sahling et al. 2016), and Chapopote Knoll (MacDonald et al. 2004). In order to (geo-)reference all seafloor features unambiguously, they were assigned by the first four digits of the latitude of the bathymetric high, or the latitude of the middle point of the elongated ridge (Table 4.1), which is a system first used by Bohrmann and Schenck (2004).

## 4.3 Materials and Methods

### 4.3.1 Hydroacoustic data collection and detection of gas and oil emissions

Datasets used for bathymetric maps were acquired by ship-based multibeam echosounder (MBES) systems during three cruises to the southern Gulf of Mexico (R/V SONNE cruise SO174 in 2003 (Bohrmann and Schenck 2004), and R/V METEOR cruises M67/2 in 2006 (Bohrmann et al. 2008) and M114 in February–March 2015 (Sahling et al. 2017). Swath bathymetry data were collected using an MBES Kongsberg EM 120 with a frequency of 12 kHz during cruises SO174 and M67/2 and using an MBES Kongsberg EM 122 with a frequency of 12 kHz during cruise M114. All ship-based bathymetric data were processed with MB-system (Caress and Cheyes 2017) and combined into a single map covering the total extent of the Campeche and Sigsbee Knolls. Water column data were recorded using the ship-based MBES Kongsberg EM 122 during cruise M114. Water column imaging for the detection of high backscatter signatures, indicative of gas bubble plumes, were conducted with QPS Fledermaus Midwater (Quality Positioning Services B. V., The Netherlands).

Backscatter signatures caused by gas bubble plumes are commonly referred to as “flares” due to their characteristic appearances in echosounder records (McGinnis et al. 2006; Schneider von Deimling et al. 2007; Wang et al. 2016). All flares identified in this study were traced in the central part of the EM 122 swath (up to 36° on each side of the nadir) as the noise outside of this coverage (i.e., >36° on each side of the nadir) is exceedingly high and makes a reliable identification impossible. Flare signatures were traced manually using the picking tool in Fledermaus Midwater and point clouds were extracted and analyzed in pseudo-3D in Fledermaus. Where flares could not be traced down to the seafloor, the locations of gas

emission sites were determined by projecting the lowermost anomaly of each flare vertically down onto the seafloor.

The spatial relation between flares and sea surface oil slicks was investigated for those parts of our study area (Fig. 4.2), where information on oil slick origins was available from SAR images previously reported by Williams et al. (2006).

### 4.3.2 Gas bubble emission analysis

During cruise M114 the remotely operated vehicle (ROV) MARUM QUEST 4000 m was used for detailed seafloor inspections, size measurements on gas bubbles and gas sampling. Underwater positioning was achieved by using the IXSEA POSIDONIA on both the ROV and the vessel. A broadcast-quality 3CCD HDTV 14 x zoom video camera (Zeus) with 2.2 mega-pixel spatial resolution and a 59.94 Hz interlaced was used for recording video sequences.

Video sequences recorded during ROV dives were analyzed frame by frame and gas bubble sizes were measured against a physical scale (i.e., an object of known size on the same frame) in the software ImageJ (Rasband 1997-2016). Only bubbles rising in the same focal plane as the scale could be analyzed. The major ($a$) and minor bubble axes ($b$) were measured and the volume was calculated by assuming a rotational ellipsoid with the equivalent spherical radius ($r_e$) (equation (4.1)).

$$r_e = (a^2 b)^{\frac{1}{3}} \qquad \text{(Eq. 4.1)}$$

### 4.3.3 Gas sampling and gas hydrate stability calculations

Gas bubbles were sampled by ROV operations using pressure-tight Gas Bubble Samplers (Pape et al. 2010; Sahling et al. 2016) directly above five gas emission sites: UNAM Ridge (GeoB19318-9), Chapopote Knoll (GeoB19328-13), Mictlan Knoll (GeoB19336-8) and Tsanyao Yang Knoll (GeoB19337-12, 19348-7). Phase boundaries for structure I (sI) and structure II (sII) gas hydrates in the Campeche Knolls region were calculated using the program HWHY (Masoudi et al. 2005). The molecular gas compositions used for the calculation were obtained from the five gas samples (Table 4.2). Three CTD stations provided the input for the water column temperatures and the salinity used in the calculations.

Table. 4.1. Summary of the morphological classification of the seafloor structural types identified and defined in this study with indication on the presence of hydrocarbon seepage activities in the southern Gulf of Mexico.

| Bathymertirc highs | Structure type | Location | | Approx. Water | Elevation | Structure size* (km) | | Flares detected | Sea surface oil slicks |
|---|---|---|---|---|---|---|---|---|---|
| | | Latitude | Longitude | (mbsl) | (m) | diameter/ lengtl | width | during M114 | detected |
| Challenger Knoll | Flat-topped-type knoll | 23° 28.02' N | 92° 36.43' W | 3689 | 210 | 9 | N/A | yes | yes |
| H2327 | Flat-topped-type knoll | 23° 25.63' N | 92° 25.70' W | 3652 | 250 | 8.5 | N/A | yes | yes |
| H2320 | Flat-topped-type knoll | 23° 35.68' N | 92° 41.59' W | 3674 | 170 | 11 | N/A | yes | yes |
| H2235 | Chapopote-type knoll | 22° 35.68' N | 93° 09.10' W | 3374 | 350 | 5 | N/A | no | no |
| H2233 | Flat-topped-type knoll | 22° 33.52' N | 93° 17.65' W | 3328 | 480 | 10 | N/A | no | no |
| Isanyao Yang Knoll | Flat-topped-type knoll | 22° 23.19' N | 93° 24.45' W | 3427 | 420 | 7 | N/A | yes | yes |
| H2222 | Furrow-type ridge | 22° 22.01' N | 93° 16.41' W | 3374 | 330 | 31 | 5 | no | yes |
| H2203 | Furrow-type ridge | 22° 03.03' N | 93° 21.06' W | 3072 | 380 | 15 | 4 | yes | yes |
| Mictlan Knoll | Chapopote-type knoll | 22° 01.38' N | 93° 14.90' W | 3180 | 300 | 7 | N/A | yes | yes |
| H2156 | Chapopote-type knoll | 21° 56.24' N | 93° 06.93' W | 2896 | 500 | 7 | N/A | no | yes |
| Chapopote Knoll | Chapopote-type knoll | 21° 54.05' N | 93° 26.14' W | 2956 | 480 | 6 | N/A | yes | yes |
| H2154 | Furrow-type ridge | 21° 49.78' N | 93° 17.46' W | 3095 | 680 | 19 | 7.5 | no | yes |
| H2147 | Furrow-type ridge | 21° 45.37' N | 93° 08.00' W | 2937 | 670 | 16 | 8 | no | yes |
| H2146 | Assymetric-type ridge | 21° 45.21' N | 93° 23.91' W | 2779 | 650 | 20 | 10 | yes | yes |
| H2141 | Furrow-type ridge | 21° 41.32' N | 93° 41.29' W | 2831 | 380 | 17 | 5 | yes | yes |
| H2140 | Flat-topped-type knoll | 21° 41.83' N | 93° 32.72' W | 2900 | 500 | 11 | N/A | no | yes |
| H2139 | Chapopote-type knoll | 21° 39.73' N | 93° 26.40' W | 2973 | 400 | 6 | N/A | no | yes |
| H2137 | Chapopote-type knoll | 21° 37.16' N | 93° 13.82' W | 2916 | 480 | 6 | N/A | no | yes |
| H2136 | Furrow-type ridge | 21° 38.15' N | 93° 49.92' W | 2810 | 520 | 12 | 5.5 | yes | yes |
| H2135 | Flat-topped-type knoll | 21° 38.47' N | 93° 44.72' W | 3249 | 290 | 7.5 | N/A | no | yes |
| H2131 | Assymetric-type ridge | 21° 30.85' N | 93° 07.12' W | 2525 | 600 | 10 | 6 | yes | no |
| H2130 | Flat-topped-type knoll | 21° 30.49' N | 93° 47.26' W | 2887 | 440 | 9 | N/A | no | yes |
| H2128 | Chapopote-type knoll | 21° 28.15' N | 93° 26.28' W | 2788 | 400 | 7 | N/A | no | yes |
| H2124 | Furrow-type ridge | 21° 23.91' N | 93° 22.24' W | 2507 | 780 | 14 | 6 | yes | yes |
| H2119 | Flat-topped-type knoll | 21° 20.54' N | 93° 53.93' W | 2758 | 650 | 13 | N/A | no | no |
| H2117 | Furrow-type ridge | 21° 23.20' N | 93° 59.61' W | 2581 | 680 | 30 | 7 | yes | yes |
| H2112 | Assymetric-type ridge | 21° 15.11' N | 93° 49.43' W | 2320 | 1000 | 48 | 10 | yes | yes |
| H2105 | Furrow-type ridge | 21° 04.81' N | 93° 52.50' W | 2320 | N/A | N/A | N/A | yes | yes |
| H2103 | Furrow-type ridge | 21° 03.97' N | 94° 10.25' W | 2074 | 640 | 48 | 7 | yes | yes |
| H2100 | Furrow-type ridge | 21° 00.33' N | 93° 47.96' W | 2148 | N/A | N/A | N/A | yes | yes |
| H2053 | Assymetric-type ridge | 20° 53.30' N | 94° 10.38' W | 2425 | 320 | 11 | 5 | yes | no |
| H2042 | Assymetric-type ridge | 20° 42.40' N | 94° 01.63' W | 2246 | 850 | 20 | 7 | yes | yes |
| H2036 | Furrow-type ridge | 20° 37.98' N | 94° 15.82' W | 2247 | 1170 | 44 | 7.5 | yes | yes |
| H2035 | Flat-topped-type knoll | 20° 35.50' N | 94° 26.05' W | 2696 | 400 | 17.5 | N/A | yes | no |
| H2022 | Furrow-type ridge | 20° 22.61' N | 94° 21.70' W | 1558 | N/A | N/A | N/A | yes | no |
| H2007 | Flat-topped-type knoll | 20° 07.44' N | 94° 18.42' W | 1375 | N/A | 12 | N/A | yes | no |
| H2006 | Flat-topped-type knoll | 20° 07.44' N | 94° 18.42' W | 1376 | N/A | 11 | N/A | no | yes |
| H2005 | Furrow-type ridge | 20° 10.78' N | 94° 00.62' W | 1616 | N/A | N/A | N/A | no | yes |
| H2004 | Furrow-type ridge | 20° 04.72' N | 94° 00.07' W | 1700 | N/A | N/A | N/A | no | yes |
| H2002 | Flat-topped-type knoll | 20° 00.50' N | 94° 16.09' W | 1170 | 730 | 13 | N/A | no | yes |
| H2000 | Assymetric-type ridge | 19° 59.33' N | 94° 25.80' W | 1668 | 620 | 20 | 5 | yes | yes |
| UNAM Ridge | Assymetric-type ridge | 19° 56.03' N | 94° 21.09' W | 1258 | 800 | 13 | 5.5 | yes | yes |
| H1946 | Furrow-type ridge | 19° 47.03' N | 94° 35.97' W | 1655 | N/A | N/A | N/A | yes | no |

* N/A = not applicable; diameter is applied for the knolls, length and width are applied for ridges

### 4.3.4 Modeling the fate of oil and gas bubbles

A single bubble dissolution module of the Texas A&M Oil spill Calculator (TAMOC) was applied to model the fate of oil and gas bubbles released at the seafloor. This module was developed by Dissanayake et al. (2018) and included gas hydrate formation and detailed equations for the state of hydrocarbons (Gros et al. 2016). This model has been previously applied to hindcast the fate of oil and gas released from the Deepwater Horizon accident (Gros et al. 2017). The parameters used in the model, such as bubble size measurements (GeoB19336-8, GeoB19346-4), molecular gas compositions (GeoB19336-8), and CTD data (GeoB19308-1), were all collected from Mictlan Knoll at 3086 mbsl. For the modeling input, it was assumed that differences in gas composition between the analyzed gas bubbles were negligible at the same emission site at Mictlan.

## 4.4 Results

### 4.4.1 Hydroacoustic data

The bathymetry data acquired during cruises SO174, M67/2 and M114 cover ~52,600 km$^2$ of the seafloor in the southern GoM, ranges from ~ 820 to 3800 m water depth and covers ~60% of the area of the 4S salt province indicated in Fig. 4.1. It includes the four knolls most significant to this study: Chapopote Knoll, Mictlan Knoll, Tsanyao Yang Knoll and Challenger Knoll. The bathymetric map illustrates that the seafloor morphology in this area is characterized by a high abundance of knoll and ridge structures (Fig. 4.2). A general trend from north to south is recognized, where the main seafloor features change from relatively well-defined and isolated knolls in the north to more complex and interconnected ridges in the center and the south. The knolls in the north are typical of circular shape with 5–13 km in diameter and rise 170–650 m above the surrounding seafloor. The ridges in the central area are mainly oriented from SW to NE, extending tens of kilometers in length and rising to 1000 m in elevation. The more complex seafloor morphology in the south consists of coalescing ridges and domes.

The water column data from cruise M114 were used for flare mapping. It covers ~19,600 km$^2$of seafloor in the southern GoM, corresponding to ~30% of the area of the 4S salt province (Fig. 4.2). Based on hydroacoustic data, a total of 209 gas emission sites were identified. Most of them were located above bathymetric elevations such as ridges and knolls within or near the border of the 4S salt province (Fig. 4.2). Flares occurred as 6 individual flares and as 23 flare clusters, each consisting of 2 to 24 flares within a 5 km radius at the ridges along the western border of the Campeche Knolls. The flares indicate the presence of ascending gas bubbles in the water column. Their source points, corresponding to the gas emission sites on the seafloor, were located at water depths ranging from 1,000 to 3,750 meters (Fig. 4.2). The tops of gas flares ranged between 230 and 1,510 m water depth with an average top of all flares at around 805 mbsl (SD=222) (Fig. 4.3).

The flares were found to rise between several hundred and up to several thousand meters into the water column (Figs. 4.4a, 4.4b and 4.4c). Some of the flares could be traced down to the seafloor. A prominent example was observed at Tsanyao Yang Knoll where the ascent of gas bubbles was traced approximately 2900 m above the seafloor at ~ 3400 mbsl (Fig. 4.4b). Many flares showed no hydroacoustic anomalies between the seafloor and mid-water depths of

~2600 – 500 mbsl. For instance, gas bubbles at the Sigsbee Knolls (~3600 mbsl) could only be detected above the 2,600 mbsl (Fig. 4.4c) in the water column.

The correlation between the locations of flare and origins of oil slicks (see section 3.1) at the sea surface was carried out. It showed that 80 % of all (i.e., at 23 of 29) flares or flare-cluster locations co-occurred with origins of oil slicks at the sea surface. In contrast, no indications of gas bubble emissions into the water column were found at several locations (i.e., 39 definite and 30 probable) where origins of oil slicks have been reported by Williams et al. (2006) (Fig. 4.2).

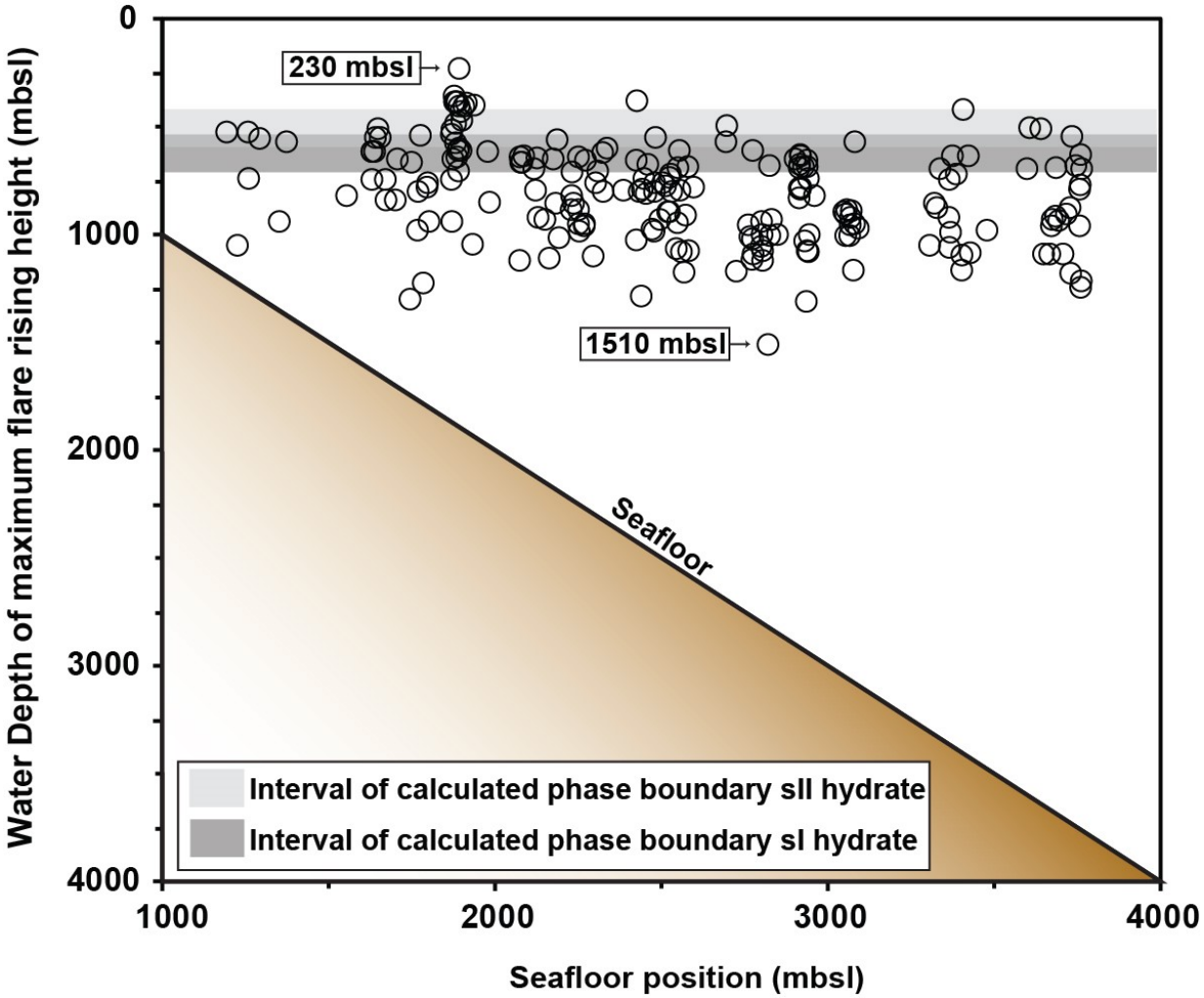


Fig. 4.3. Plot illustrating maximum rising heights of 209 flares (open circles) detected during cruise M114 versus seafloor water depth. Grey zones indicate intervals of calculated boundaries for sI and sII hydrates.

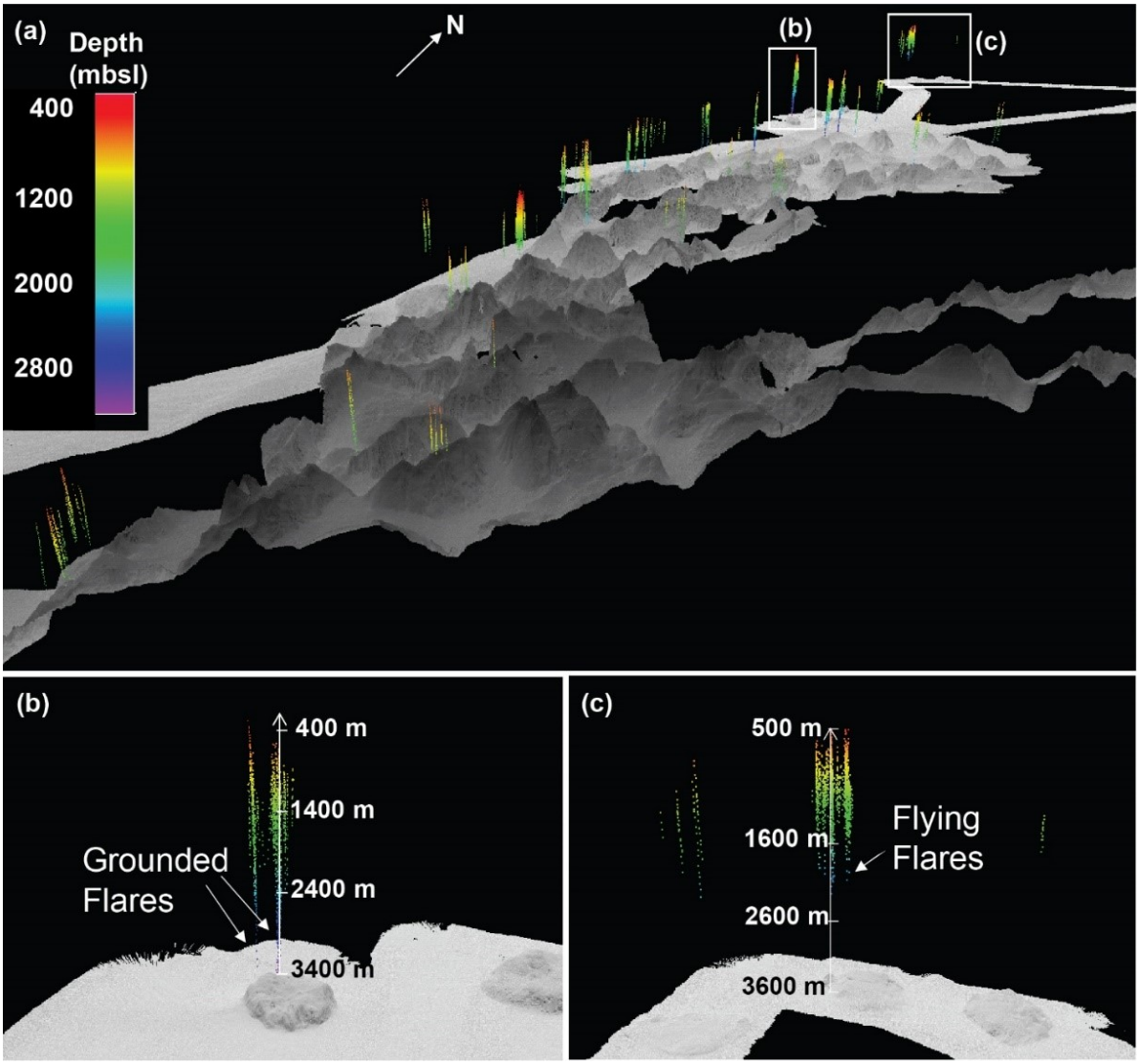


Fig. 4.4. Ship-derived bathymetry (grey-shaded) and flares (colored according to water depth) of the Campeche and Sigsbee Knolls areas acquired and identified, respectively, during cruise M114 and presented as perspective 3D view. (a) Distribution of flares in relation to the bathymetry of the Campeche and Sigsbee Knolls areas, highlighting. (b) Flares above Tsanyao Yang Knoll, which could be traced from water depths of 400 mbsl all the way down to the sources of gas release at the seafloor. (c) Flares above Challenger Knoll, which could be traced from water depths of 500 mbsl all the way down to ~ 2,600 mbsl.

### 4.4.2 Morphological classification of seafloor features

Campeche Knolls and Sigsbee Knolls are characterized by bathymetric highs, forming knolls and ridges of various shapes and extents. Based on their seafloor morphologies and features (Fig. 4.2), 20 knoll-shaped and 23 ridge-shaped structures were classified and grouped into four structural types. These are described in the following as (a) Chapopote-type knolls, (b) Flat-topped-type knolls, (c) Furrow-type ridges, and (d) Asymmetric-type ridges. Besides, the distribution of gas emission sites in there 4 structure types is reported in the following subsections.

#### 4.4.2.1 Chapopote-type knolls

Chapopote-type knolls are circular to sub-circular knoll structures characterized by a central crater-like depression on their crest. In this study, 7 knolls were classified as Chapopote-type knolls. All of them are located in the northern part of the study area (Table 4.1, Fig. 4.2). The most prominent and well–studied knoll of this type is Chapopote asphalt volcano (Fig. 4.5a), therefore, it epitomizes this type of knolls. Chapopote Knoll is located in the northern part of Campeche Knolls (Fig. 4.2). It is a positive structure with a sub-circular basis of ~6 km diameter and with a 60 m-deep and 1.5 km-wide crater at its center. It rises approximately 480 m above the surrounding seafloor from ~ 3,300 m water depth (Fig. 4.5a). The hydroacoustic water column survey lines covering Chapopote Knoll showed that flares predominantly occurred above the rim of the central crater. Only one flare could be traced from the seafloor at ~2,950 mbsl water depth to a height of 650 mbsl. Most of the flares can only be detected above ~2450 mbsl in the water column (Fig. 4.5c), only few gas bubbles were detected below that depth.

A second prominent structure of this type is Mictlan Knoll (Fig. 4.5b). Mictlan Knoll is located 20 km northeast of Chapopote Knoll (Fig. 4.2). It is 7 km in diameter at the base and rises ~300 m higher than the surrounding seafloor of ~3300 m water depth (Fig. 4.5b). The crater-like depression at its top is 1.5 km in diameter and 80 m deep. 11 gas emission sites were found at Mictlan Knoll. They were distributed along the northern and eastern rim of the crater-like depression. In echograms, flares could be traced to a maximum depth of 2450 mbsl, no hydroacoustic anomalies in the water column were detected below ~2450 msbl. Nevertheless, 7 flares reached up to ~900 mbsl, illustrating that gas bubbles were transported more than 2000 m through the water column above Mictlan Knoll.

The remaining knolls of this type are 5–7 km in diameter at the base and rise 300–500 m above the surrounding seafloor. The sizes of the crater-like depressions, present at the top of all of these knolls, range from 1 to 3 km in diameter and 60 to 125 m in depth, respectively. Oil slicks are evident in SAR images above six out of the seven knolls of this type (Table 4.1). Gas flares related to Chapopote-type knolls were only recorded above Chapopote Knoll and Mictlan Knoll during M114.

#### 4.4.2.2 Flat-topped type knolls

Flat-topped type knolls are circular, sub-circular or oval-shaped knolls with a flat morphology on their top. 13 knolls of this type were classified and they were scattered in both Campeche and Sigsbee Knolls (Table 4.1). The diameters and heights of these knolls vary between 7 to 17.5 kilometers and 170 to 730 m, respectively.

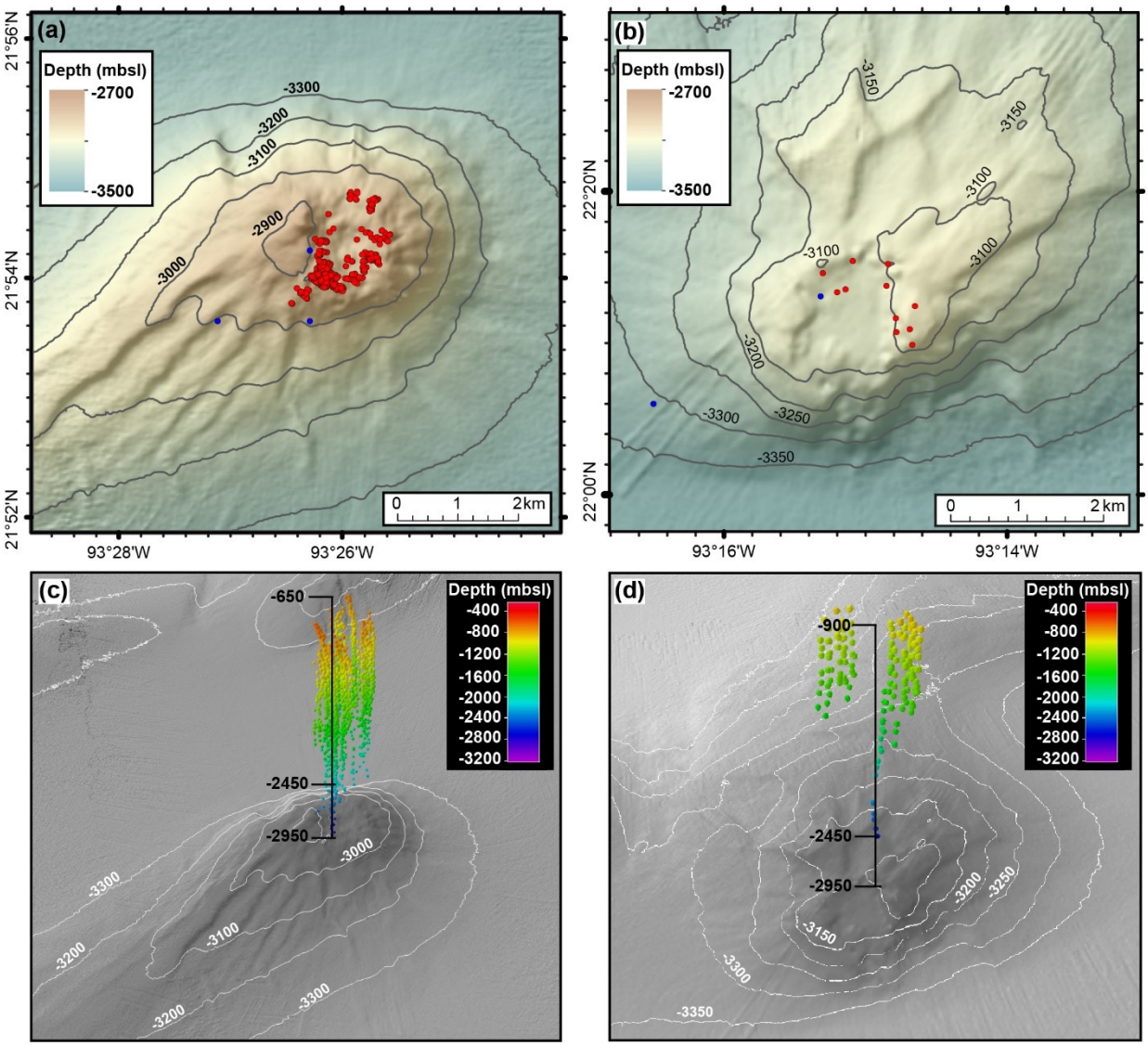


Fig. 4.5. Seafloor maps of selected examples of Chapopote-type knolls. Shaded seafloor bathymetry of (a) Chapopote Knoll and (b) Mictlan Knoll with flare positions projected onto the seafloor (red dots) as determined during cruise M114. Source points of oil seeps are based on the origins of oil slicks at sea surface (blue dots = definite slicks), identified in satellite (SAR) data by Williams et al. (2006), the source points of which have been projected onto the seafloor. c) and d) are perspective views of a) and b), respectively, to indicate the flare heights of up to 2300 m above Chapopote Knoll and 2050 mbsl above Mictlan Knoll.

Eleven knolls of this type showed active hydrocarbon seepage either in the form of oil slicks at the sea surface evident by SAR images or the occurrence of flares (Table 4.1, Fig. 4.2) detected in this study. Flares were found at 6 of the flat-topped type knolls, including Tsanyao Yang Knoll, knoll H2035, knoll H2007, Challenger Knoll, knoll H2327, and knoll H2320 (Fig. 4.6a and 4.6b). In contrast to the flares at the Chapopote-type knolls, flares at the flat-topped type knolls were located near the edge the knolls, as exemplified by Challenger Knoll (Figs. 4.6a and 4.6c). An exception example of flare distribution was at the knoll H2035, where three flares were detected at the flat area on its top (Figs. 4.6b, 4.6d). H2035 is the the largest flat-topped knoll in the study area and it is of oval-shape with a long axis of 17.5 km and a short axis of 9.5 km (Fig. 4.6b), the highest flare at this knoll can reach up to ~500 mbsl (Fig. 4.6d).

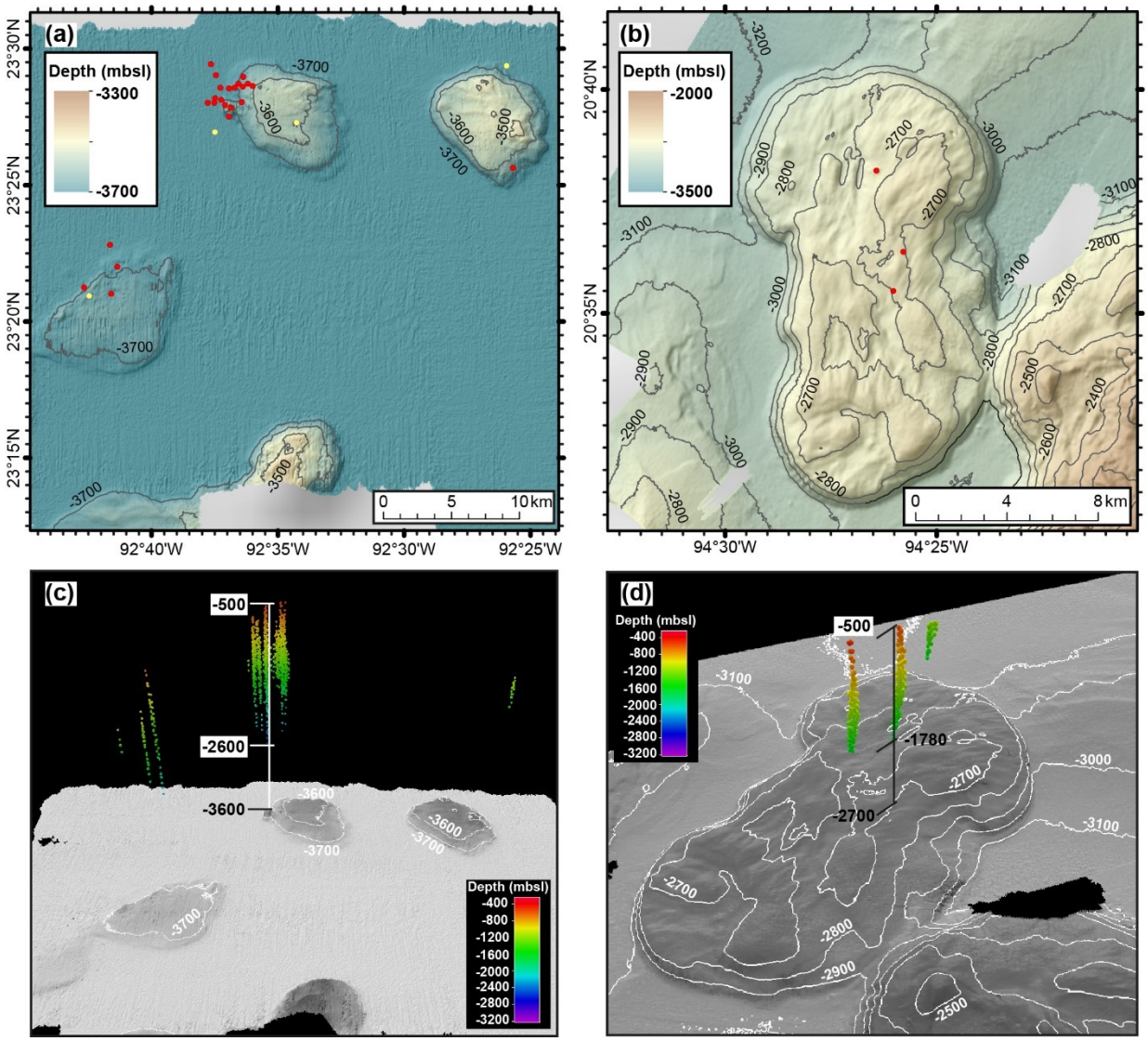


Fig. 4.6. Seafloor maps of selected examples of Flat-topped-type knolls. Shaded seafloor bathymetry of (a) Challenger Knoll and (b) Knoll H2035 with flare positions projected onto the seafloor (red dots) as determined during M114. Source points of oil seeps are based on the origins of oil slicks at sea surface (blue dots = definite slicks), identified in satellite (SAR) data by Williams et al. (2006), the source points of which have been projected onto the seafloor. c) and d) are perspective views of a) and b), respectively, to indicate the flare heights of up to 3100 m above Challenger Knoll and 2200 m above Knoll H2035.

The flat-topped type Challenger Knoll, knoll H2327 and knoll H2320 (Fig. 4.6a) are located in the Sigsbee Knolls area. These knolls are about 10 km wide at their base, sub-circular in shape and rise 170–250 m high from a surrounding abyssal seafloor depth of ~3,750 mbsl. A cluster of 18 flares was detected at the western foot of Challenger Knoll, marking it as the most active site in terms of the number of gas flares within the Sigsbee Knolls area. The echograms showed the hydroacoustic anomalies were detected from the depths of ~2,600 mbsl to ~500 mbsl in the water column (Fig. 4.6c), indicating that gas bubbles traveled more than 3,100 m through the water column at Challenger Knoll.

#### 4.4.2.3 Furrow-type ridges

Furrow-type ridges have been defined as ridges with elongated depressions (furrows) that strike separate it into two crests along the ridge. A total of 16 seafloor features have been attributed to this category (Table 4.1), marking it as the most abundant structural type in our study area. These ridges occur widespread and appear to be randomly distributed across the Campeche area, but were not observed in the Sigsbee Knolls area. Structure H2117 (Figure 7a) is a typical example of a Furrow-type ridge, illustrating that the most obvious characteristic is a depression cutting through the summit of the ridge. Furrow-type ridges range from 12 to 48 km in length and rise from 330 to 1170 m above the surrounding seafloor. In addition, the furrows themselves are normally 30 - 250 m deep depressions cutting the crest of the ridge along its entire length or part of the ridge. Where Furrow-type ridges have coalesced with adjacent ridges or domes, this has resulted in complex structures for which a distinct classification is impossible.

All Furrow-type ridges are associated with either gas emissions or sea surface oil slicks that had been identified from SAR images in earlier studies. Flares were present at 11 Furrow-type ridges and occurred either individually or in clusters of up to 24 flares (e.g. H2036; Fig. 4.7b). Noticeably, flares were distributed either along the depression of the furrow (example.g. H2117; Fig. 4.7a and 4.7c) or along the crest of the ridges (H2036 (Fig. 4.7b and 4.7d)). At structure H2117 for example, flares occurred in the northern part of the furrow along a trend from NE to SW, however, additional flares occur as clusters at the southern crest (Fig. 4.7a and c).

The highest Furrow-type ridge in the study area is structure H2036 (elevation of 1170 m) and it also has the deepest furrow (250 m) separating its two crests (Fig. 4.7b). With more than 20 gas emission sites located along the crest on the western side of the furrow, it was one of the sites with the highest density of active gas emissions detected during cruise M114 in the Campeche area. At structure H2036, most of these flares reached a water depth shallower than 400 mbsl with the highest one peaking at ~250 mbsl (Fig. 7d). This illustrates that the gas bubbles rise up to 1650 m in the water column above their seafloor sources at sites at ~1900 mbsl.

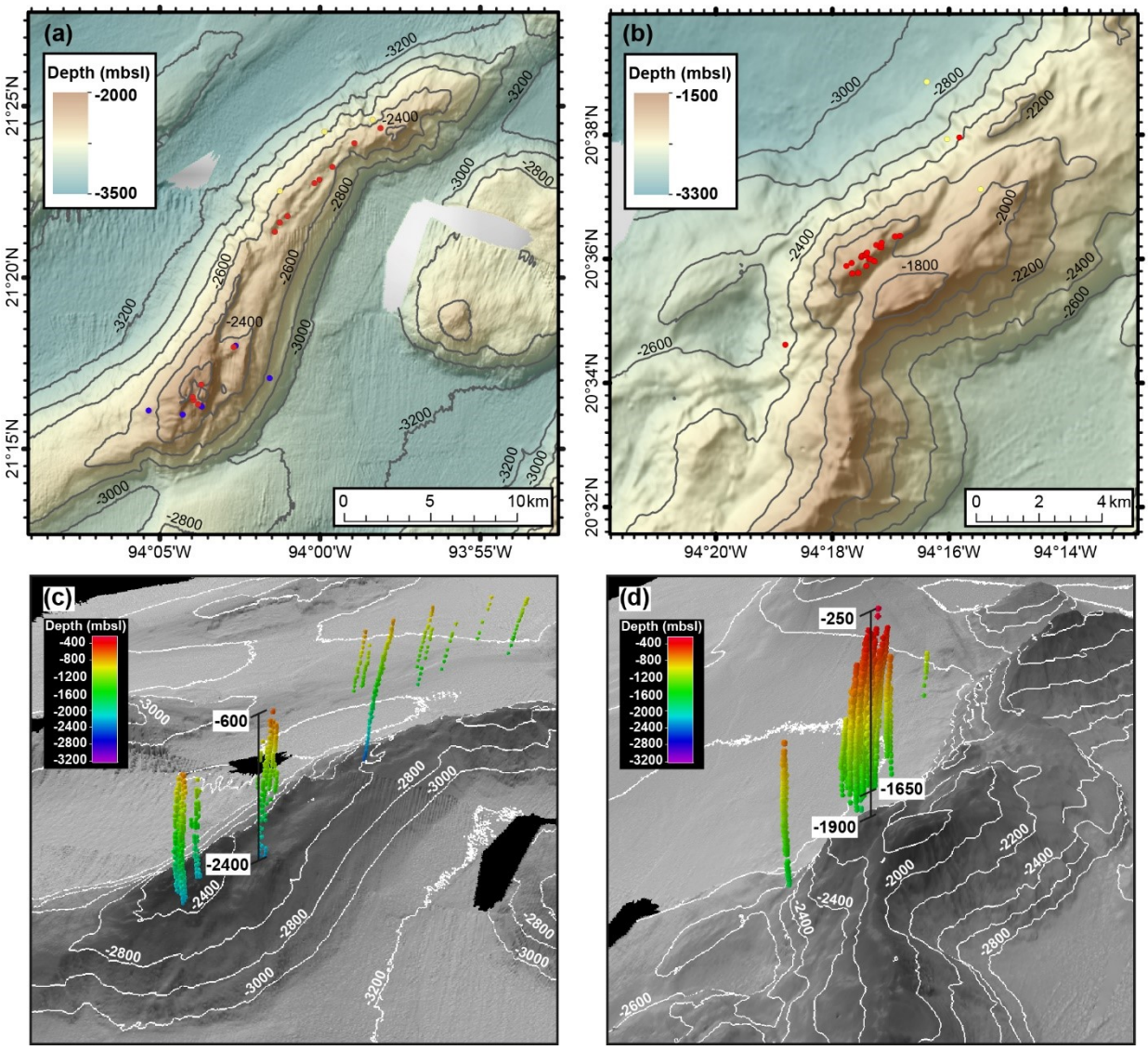


Fig. 4.7. Seafloor maps of selected examples of Furrow-type ridges. Shaded seafloor bathymetry of (a) Ridge H2217 and (b) Ridge H2036 with flare positions projected onto the seafloor (red dots) as determined during M114. Source points of oil seeps are based on the origins of oil slicks at sea surface (blue dots = definite slicks), identified in satellite (SAR) data by Williams et al. (2006), the source points of which have been projected onto the seafloor. c) and d) are perspective views of a) and b), respectively, to indicate the flare heights of up to 1800 m above Ridge H2117 and 1650 m above Knoll H2035.

### 4.4.2.4 Asymmetric-type ridges

Asymmetric-type ridges have been identified based on their seafloor morphology (Fig. 4.8), whereby the key characteristics are differences in the slope angles caused by morphological features such as depressions or bulges on each flank. For example, the slope on the eastern flank of structure H2112 (Fig. 4.8a) is steeper than its western flank, which shows an irregular seafloor expression due to a bulge extending 5 km from the foot of the slope. Similarly, the characteristics of the seafloor morphology at structure H2146 (Fig. 4.8b) consist of a relatively smoother flank along the north and northeast compared to the irregular bulges at the foot of the southern flank. Based on slope angle differences and the smooth vs. irregular

morphological features along their flanks, a total of seven seafloor structures have been identified as Asymmetric-type ridges in our study area (Table 4.1). These ridges range from 10 to 48 km in length and vary between 320 to 1000 m in elevation above the surrounding seafloor.

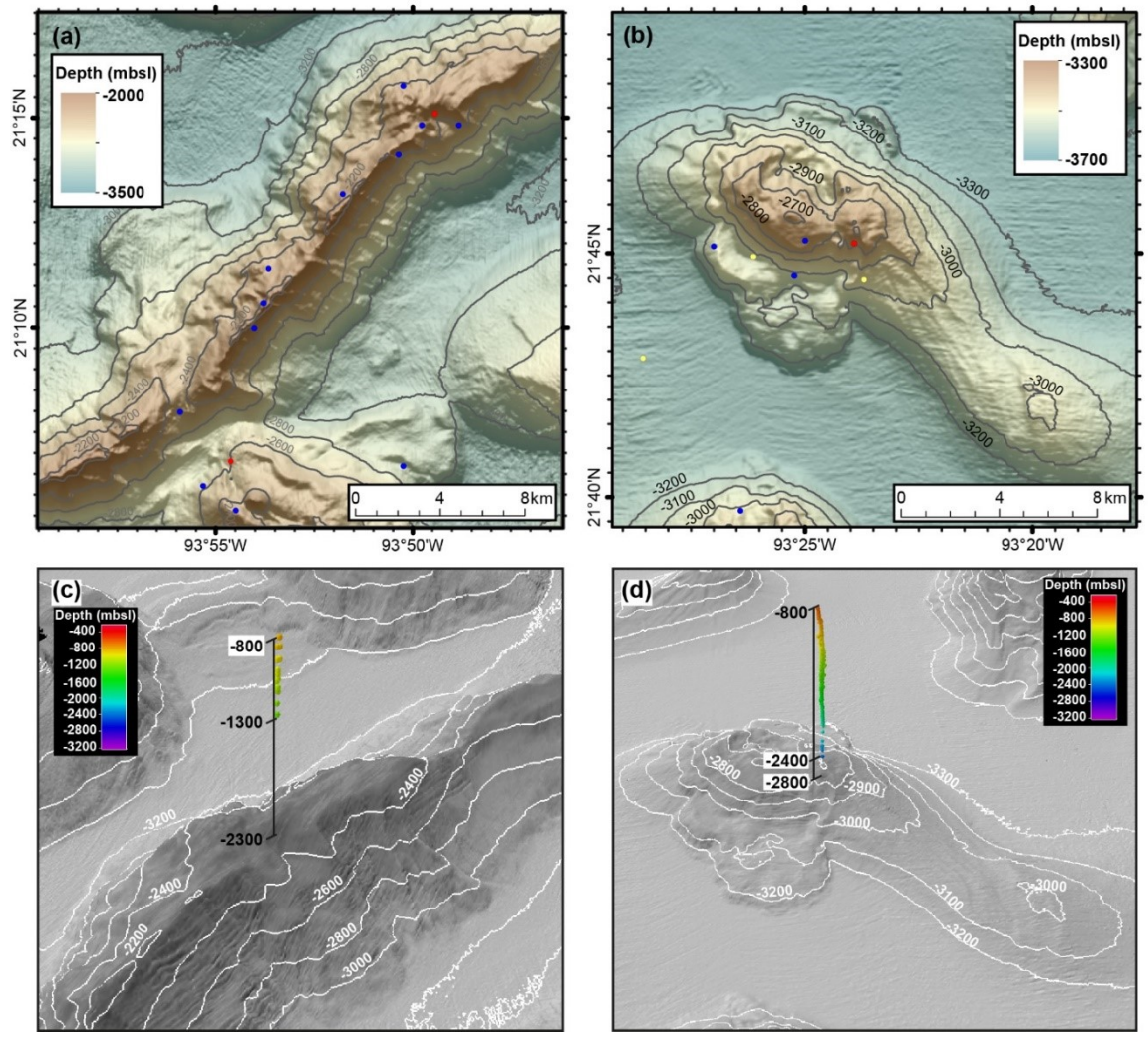


Fig. 4.8. Seafloor maps of selected examples of Asymmetric-type ridges. Shaded seafloor bathymetry of (a) Ridge H2112 and (b) Ridge H2146 with flare positions projected onto the seafloor (red dots) as determined during M114. Source points of oil seeps are based on the origins of oil slicks at sea surface (blue dots = definite slicks), identified in satellite (SAR) data by Williams et al. (2006), the source points of which have been projected onto the seafloor. c) and d) are perspective views of a) and b), respectively, to indicate the flare heights of up to 1500 m above Ridge H2112 and 2000 m above Knoll H2146.

Sea surface oil slicks and flares were generally found above the crests of the ridges or at their chaotic/irregular flanks (Fig. 4.8a and 4.8b). On the crest of structure H2112 (~2320 mbsl), an individual flare was detected from ~800 mbsl to ~1300 mbsl above a circular depression (Fig. 4.8a and 4.8c). At structure H2146, a single flare was detected in the water column from ~2800 mbsl to ~800 mbsl.

### 4.4.3 Gas analyses and calculation of gas hydrate stability

The analyses of gas compositions of samples that were collected by GBS are summarized in Table 4.2. The results show that the molecular composition of light hydrocarbons (methane: ethane: propane: *i*-butane) is 99.48: 0.25: 0.22 :0.05 (mol,%) at the Mictlan Knoll. In this study we calculated phase boundaries for both, the structure I (sI) and structure II (sII) hydrates, which resulted in the upper limit of the GHSZ ranging from 541 to 707 mbsl for sI hydrate and from 407 to 596 mbsl for sII hydrates at respective sites (Fig. 4.9).

Table 4.2. Molecular compositions of gas collected with the Gas Bubble Samplers at individual sites during M114

| Sample code (GeoB) | Site | Methane( mol,%) | Ethane (mol,%) | Propane( mol,%) | *i*-Butane (mol,%) | $C_1/C_2$ |
|---|---|---|---|---|---|---|
| 19318-9 | UNAM Ridge | 97.15 | 1.92 | 0.81 | 0.12 | 34 |
| 19325-13 | Chapopote Knoll | 97.87 | 1.62 | 0.43 | 0.08 | 46 |
| 19336-8 | Mictlan Knoll | 99.48 | 0.25 | 0.22 | 0.05 | 192 |
| 19337-12 | Tsanyao Yang knoll | 95.34 | 3.19 | 1.07 | 0.40 | 20 |

### 4.4.4 Gas bubble analyses and modeling results

Video footage of rising gas bubbles was analyzed at a gas hydrate mound located in the central area of Mictlan Knoll, where bubbles were continuously emitted in a clearly defined stream. The gas bubble sizes ranged from a minimum radius ($r_e$) of 1.4 mm to a maximum $r_e$ of 4.4 mm, with an average $r_e$ of 2.92 mm (SD = 0.6). Based on this dataset and the gas compositions described in the previous chapter, a single bubble dissolution model was applied to calculate the fate of methane in the water column. Whereas the full simulation results are shown in Table. 4.3, it was found that bubbles of the maximum size ($r_e$ of 4.4 mm) can rise up to 850 mbsl, bubbles of average size ($r_e$ of 2.9 mm) could reach the depth of up to 1955 mbsl, and bubbles of the minimum size ($r_e$ of 1.4 mm) can only reach the depth of 2810 mbsl.

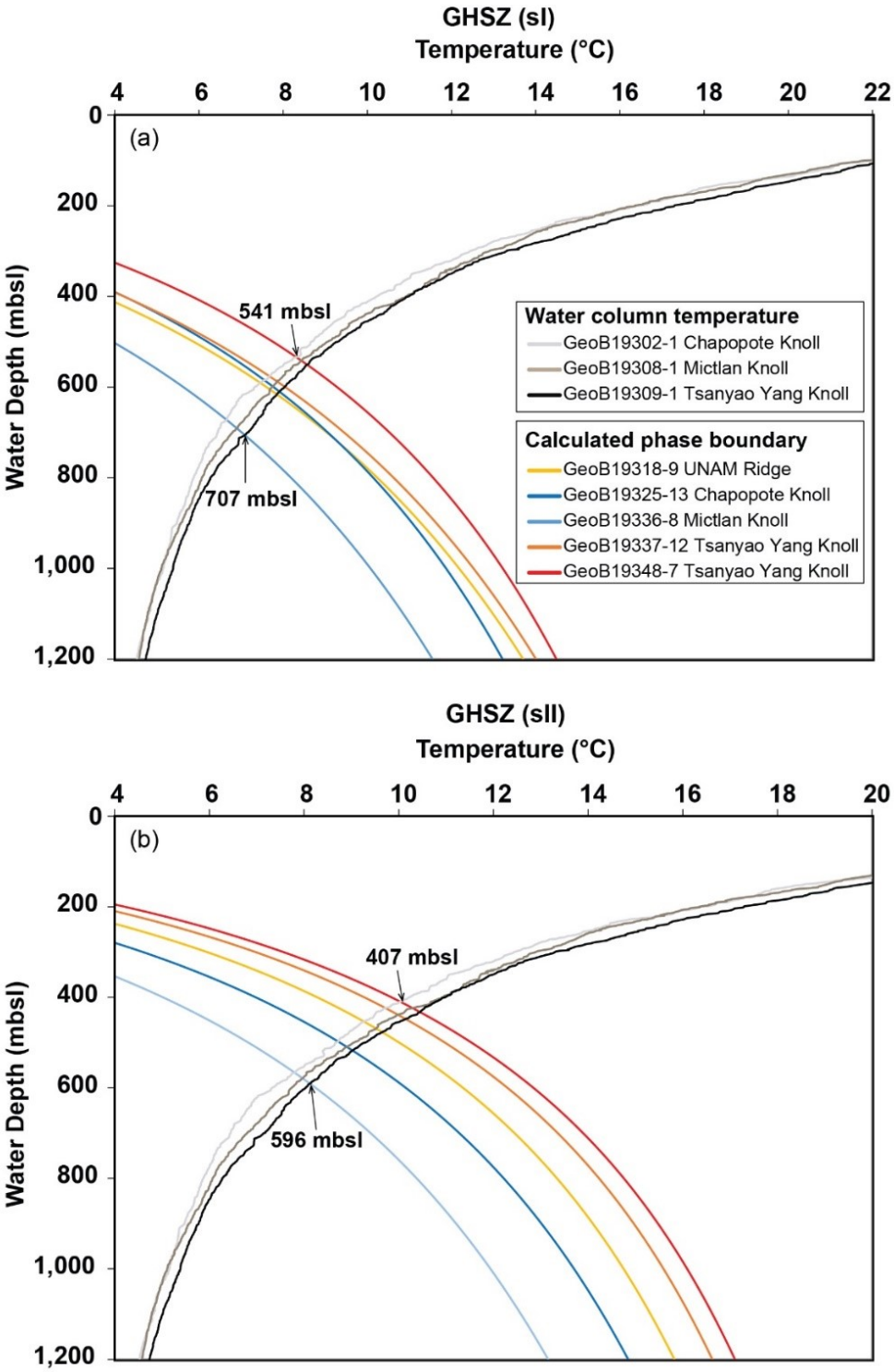


Fig. 4.9. Phase diagrams of the gas hydrate stability zone (GHSZ) computed based on physical data (temperature, salinity and conductivity) obtained from CTD casts during cruise M114 and the composition of gas sampled by pressure-tight gas bubble samplers during ROV operations. The points of intersection define the upper boundaries of the GHSZ. The upper boundary of the GHSZ for structure I (a) and structure II (b) hydrate in southern GoM is between 541 ~ 707 mbsl and between 407 ~ 596 mbsl.

Table. 4.3 Parameter settings for the Texas A&M Oil spill Calculator (TAMOC) single bubble model considering data from Mictlan Knoll.

| | |
|---|---|
| Initial depth | 3086 mbsl |
| Hydrate film formation time | 0* second |
| Bottom water temperature | 277.15 K |
| Ambient water condition (CTD data) | GeoB19308-1 |
| Bubble equivalent spherical radius | |
| Maximum | 4.4 mm |
| Minimum | 1.4 mm |
| Average | 2.9 mm |

*In this model we assume that the gas hydrate film forms simultaneously while gas bubble release from seafloor

## 4.5 Discussion

### 4.5.1 Distribution of flares in the Campeche and Sigsbee Knolls

The Campeche (e.g., MacDonald et al. (2004), Ding et al. (2010), and Sahling et al. (2016)) and Sigsbee Knolls (e.g., Ewing et al. (1969a)) formed the Campeche-Sigsbee salt province in the southern GoM. This region is known to be associated with active hydrocarbon seepage similar to the major hydrocarbon systems linked to salt tectonism in the northern GoM (Garrison and Martin 1973). Salt domes, salt stocks and salt ridges, are known to have affected salt-overlying sedimentary successions, the seafloor morphology and the hydrocarbon system throughout major parts of the northern GoM (Bryant et al. 1991; Salvador 1991a). In the southern GoM, however, studies focusing on the relationship between seafloor morphological structures and the distribution of hydrocarbon seepage on a regional or basin-wide scale are lacking. Systematic and extensive hydroacoustic surveys performed in this study revealed that gas emission sites were distributed across a wide area and a broad range of seafloor structures and morphologies in the Campeche and Sigsbee Knolls areas (Fig. 4.2 and 4.3a). Mapping at resolutions that are capable of revealing seafloor features as small as tens of meters in diameter, allowed to classify four types of seafloor structures based on their morphologies and to accurately localize the sites of gas release at the seafloor for the first time.

In the following, we discuss the occurrences of flares and origins of oil slicks at the sea surface in the Campeche-Sigsbee salt province and the potential relationships between emission sites at the seafloor and morphological structures. We propose conceptual models of gas migration for the four defined structural types that focus on the relationship between distributions of gas emission sites and seafloor morphology (Fig. 4.10). Finally, we put the characteristics of the

flares and seepage sites into context with their respective water depths to study possible gas hydrate formation processes.

At 80% (23 of 26) of the structures investigated in this study, gas flares, as well as oil slicks, occurred, respectively, in the water column and at the sea surface. Hydrocarbon leakage in the southern GoM has previously been documented by repeated sightings of numerous natural oil slicks at the sea surface (MacDonald et al. 2015; Suresh 2015; Williams et al. 2006) and by investigations of selected seafloor gas and oil emission sites (Brüning et al. 2010; Hsu et al. 2019; Sahling et al. 2016). However, the distribution of gas emission sites has not been systematically investigated in these regions, so far. A total of 209 flares was detected during the 6 weeks cruise of M114 in an area of ~19,600 $km^2$, showing the evidence for the current gas seepage in this salt province. Additional evidence of past and recently ongoing hydrocarbon seepage in the southern GoM comes in the form of asphalt deposits, which cover areas of up to several thousand square meters on the seafloor at the Campeche Knolls (Brüning et al. 2010; Marcon et al. 2018). Such deposits result from tar-like fluids, which are related to the discharge of heavy bitumen (a thick form of petroleum) from an underlying hydrocarbon system.

By integrating our systematic hydroacoustic surveys and newly acquired seafloor bathymetry with existing satellite data (SAR) on oil-slick distributions (Williams et al. 2006), we find that gas emission sites are not randomly distributed across the Campeche and Sigsbee Knolls areas, but are related to four structural types identified and newly defined in this study. Whereas the particular characteristics of each structural type will be discussed in the following chapters, the distribution of the majority of the gas emission sites appears to be closely linked to potential fluid migration pathways resulting from salt diapirism, such as normal faults, basins, and zones where salt deposits have been thinned or are absent due to sediment movement (e.g., uplift). These findings are based on the comparison of the gas emission sites with our newly acquired seafloor bathymetry as well as previously published seismic lines across several of the structures (Ding et al. 2010). Based on seafloor bathymetry and 2D seismic data as well as oil slick distributions, those authors proposed that hydrocarbon seepage at the Campeche Knolls is the result of salt tectonism that has affected the sediment structures overlying the salt deposits (Ding et al. 2010). Salt deposits are known for their qualities to form geological seals, which may prevent fluid migration, and form structural traps, hence influencing reservoir distributions in the subsurface (Hudec and Jackson 2007). In contrast, salt bodies may also be prone to fluid leakage in particular in relation to sediment uplift or diapir formation, where fluids typically escape at the edges of basins or in between of salt uplifts (Warren 2017).

The ROV guided visual seafloor inspections during the M114 cruise in the southern GoM showed that gas and oil release occurred from the seabed, but a clear distinction between gas bubbles, oil drops, and oil-coated gas bubbles was not always possible (Sahling et al. 2016). From the northern GoM, it is known that oil seeps usually also emit natural gas (Aharon and Fu 2000; Kvenvolden and Rogers 2005; Leifer 2010).

#### 4.5.1.1 Chapopote-type knolls

The most obvious morphological characteristic of Chapopote-type knolls is a circular to sub-circular geometry with a crater-like depression on the crest (Fig. 4.10a). At 2 of 7 structures of this type, flares were documented during cruise M114 and satellite imagery revealed oil slicks at 6 knolls of this type from Williams et al. (2006) (Table 4.1)

Asphalt volcanism exists at two of the Chapopote-type structures and oil slicks indicate active oil seepage from the crater-like depressions at all but one of the structures. During M114, gas emissions into the water column occurred predominantly from along the rims of the central craters on top of the structures (Fig. 4.5a and 4.5b). Two typical examples of Chapopote-type knolls are the structures referred to as Chapopote Knoll and Mictlan Knoll. The release of gas bubbles points to the presence of fluids oversaturated in gas, which accumulate in the subsurface and are actively focused along discrete pathways. Chapopote Knoll in particular, has been argued to overlay a reservoir-seal system for hydrocarbons (Ding et al. 2008). Seismic studies by Ding et al. (2010) indicated that two Chapopote-type knolls share a domed coarse-grained reservoir covered by a thin (100-200 m) layer of fine-grained sediment acting as a seal, which formed a classical structural trap and allowed hydrocarbon accumulation within the knoll. The thin and unconsolidated sediment allowed hydrocarbons to intrude below the seal intervals near the crest of the knoll (Ding et al. 2010). Consequently, the intrusive hydrocarbons may form a shallow reservoir. Based on the systematic arrangement of seepage sites discovered along the rims of the craters at Chapopote-type Knolls, we interpret that fluid migration occurs through the knolls and is focused upwards towards the crater-like depressions on top of the structures.

Furthermore, the loss of material (i.e., fluids) from the subsurface is proposed to explain the formation of crater-like depressions on top of Chapopote-type structures. The crater-like depressions on top of Chapopote and Mictlan are known to be partially filled by asphalt fields resulting from the extrusion and deposition of tar-like fluids through processes of asphalt volcanism (MacDonald et al. 2004; Marcon et al. 2018; Sahling et al. 2016). In addition, a particular mechanism to explain the crater-like depression has previously been proposed for Chapopote Knoll, where it has been argued that sediments collapsed after hydrocarbons moved upwards and were released from a sub-seafloor reservoir located in strata overlying the salt diapir (Ding et al. 2010).

At Chapopote Knoll and Mictlan Knoll, the edges of the asphalt fields coincided with the rims of the crater-like depression. Visual seafloor inspections by ROV confirmed the release of oil drops (black color) or oil-coated gas bubbles (brown color) from the seafloor at sites from within cracks or in close proximity to the asphalt deposits (Sahling et al. 2016). In contrast, sites of gas bubble release (colorless) were encountered only at the edges of the asphalt field or from sediments along the edge of the asphalt field (Sahling et al. 2016). Based on the above findings, we propose a conceptual model for seepage at the Chapopote-type knolls, in which ascending gas encountering the asphalt deposits in the crater-like depression from below, is laterally diverted and eventually escapes at the edge of the asphalt field (Fig. 4.10a). A few flares and sites where oil-coated bubbles are released occur in the central parts of the crater-like depression (Fig. 4.5a). These sites may represent areas where there are gaps or cracks in the otherwise tight seal formed by the asphalt deposits. Solid asphalt deposition and gas hydrate formation are known to reduce the permeability along migration pathways of fluids, forming

temporal seals, and potentially cause a lateral shift of the fluid migration pathways (Ding et al. 2008; Kleinberg et al. 2003; Tryon et al. 2002). Furthermore, our interpretation that asphalt deposits are capable of forming a seal in the form of a seafloor pavement is supported by a previous study (Marcon et al. 2018), which reports that the asphalt deposits are up to several meters thick and consist of several overlapping flows.

An alternative scenario of gas migration and release along the crater rims could involve fluid-migration pathways along ring faults of the collapse-depression. This process is known from mud volcanoes, which extrude a mixture of sediments and fluids through their plumbing systems, where the material loss in the subsurface can lead to the formation of caldera-like craters surrounded by inward-dipping ring faults (Loher et al. 2018c; Mazzini et al. 2009; Planke et al. 2003). Such ring faults have recently been found to act as potential fluid migration pathways forming upward-branching plumbing systems at deep-sea mud volcanoes (Loher et al. 2018c). Whereas we find the flare locations at Chapopote Knoll and Mictlan Knoll to be distributed along the rim of the crater-like depressions, we do not find evidence of inward-dipping ring faults in the seafloor bathymetry and neither do the seismic data by Ding et al. 2010 indicate faults reaching the seafloor in the cap-sediments of Chapopote Knoll. Nevertheless, we cannot completely discard the possibility of the influence of faults as potential fluid migration pathways extending through sediments on top of the diapir. In addition, the type of seepage activity (quiescent gas bubbling, oil drop release, and slow asphalt volcanism) does bear similarities to quiescent phases of mud volcanoes in terms of the mechanism for hydrocarbon seepage.

#### 4.5.1.2 Flat-topped type knolls

The top areas of these types of knolls are characterized by a flat seafloor morphology. During our investigations in 2015 (Fig. 4.6a) flares were distributed or clustered around the edges at the foot of the knoll structures, i.e., at the seafloor transition from the knoll structures and the normal seafloor, with few exceptions. This finding accords with earlier observations in the northern GoM where it was found that gas emissions typically occur on the edges of domed structures caused by salt diapirism (Hood et al. 2002; Weber et al. 2014). Seismic investigations across several flat-topped-type knolls including Challenger Knoll (Ewing et al. 1969a; Ladd et al. 1976) and knoll H2119 (Ding et al. 2010; Shipley et al. 2005), indicated that their internal structure represents passive salt diapirs, consisting of wide salt stocks at sub-surface. In cases where salt rises upwards and breaks through its overburden sediment (Hudec and Jackson 2007; Warren 2017), salt tops tend to spread out laterally as there is essentially no confinement above the top of the salt (Ding et al. 2010; Rowan et al. 2003). Given the large surface area extent of flat-topped-type knolls, we, therefore, interpret that the flat seafloor expression at the top of these types of structures results from the lateral spreading of salt. Interpretations of seismic data across Challenger Knoll (Ewing et al. 1969a) and knoll H2119 (Ding et al. 2010) for example have shown salt deposits at levels covered by no more than 150 m and 10 m of overburden sediments, respectively. We argue that the extensive and impermeable salt cap inhibits hydrocarbon migration to and seepage at the flat top of the knoll. In addition, the presence of a thin interval of overburden sediment appears not to be enough to host a sub-seafloor reservoir located in strata overlying the salt diapir as proposed for Chapopote-type knolls. Instead, this supports the idea that hydrocarbons, e.g. originating from

reservoir intervals deeper than what has been resolved in seismic data by Ding et al. (2010), may migrate along the salt-sediment interface along the flank of the salt diapirs and escape at the periphery of the knolls. One exception, however, was found at knoll structure H2035, where gas emission sites not only occurred at the periphery of the knolls but also at the top of the knoll (Fig. 4.6b). This suggests that alternative fluid migration pathways exist, which facilitate hydrocarbon upward migration to the top of the knolls. Gas escape may occur where gas has migrated along the salt-sediment boundary of thicker (i.e.,>10 m) intervals of overburden sediments to the tops of salt diapirs and where the structural integrity of these sediments has been compromised by normal faults. This interpretation of such a potential mechanism warrants further investigations, given the lack of seismic data for knoll H2035. Nevertheless, we propose a conceptual model for seepage processes at flat-topped-type knolls, where we include two potential gas migration and release pathways (Fig. 4.10b). A first involves hydrocarbon migrating along the salt-sediment interface from depth and release at the edge of the knoll at the seafloor. A second involves a longer migration pathway along the sediment-salt interface to the shallow sub-surface on top of the knoll, where normal faults provide structural weaknesses through which gas may escape.

#### 4.5.1.3 Furrow-type ridges

Furrow-type ridges are elongated morphological structures most of which show heights/areal extents/widths larger than the isolated knolls (i.e., Chapopote-type and Flat-topped-type knolls) in our study area. In regions affected by salt tectonics, differences in size and shape of the existing morphological structures are typically caused by the development of the underlying salt structures (Hudec and Jackson 2007). In the northern GoM, for example, elongated ridges have formed by the rise of line-shaped diapiric subsurface structures such as salt anticlines or salt rollers, whereas knolls have risen from point sources. The shapes and sizes of diapirs are also related to their age and stage of development as has been suggested for salt structures in the northern GoM, where they tend to become smaller and more circular with increasing age (Jackson and Talbot 1986). Assuming a similar mechanism for the southern GoM, the greater number of isolated knolls in the Sigsbee and the northern regions of the Campeche areas indicates that those structures are older than the complex and irregular ridges in the southern parts of our study area.

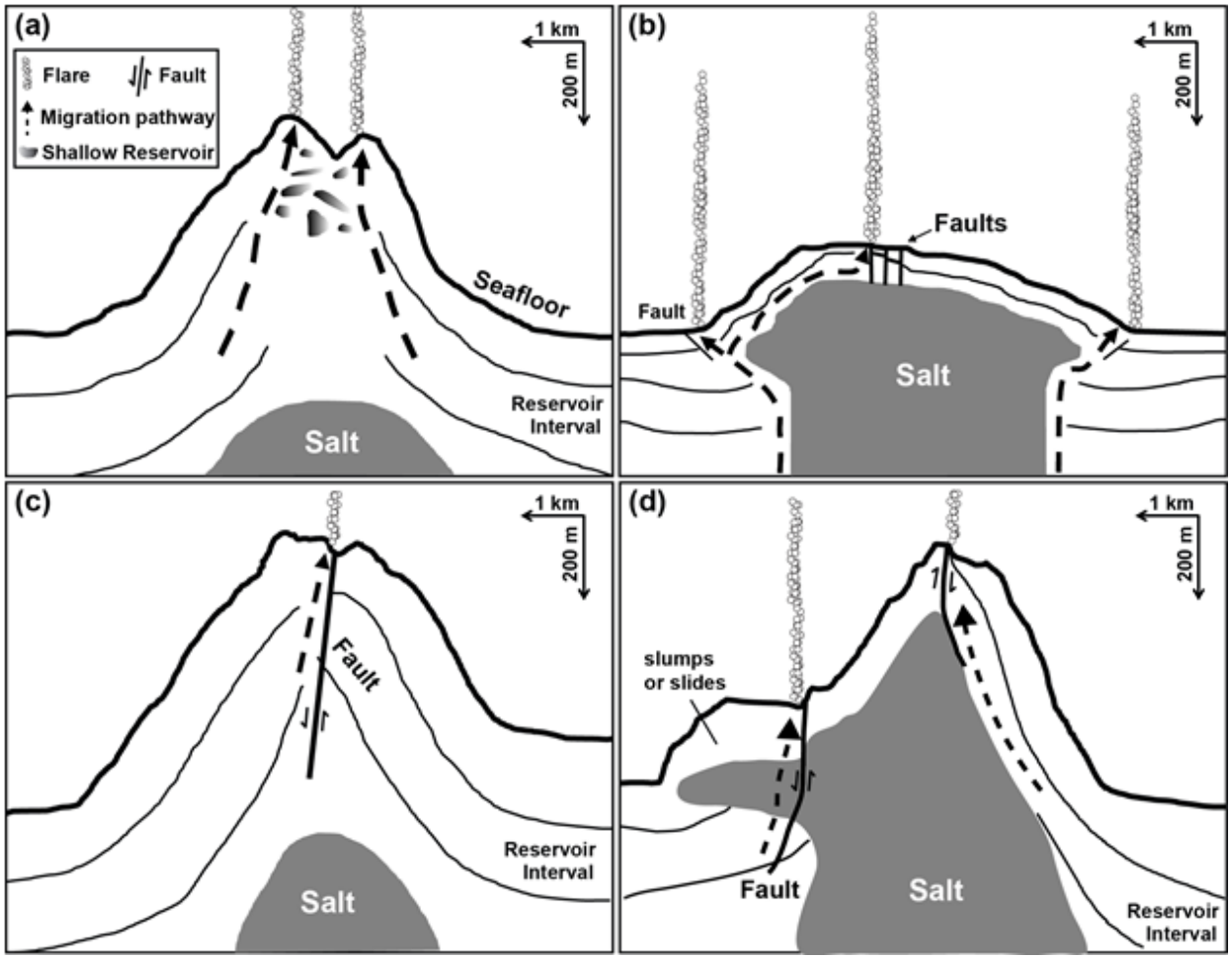


Fig. 4.10. Schematic cross sections through the four individual knoll and ridges types illustrating conceptual fluid migration and release models (see also text for details) (a) Chapopote-type knolls: hydrocarbons migrate from the reservoir interval overlying the salt deposits into sediments below the crest, where solid asphalt and gas hydrate deposits have limited the permeability of vertical fluid migration. The fluids encounter the asphalt field as a barrier and are trapped, accumulate, and are diverted towards the edge of the asphalt field, which results in gas emission sites located along the rim of the crater. (b) Flat-topped type knolls: the lateral spreading of salt in the sub-surface inhibits vertical fluid migration, whereas the salt-sediment interface potentially provides fluid migration pathways. Accordingly, most gas emission sites are located around the edge of the knoll. In addition, faults located on the flat tops of the knoll might facilitate gas release in more central parts. (c) Furrow-type knolls: the furrow-like depression is most likely the result of a fault related to differential salt movement in the subsurface. The fault system possibly provides an effective pathway for fluids to migrate from the reservoir interval towards the furrow or the crest where the seeps have been detected. (d) Asymmetric-type knolls: Two potential fluid migration pathways are suggested, to explain the observed seepage at the crest and along the chaotic flank. The depths and geometries of the salt in Fig. 4.9 are depicted schematically following Ding et al. (2010).

The key morphological characteristic of Furrow-type ridges is an elongate depression, extending across the length of the structure and bifurcating the top into two crests. Previous studies in the southern GoM have shown that elongated furrows across diapir-related morphologies represent the surface expression of normal faults which may cut along the entire length of a ridge (Ding et al. 2010). In this study, the spatial distribution of flares above the Furrow-type ridges was shown to be related to the furrow-like depression (Fig. 4.7). These depressions closely resemble the surface expression of salt sheets moving upwards at differential speeds, typically causing fault systems in overlying sediments (e.g. Warren (2017)and their Fig. 13B). Flares were located either along one or both of the ridge-crests or in sub-parallel alignment along the furrow-like depressions. In our conceptual model for seepage processes at Furrow-type ridges (Fig. 4.10c), we therefore propose a spatial link between flare origins at the seafloor and the normal fault systems represented by the furrows. The distribution of gas and oil seep sources on top of the Furrow-type ridges in our study suggests that such faults represent efficient conduits, allowing fluids to migrate from reservoir intervals up to the seafloor. Furthermore, the edges of so-called depopods, which are sediment-filled basins located on or in between salt uplifts and which have been defined in their type area in the northern GoM, have previously been found to be associated with fluid leakages in other offshore salt provinces, where they typically are expressed by mud mounds, chemosynthesis-based ecosystems, gas chimneys or pockmarks (Andresen et al. 2011; Bowman 2011; Cartwright et al. 2007; Warren 2017). Our conceptual model of hydrocarbon seepage along fault systems also supports previous findings in the Nankai Trough (Le Pichon et al. 1992) or offshore Oregon (Moore et al. 1990), where the seepage occurs through normal faults at structures resembling the Furrow-type ridges. Similarly, Dupré et al. (2015) have reported that gas emissions preferentially follow traces of active normal faults in the Sea of Marmara and in particular that they occur along a strike-slip segment of the Main Marmara Fault.

#### 4.5.1.4 Asymmetric-type ridges

Ridges are characterized by strong morphological differences along each flank, have been identified and defined as Asymmetric-type ridge in this study. However, the term Asymmetric-type has first been introduced based on for ridges in the southern GoM, where seismic investigations by Ding et al. (2010) have shown certain structures to consist of sediment successions with relative constant thickness but which have been more strongly uplifted at one flank than at the other. The classification of Asymmetric-type ridges presented in this study, therefore, also considers the findings by Ding et al. (2010) to achieve a complete definition. For instance, ridges H2112 and H2146 have been defined as Asymmetric-type based on our morphological criteria of differential slope angles as well as similarities in internal structures as described by Ding et al. (2010).

The seafloor bathymetry analyzed in this study is of high enough resolution to show the ridge crests of Asymmetric-type structures to host complex mini-basins and in most cases, positive morphologies (i.e., bulges) at one of the flanks or the foot of one side of the ridges. It appears that the morphological appearance of Asymmetric-type ridges is closely associated with the degree of deformation. This supports a formation scenario proposed for Asymmetric-type ridges by Ding et al. (2010), who suggested that complex deformations including mini-basin subsidence, salt evacuation and normal faulting at the ridge crests formed the present seafloor

structures. Our results of the distribution of gas emissions sites at the ridges show that gas was found to emanate predominantly at the crests or at the more chaotic flanks along the ridge structures. Our findings confirm what had previously been speculatively proposed by Ding et al. (2010) that the occurrences of hydrocarbon seepage favored at the crest and the chaotic flank due to the presence of sediment structures overlying the salt deposits that allow for the accumulation of subsurface fluids.

In this study, we propose a conceptual fluid migration and release model for a strongly deformed Asymmetric-type ridge (Fig. 4.10d). As the Asymmetric-type ridges comprise seal intervals both at their uplifted and at their chaotic flanks, where reservoir intervals have been turned upwards, we therefore propose two possible hydrocarbon migration pathways in the subsurface. The first involves fluid migration along the seal-forming salt deposits and the uplifted reservoir interval, which provides a pathway for fluids to migrate from depth to the crest of the ridges. Whereas the uplifted flanks have been argued to generally lack effective structural traps to accumulate hydrocarbons by Ding et al. (2010), seepage may still occur by involving fluids that have accumulated at depths greater than the presently available seismic data. The second illustrates seepage at the morphologically more irregular flanks. In these cases, fluid release occurs from where hydrocarbons have been trapped below salt deposits or by thicker overlying sediments forming a seal. This structural arrangement is argued to be the result of lateral salt intrusions into shallow sediments above the reservoir interval. Salt intrusions above reservoir intervals are a typical mechanism to form hydrocarbon traps where thick sealing sediments overlie the salt (Harding and Lowell 1979). Similar structures are also known in association with salt diapirs in the northern GoM (Rowan et al. 2003), where salt has spread horizontally, lacking significant confining sediments on top of it, and formed structural traps for fluids. We argue that seafloor deformations resulting from lateral salt intrusions have given rise to complex seafloor morphologies (e.g., bulges) along the chaotic flanks. The surface morphology of the chaotic flanks may additionally be affected by slumps or slides driven by faults in the flanks, which have now been pushed upwards (Fig. 4.10d). Seafloor seepage at the chaotic flanks thus occurs where the salt seals are absent, the integrity of the otherwise effective salt seal has been compromised (e.g., by faults), or where overlying sediments are too thin and fail to inhibit fluid migration.

### 4.5.2 Characteristics of gas flares in relation to gas hydrate stability

The results of our hydroacoustic observations in the water column show numerous flares that rise more than 2000 meters from the seafloor in our study area in the southern GoM (Fig. 4.3). The highest flare was traced over 3,100 meters through the water column above Challenger Knoll, where it originated at ~3,600 mbsl (Fig. 4.6c). The hydroacoustic water column anomalies detected in our study represent gas flares that rank among the highest on record to date, compared to investigations in regions including Cascadia margin (Heeschen et al. 2003), Makran continental margin (Römer et al. 2012b), or Håkon Mosby Mud Volcano in Norwegian–Barents–Spitzbergen continental margin (Sauter et al. 2006) where the highest flares have indicated rising gas bubbles over distances less than 1200 meters through the water column. Previous studies have suggested that flares often disappear from the echosounder records near or shortly above the upper boundary of the GHSZ (Heeschen et al. 2003; Römer et al. 2012b; Sauter et al. 2006). To test this hypothesis in the southern GoM and to investigate the

rising limitations of bubbles discharged into deep waters, we documented the highest rising levels from a total of 209 flares. As shown in Fig. 4.3, the upper limit of flares was located at water depths between 230 to 1510 mbsl with an average water depth of 805 mbsl. Comparison of the calculated phase boundaries and flare heights determined during water column surveys showed that most of the flares did not reach the upper stability boundary for structure I hydrate (Fig. 4.3). Moreover, only few of the flares were traced above the stability limit of sII hydrates.

In principle, methane bubbles are dissolved rapidly after they have been discharged at the seafloor since ocean water is highly under-saturated concerning methane (McGinnis et al. 2006). If gas emissions occur from seafloor areas within the hydrate stability zone, however, methane bubbles may be protected from being dissolved by hydrate skins, which can form as soon as the gas bubbles get in contact with water (Brewer et al. 2002; Rehder et al. 2002). Furthermore, hydrate skin formation has been found to be responsible for the characteristic porous bubble fabric of hydrate deposits sampled for the first time at Hydrate Ridge in 1998 (Bohrmann et al., 1998; Suess et al., 2001). The trapping and accumulation of gas-hydrate coated bubbles have been observed at several other locations such as Tsanyao Yang Knoll or Mictlan Knoll and it is believed that this process can lead to the build-up of gas hydrate deposits or mound of several meters in height and extent (Römer et al. 2019; Sahling et al. 2016). This shows that where free gas emanates from the seabed into the ocean water and ascending gas bubbles become coated by hydrate skins, these protect or at least reduce the rapid dissolution of the methane in the highly methane-under saturated water (Rehder et al. 2009). Once the bubbles reach the upper boundary of the GHSZ, however, the dissolution rate of residual methane in the bubbles rapidly increases (Heeschen et al. 2003).

It should be stressed, however, that buried gas hydrates recovered from Chapopote Knoll have been reported to consist of either pure sI hydrate or of co-existing sI and sII hydrate structures (Klapp et al. 2010). Sahling et al. (2016) reported hydrocarbon ratios ($C_1/C_2$) ratio for discharged gases collected at UNAM Ridge (34, GeoB19318-9), Chapopote Knoll (46, GeoB19325-13), Mictlan Knoll (192, GeoB19336-8) and Tsanyao Yang Knoll (20, GeoB19337-12), indicating higher hydrocarbons such as propane and *i*-butane. These hydrocarbons are typical components of thermogenic natural gases, and due to their molecular sizes, typically lead to the incipient formation of hydrate crystal structure sII (Sloan 1998). Thus, we suggest that hydrate skins enveloping bubble-forming hydrocarbons in our study area consist of sII hydrate, which would explain how gas bubbles can rise close to or slightly above the respective upper stability boundary (Fig. 4.3).

### 4.5.3 Hindcast modeling of the fate of gas bubbles released at Mictlan Knoll

During cruise M114 the highest flares documented in echograms at Mictlan Knoll reached up to ~ 900 mbsl (Fig. 4.5), which matches the modeling result for the maximum rise height of large-sized (i.e., 8.8 mm diameter) bubbles. This suggests that the sizes of bubbles play a key role in their rising height. Further simulation results suggest that the molecular composition of the gas also significantly influences the bubble rising height (Table 4.4). Overall, these results indicate that the larger size bubbles and the gas bubble composed by higher hydrocarbon can be lead to higher rising levels, as it was observed in our study (Fig. 4.3).

Table. 4.4 Simulation results of the Tamoc single bubble model for gas emission site at Mictlan Knoll. For cases 1–3 data from GeoB19336-8 were considered; in case 4, we assume that the gas bubble was composed of pure methane only.

| Case | Bubble equivalent spherical radius | Molecular gas composition (%) | | | Calculated maximum rise height of flare |
|---|---|---|---|---|---|
| | (mm) | methane | ethane | propane | (mbsl) |
| 1 | 1.4 | 99.48 | 0.25 | 0.22 | 2810 |
| 2 | 4.4 | 99.48 | 0.25 | 0.22 | 836 |
| 3 | 2.9 | 99.48 | 0.25 | 0.22 | 1955 |
| 4 | 4.4 | 100* | 0* | 0* | 1162 |

The transport of gas bubbles from a hydrocarbon seep in the water column has been argued to depend on bubble size, gas composition, presence of surfactants (Leifer and MacDonald 2003), initial depth, temperature, ambient water conditions but the relative contributions of each of these factors is not yet fully understood. In order to better constrain the fate of rising gas bubbles released at the seafloor, numerical models have been used to simulate the mechanism of gas bubble transport in the water column (Leifer 2015; Leifer and Patro 2002; McGinnis et al. 2006; Römer et al. 2019; Wang and Socolofsky 2015). By comparing the modeling results with more visual and hydroacoustic observations might advance understanding in both fields.

## 4.6 Conclusions

A comprehensive multibeam echosounder seafloor survey along with systematic hydroacoustic water column investigations in the southern Gulf of Mexico in spring of 2015, led to the discovery of 209 gas emission sites spread across an area of ~19,600 $km^2$ in the Campeche Knolls and Sigsbee Knolls located within the 4S deep-water salt province. The gas emission sites are mainly located at bathymetric elevations (e.g., knolls or ridges), and the origin of oil slicks systematically occur at the sea surface above these structures. Morphological investigations of 40 individual knolls and ridges led to the classification and definition of four common structural types: Chapopote-type knolls, Flat-topped-type knolls, Furrow-type ridges, and Asymmetric-type ridges. The spatial distribution of gas emissions from these structural types appears to be associated with faults, depressions, or slumps, resulting from underlying salt tectonism. Conceptual models for seepage processes are proposed for each of the four structures. Gas emissions from Chapopote-type knolls are systematically located along the rim of a central crater-like depression. These knolls are known to host hydrocarbon accumulations in sediments overlying salt diapirs, which formed a reservoir-seal system for hydrocarbons at their crests. Solid asphalt deposits and gas hydrates are proposed to have created a temporary seal, causing lateral fluid migration so that fluids migrate upward and toward the rim of the crater-like depression. At the Flat-topped type knolls fluid migration pathways in the sub-surface are highly constrained by underlying salt bodies. It is suggested that the flat-topped morphology indicates that salt has spread laterally in the sub-surface, which also limited the vertical migration for hydrocarbons. The gas emission sites are generally distributed around the edges of Flat-topped-type knolls, indicating that the salt-sediment interface could be an effective transport pathway for rising fluids. The gas emission sites of Furrow-type ridges are distributed primarily along the crests or along furrow-like depressions. The morphology of this ridge-type implies that it is influenced by normal faults or more complex fault systems and these faults may provide efficient conduits to allow hydrocarbons to migrate to the seafloor. Gas emission sites of Asymmetric-type knolls were found to be limited to the top of the crests and or the chaotic flank, which is argued to be the result of a thin sediment cover.

At Challenger Knoll, the highest flare on the present record was reported as it was rising 3,100 m through the water column from 3,600 mbsl at the seafloor. The flare heights in our study area suggest that gas bubbles do not reach the sea surface based on our hydroacoustic observations. These results are supported by modeling results, which reveal that the methane contained in hydrate-coated bubbles are completely dissolved in the water column during the rise of the bubbles through the water column.

## 4.7 Acknowledgments

We sincerely appreciate the excellent cooperation from the captain and the crew of R/V METEOR during cruise M114 as well as the professional assistance of the scientific and technical operating teams of the ROV 'MARUM Quest 4000m' and AUV 'MARUM Seal'. We are very grateful to the Mexican authorities for granting permission to collect the multidisciplinary data from Mexican national waters (permission of DGOPA: 02540/14 from 5 November 2014). Our sincere thanks go to Marta Torres (Oregon State University) and Patrizia Geprägs (MARUM) for their contribution on the geochemical data analysis. Additional thanks go to, Jan-Derk Groeneveld, Tiago Biller, Nils Brückner and Stefanie Gaide (both MARUM) for their support on MBES data processing. Cruise M114 was funded by the German Research Foundation (DFG – Deutsche Forschungsgemeinschaft) through the cruise proposal "Hydrocarbons in the southern Gulf of Mexico". Additional funding was provided through the DFG-Research Center/Excellence Cluster "The Ocean in the Earth System". C.-W. Hsu would like to thank the Deutscher Akademischer Austausch Dienst (DAAD) for providing a scholarship (program ID: 57048249). I.R. MacDonald acknowledges support from the Gulf of Mexico Research Initiative ECOGIG 2 consortium for participation in the M114 cruise. We are particularly grateful to Dr. Heiko Sahling for his special contribution and to commemorate his dedication to this research.

# 5. Manuscript II: Hydrocarbon Seepage at Challenger Knoll

## Characteristics and hydrocarbon seepage at the Challenger Knoll in the Sigsbee Basin, Gulf of Mexico

Chieh-Wei Hsu[1], Ian R. MacDonald[2], Miriam Römer[1], Thomas Pape[1], Heiko Sahling[1†], Paul Wintersteller[1], Gerhard Bohrmann[1]

**Published in Geo-Marine Letters**

https://doi.org/10.1007/s00367-019-00595-x

Published online: 10 October 2019

[1]MARUM – Center for Marine Environmental Sciences and Department of Geosciences at the University of Bremen, Klagenfurter Str. 4, 28359 Bremen, Germany

[2]Department of Earth, Ocean and Atmospheric Science, Florida State University, Tallahassee, Florida 32306-4320, USA

[†]Deceased April 23, 2018

*Corresponding author: Chieh-Wei Hsu
phone: +49 (0) 421/218 65055, e-mail: cwhsu@marum.de

Key words: Hydroacoustic, Sigsbee Knolls, Gas emissions, Natural oil slicks, Hydrocarbons, Flares, Remote sensing

## 5.1 Abstract

Active seafloor hydrocarbon seepage from three distinct, positive seafloor features, termed knolls, in the Sigsbee Knolls area, Gulf of Mexico (GoM), was investigated in March 2015. The study sites included the Challenger Knoll, which was drilled by the Deep Sea Drilling Project (DSDP) in 1969 and showed the influence of salt tectonics on its evolution and the presence of subsurface petroleum. This study used gas flare mapping in the water column, detailed seafloor bathymetry, backscatter mapping, sub-bottom profiling, and remote sensing of surface water to locate seafloor areas of hydrocarbon emissions. Flares of gas bubbles were detected in the water column above all three knolls, making them the deepest reported gas emission sites in the GoM. Although surface oil slicks above the Sigsbee Knolls have been detected by satellite imaging in the past; in this study, neither satellite imagery nor ship-based observations detected floating oil;, this suggests that oil seepage in the region is intermittent. High-resolution video surveys of the seafloor at Challenger Knoll, using a camera system mounted on a lowered tow-vehicle, documented the presence of seep-related chemosynthetic fauna including clam fields and microbial mats at the western part of the knoll. These findings are consistent with previous investigations that link hydrocarbon seepage at Challenger Knoll to salt tectonics. During visual seafloor inspections, no asphalt deposits, such as those known from sites in the Campeche Knoll area in the southern GoM, were observed. These findings indicate that hydrocarbon seepage is less pronounced in the Sigsbee Knolls region, central GoM, than is the case in hydrocarbon systems in the northern or southern GoM.

## 5.2 Introduction

The deep-sea regions around Sigsbee Knolls and Campeche Knolls host the largest allochthonous and autochthonous salt units in the central and southern Gulf of Mexico (GoM) (Cruz-Mercado et al. 2011, Fig. 5.1). Both regions are characterized by complex geological structures and active hydrocarbon seepage. Natural oil slicks on the sea surface, detected by satellite imagery, have been reported in previous studies (MacDonald et al. 2015; Williams et al. 2006). The Sigsbee Knolls are sub-circular features in the deep Sigsbee Abyssal Plain (Fig. 5.1) intruding several hundred meters into the water column that were first reported by Ewing et al. 1958. This led to research on their origin and their significance regarding the formation of the GoM basin. Seismic profiles, gravity, and magnetic data collected over three seafloor structures in that area suggested that they were salt domes, potentially associated with petroleum accumulations (Ewing et al. 1962).

During Leg 1 of the Deep Sea Drilling Program (DSDP) in 1969, one of the Sigsbee Knolls, subsequently named Challenger Knoll (Ewing et al. 1969c), became the site of the program's first successful drilling operation. Subsurface lithology determined by that drilling revealed that the cap rock of the salt dome, which was found below 136 m of pelagic sediment; comprised mainly calcite and gypsum (Ewing et al. 1969a). Age estimates of the cap rock suggested that the salt in the Sigsbee Knolls was similar to the Jurassic-aged Louann Salt, which is known from the northern GoM (Ewing et al. 1969c). Petroleum was recovered in Lower Pliocene deposits (> 102 mbsf), which are mainly composed of calcareous biogenic oozes, including highly bioturbated nanoplankton marls with foraminifera. Seismic exploration in the Sigsbee Knolls area indicated that sediments overlying the oceanic crust comprise six seismic units, including Jurassic salt deposits that feed the salt domes and lead to the formation of the

seafloor knolls (Ladd et al. 1976). Contrasting seismic reflection characteristics (Ewing et al. 1962) and DSDP drilling results (Ewing et al. 1969a) suggested that units above the salt were formed by late Mesozoic to early Tertiary pelagic sedimentation, which were followed by mid-Tertiary to Pleistocene deposition of turbidities.

Fig. 5.1: Inset shows a map of southern and central Gulf of Mexico with bathymetry based on shaded

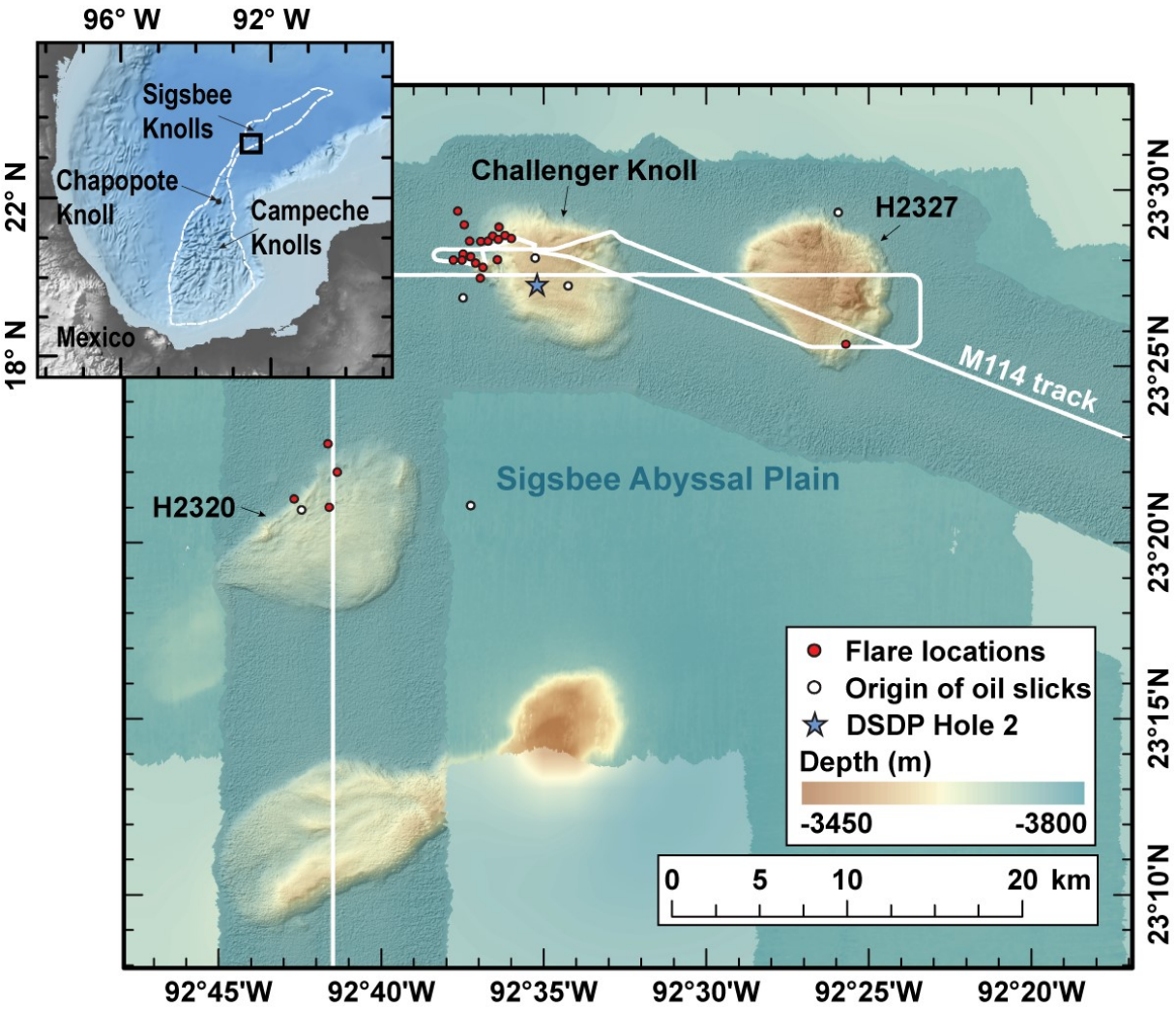


GEBCO (General Bathymetric Chart of the Oceans). The study area is shown with a rectangle. The larger map shows ship-based multibeam echosounder (MBES) bathymetry of the study area with a grid cell size of 30 m, in combination with ship track (white line) and vertical projections of flare locations (red dots) detected during R/V METEOR cruise M114. The origins of sea surface oil slick locations (white dots) are from the dataset reported by MacDonald et al. (2015). DSDP Leg 1, Hole 2, drill site (blue star) is also shown. Knolls H2327 and H2320 were named during the cruise M114 (Sahling et al. 2017) followed the naming system first used by Bohrmann and Schenck (2004) in the GoM.

The first photographic surveys of the deep ocean floor in the southern GoM were carried out in 2003 in the area of the Campeche Knolls (Bohrmann and Schenck 2004), which are diapiric structures with similar evolution to the Sigsbee Knolls in 3000 m water depth. At one such structure, called Chapopote Knoll, lush chemosynthetic communities were discovered among extensive lava-like asphalt deposits on the crest of the knoll (Bohrmann and Schenck 2004; Brüning et al. 2010; MacDonald et al. 2004). A recent study by Sahling et al. (2016) confirmed six additional asphalt deposit sites in the Campeche Knolls area. The aforementioned studies have shown hydrocarbon seepage, including gas bubble emissions, asphalt volcanism, and associated chemosynthetic fauna, to be a widespread phenomenon in the southern GoM (MacDonald et al. 2004; Sahling et al. 2016). Despite the DSDP findings of Jurassic-age salt, cap-rock and hydrocarbons, it was not known whether Sigsbee Knolls hosted gas emission sites and manifestations of asphalt volcanism similar to those in the Campeche Knolls.

In this paper, results from gas flare mapping in the water column, detailed seafloor bathymetry and backscatter mapping, sub-bottom profiling, and remote sensing of the sea surface were combined to investigate seafloor gas emissions at Challenger Knoll and two other knolls (termed H2027 and H2320) in the Sigsbee Knoll area (Fig. 5.2).

## 5.3 Geological setting

The Sigsbee Abyssal Plain, which is the deepest part of the GoM (Fig. 5.1), is delineated by the Sigsbee Escarpment to the north, the Campeche Knolls to the south, the Florida Escarpment to the east, and the Mexican continental shelf to the west. Within the flat Sigsbee abyssal plain, the Sigsbee Knolls are situated in ~3700 meters below seafloor (mbsl). The depositional history of the Sigsbee Knolls can be traced back to Jurassic times during the rifting stage of the GoM, and at least 5 km of sediment has been deposited in the Sigsbee basin in subsequent eras (Ewing et al. 1962). The basin's structural evolution is represented in a series of regional deformation events associated with the movement of salt sequences deposited during the Jurassic age (Angeles-Aquino et al. 1994), contemporaneous with the formation of the Louann Salt on the Texas-Louisiana slope (Salvador 1991a). Based on the results from DSDP drilling (Leg 1, Hole 2; Ewing et al. (1969a)) and the detection of natural oil slicks on the sea surface on satellite synthetic-aperture radar (SAR) images from June 2002 (MacDonald et al. 2015), the Sigsbee Knolls area is considered to be a petroleum-producing salt province in the central GoM.

## 5.4 Materials and Methods

### 5.4.1 Remote sensing

Two Radarsat-2 SAR images were recorded over the central part of the GoM at approximately midnight on 18 March and midday on 19 March 2015 during ascending and descending orbital paths. Weather conditions at the time and in the area of the image acquisitions were ideal for imaging oil floating on the sea surface ('oil slicks') in the GoM (Daneshgar Asl et al. 2017), cause wind speed was low between 2 and 6 m/s, with a swell less than 1 m in height, under skies clear of precipitation.

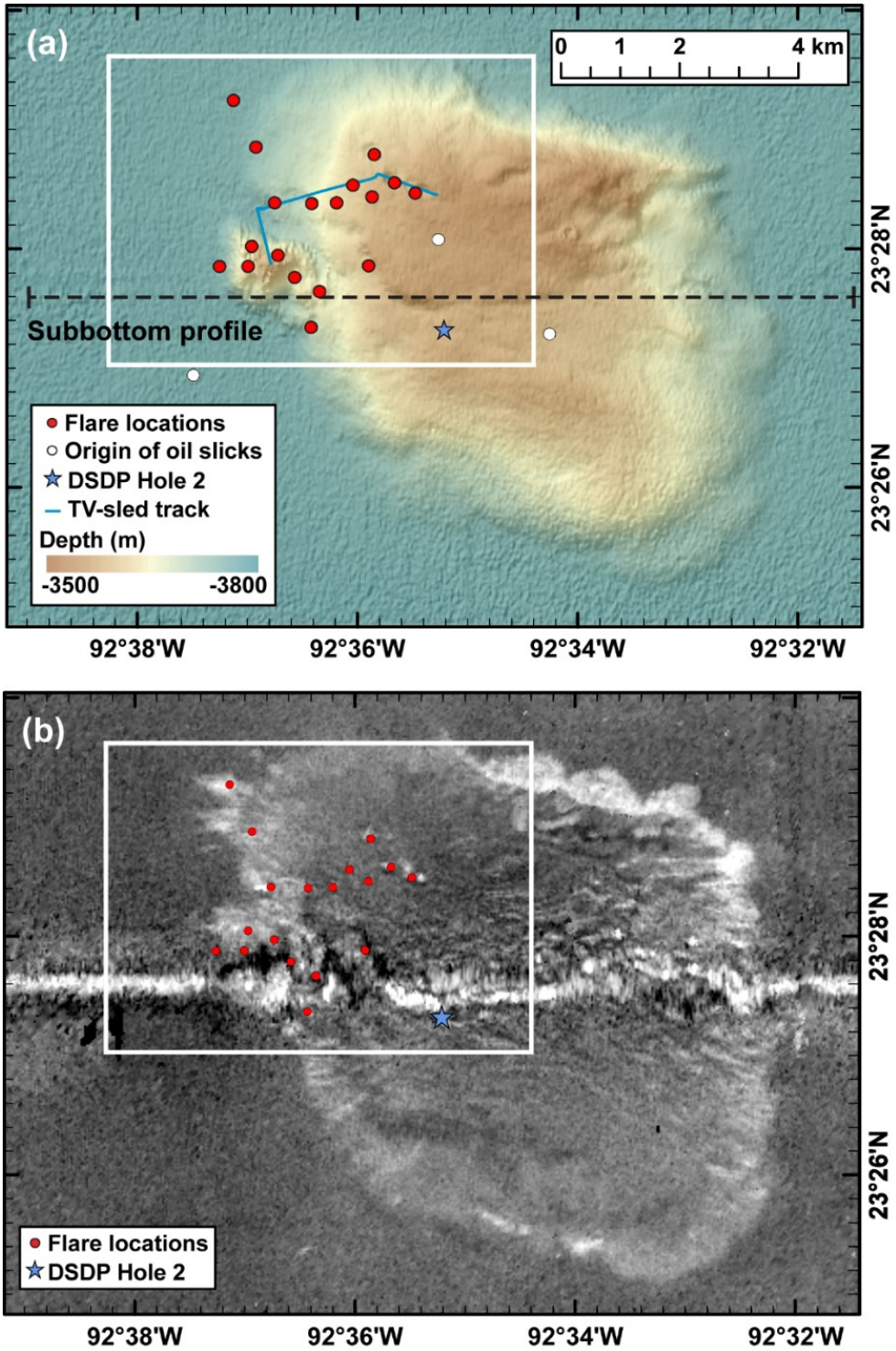


Fig. 5.2: (a) Ship-based MBES bathymetry of the Challenger Knoll and locations of the TV-sled track (blue line), vertical projections of flare locations (red dots), as well as the DSDP drill site (blue star). The origins of the sea surface oil slick locations (white dots) are from the dataset reported by MacDonald et al. (2015). Position and orientation of sub-bottom profile recorded across the center of the knoll (black dotted line), shown in Fig. 5.5. The white rectangle outlines the area with active gas emissions, corresponding to the area of Figs. 5.3a and 5.3b. (b) Side-scan sonar image of the Challenger Knoll along the track shown in (a). High seafloor backscatter reflectance is shown in white. White line across the knoll is an artifact.

### 5.4.2 Research vessel and hydroacoustic data

A hull-mounted, multibeam echosounder (MBES, Kongsberg EM122) was used to map bathymetry, seafloor backscatter, and hydroacoustic anomalies in the water column (termed flares) during R/V METEOR cruise M114 (February-March 2015) (Sahling et al. 2017). This deep-water MBES has a Mills cross configuration with an acoustic footprint of 1° (TX) along-track and 2° (RX) across-track and operates with a nominal sonar frequency of 12 kHz. Best resolution and coverage were acquired using a swath-width of 120° (60° port and starboard, respectively) configured in high-density, equidistant and dual-swath mode (up to 864 soundings per ping). Bathymetry was processed with the open-source software package MB-System (Caress and Cheyes 2017). In addition, seafloor backscatter analyses were conducted with the QPS Fledermaus™ FMGT package for comparison. Hydroacoustic anomalies in the water column caused by rising gas bubbles were evaluated for the detection of flares by visually inspecting each swath within the QPS Fledermaus™ Midwater software. The datasets analyzed for this study can be found in the Open Access library PANGAEA (https://www.pangaea.de/). Access to raw data including water column information: https://doi.org/10.1594/PANGAEA.864652 and gridded bathymetry: https://doi.pangaea.de/10.1594/PANGAEA.900987.

High frequency (3.5-12 kHz) echograms such as sub-bottom profiler are commonly used for high resolution characterization of subsurface sedimentation processes (Damuth 1980; Gaullier and Bellaiche 1998; Loncke et al. 2002). In this study, sub-bottom profiler data were acquired using a hull-mounted Teledyne Atlas Parasound™ P70 system, which utilizes the parametric effect based on the non-linear relation of pressure and density during sound propagation. The system operates with two primary high frequencies (PHF at 18 and 22 kHz) to generate a secondary low frequency (SLF) of 4 kHz, providing a high-resolution image of shallow sedimentary sub-bottom structures. The maximum penetration of the acoustic signal was 100 m sub-bottom with a footprint size of ~ 7% of the water depth. The data were recorded with the software Teledyne Atlas Parastore and processed with the program SeNT (developed by H. Keil, University of Bremen).

### 5.4.3 Seafloor observations

Direct visual inspections of the seafloor at Challenger Knoll were carried out along three tracks of a lowered tow-vehicle (TV-sled survey) that provided a real-time video feed via a camera (OKTOPUS GmbH; Kiel, Germany) and recorded HD video clips via an AquaPix™ video time-lapse camera (VTLC, Johansen et al. 2017). The sled was towed at a speed of about 0.2-0.5 knots at the seafloor. VTLC video was reviewed when the TV-sled was recovered to the ship.

## 5.5 Results

### 5.5.1 Seafloor morphology and backscatter

Challenger Knoll is a distinct feature in the Sigsbee Knolls, which is located in the central abyss of the GoM. Swath mapping conducted in the present study showed that it is sub-circular, approximately 10 km in diameter, and rises approximately 200 m above the surrounding seafloor (Fig. 5.2a). High backscatter reflectance around the knoll is generally most pronounced on the northeastern and western margins of the feature (Fig. 5.2b). Four funnel-

shaped depressions, about 200 to 300 m wide and tens of meters in depth, occur on the northwestern part of the knoll (Fig. 5.3a) and are characterized by relatively high seafloor backscatter as well (Fig. 5.3b). Adjacent to the main knoll structure, along the western edge of the knoll, the survey revealed a cone-shaped feature about 170 m in height and 1.5 km in diameter (Fig. 5.3a).

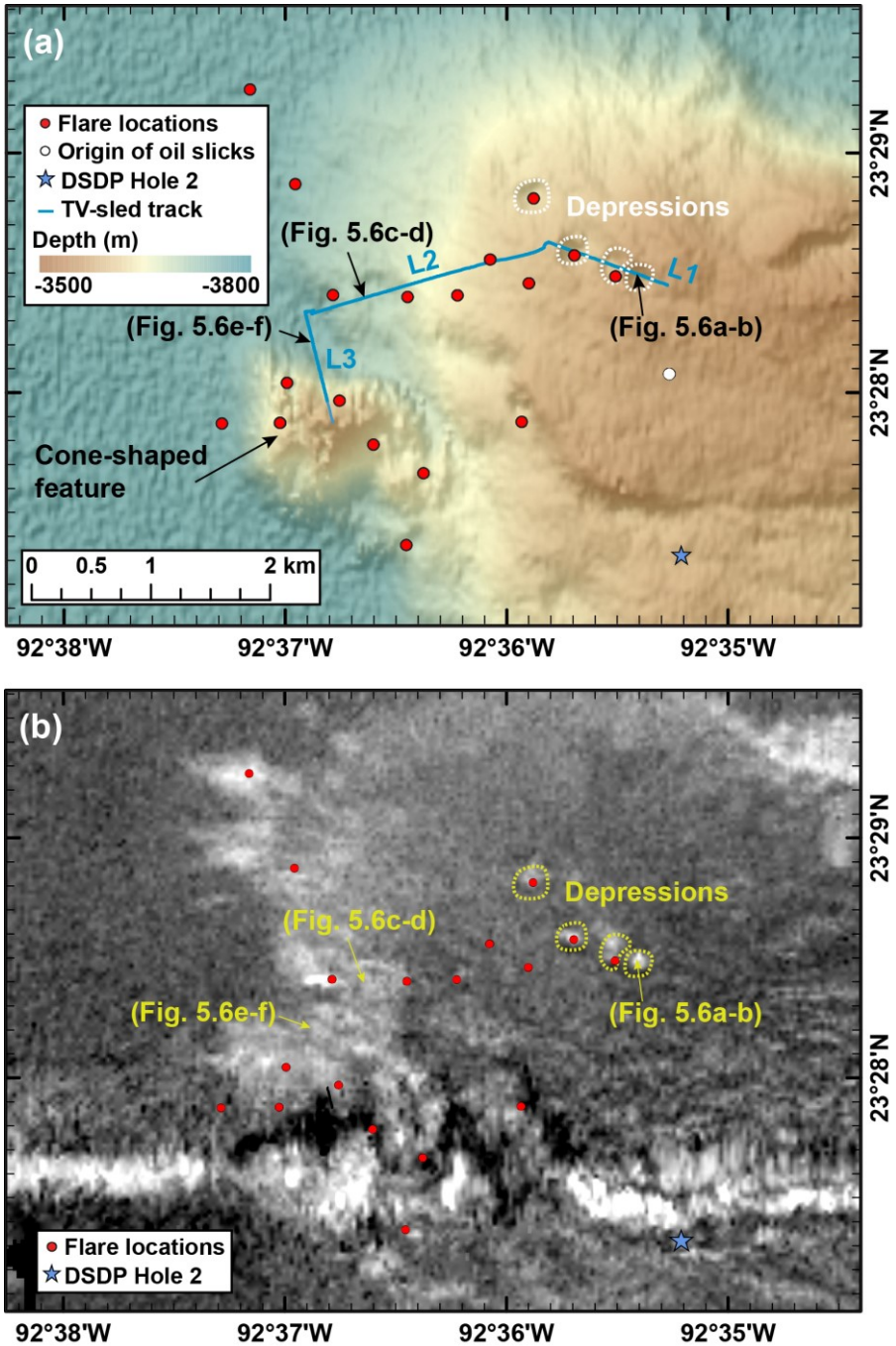


Fig. 5.3: (a) Bathymetry of active gas emission area (white rectangle of Fig. 5.2a) showing TV-sled survey lines (L1, L2, and L3). The locations of seafloor images from Fig. 5.6 are indicated by black arrows. (b) Zoomed backscatter map of active gas emission area (area of white rectangle of Fig. 5.2b). High seafloor backscatter reflectance shown in white.

### 5.5.2 Seepage activity

Hydroacoustic profiling of the water column covering the entire Challenger Knoll, knolls H2327 and H2320, revealed the occurrence of 23 flares, which are attributed to seafloor gas emissions (Fig. 5.1). A total of 18 flares was found concentrated in the northwestern area of the Challenger Knoll (Figs. 5.2a and 5.3a). Four flares were observed at the northwestern edge of knoll H2320 and a single flare was detected at the southern edge of H2327. Figure 5.4 shows that the deepest parts of the flares were recognized at ~2600 m water depth and that they disappeared from the echograms at ~500 m water depth. The projected gas emission sites were located at patches of high seafloor backscatter within seafloor depressions and around the cone-shaped feature NW of the main Knoll (Figs. 5.3a and 5.3b).

Remote sensing data a previous study (MacDonald et al. 2015) reported that sea surface oil slicks near Challenger Knoll were detected in 2002. However, two SAR images, which were collected during the M114 cruise, did not detect floating oil despite favorable weather conditions.

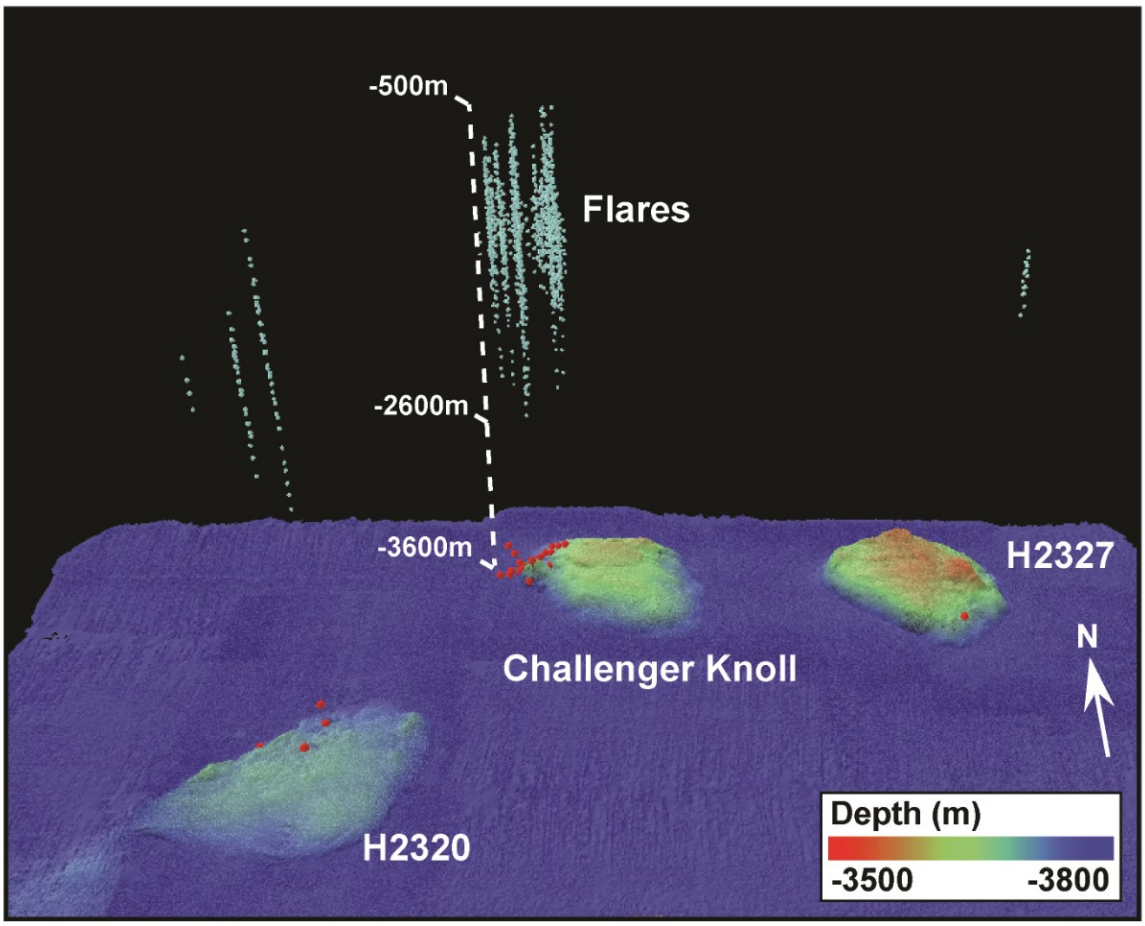


Fig. 5.4: Perspective view of the flares detected in the water column and the approximate, projected gas emission sites at the seafloor (red dots) of three Sigsbee knolls investigated. At Challenger Knoll, bubbles are acoustically visible from 2600 mbsl to ~500 mbsl in the water column.

### 5.5.3 Sub-bottom character of Challenger Knoll

A W-E sub-bottom echosounder profile of the knoll crosses near the location of DSDP Hole 2 and demonstrate the anomalous character of Challenger Knoll compared to the surrounding abyssal sediments (Fig. 5.5). The profile showed regular stratified hydroacoustic reflectors in surrounding sediments, extending to about 100 mbsf. These reflectors terminate abruptly where they onlap the edges of the main knoll structure and the cone-shaped feature in the west. Acoustic returns from the main knoll structure and the cone-shaped feature were mostly chaotic and indistinct. Weak, discontinuous reflectors to about 30 mbsf were found to be restricted to the eastern crest and flank of the main knoll structure. At the cone-shaped feature and on the western flank of the main knoll structure ('Projected flare area' in Fig. 5.5), a few high-amplitude reflectors were detected at shallow depths (less than 10 mbsf). This section of the profile corresponded to the area where flares were detected. Results from DSDP Hole 2 indicate that caprock and petroleum occur in this section of the knoll (Fig. 5.5). At the top of the knoll, high-amplitude reflectors occur at the shallow subsurface followed by an obscured reflector down to 30 mbsf. On the eastern flank, shallow subsurface high-amplitude reflectors are observed at the upper slope as well as at the foot. No further acoustic characters could be distinguished.

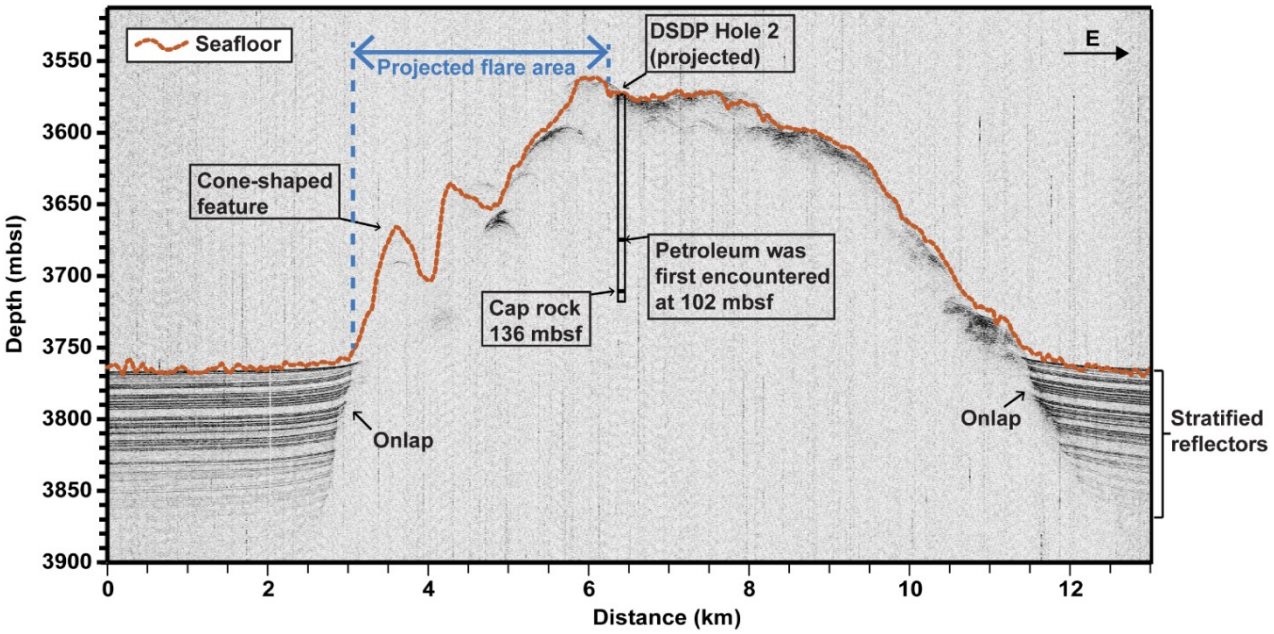


Fig. 5.5: W-E trending sub-bottom profile across the center of the Challenger Knoll along the track shown in Fig. 2a. Flare area and DSDP drill site are projected into this profile (see Fig. 5.2a for flare and DSDP site locations). Sub-paralleled reflectors onlap onto the knoll at the transitions between the flat abyssal seafloor and Challenger Knoll.

### 5.5.4 Visual seafloor observations

Visual seafloor observations were conducted during TV-sled survey GeoB19355-1 in the northwestern portion of Challenger Knoll, where gas flares and high seafloor backscatter patches were detected (blue lines in Figs. 5.2a and 5.3a). Three interlinked transect lines were completed across this target area (Fig. 5.3a). Observed indicators of seepage were carbonate-like rubble and galatheid crabs (Fig. 5.6a), dark patches of sediment (Fig. 5.6b), white microbial mats (Figs. 5.6c and 5.6d), and clams putatively of the genus *Calyptogena* (Figs 5.6d and 5.6f). The latter were seen as scattered shells and apparently living individuals that plowed short trails through the surface layer (Figs. 5.6e and 5.6f). Line L1 started from the northwestern part of the knoll and headed northwestward. Figure 5.6b shows a cluster of approximately 10-20 clams inside a dark patch in one of the depressions characterized by high seafloor backscatter (Fig. 5.3b). Because the TV-sled survey covered only a part of the region of high backscatter, its total size could not be determined, but further seepage indicators might be present in this area. The TV-sled was moved southwestward (L2) from the top of the knoll to its foot of the knoll (Fig. 5.3a). Extensive whitish microbial mats and carbonates were encountered with abundant clamshells scattered among the microbial mats (Figs. 5.6c and 5.6d). The TV-sled survey was concluded on a southward course (L3) that covered the northern flank of the cone-shaped feature. There, large fields of clam shell were found at the basin (Fig. 5.3a). Clam trails, indicating movements of living clams, were frequently observed in these areas (Figs. 5.6e and 5.6f).

## 5.6 Discussion

### 5.6.1 Gas emissions at Challenger Knoll

The general morphology (Fig. 5.1) of Challenger Knoll is similar to that of numerous other domes in the GoM, which are typically sub-circular and extend 100-300 m above the surrounding seafloor (BOEM 2018; Weber et al. 2014). Formation of these dome structures is believed to be caused by the diapiric upward movement of salt (Hudec and Jackson 2007; Jackson and Talbot 1986) with variations in shape affected by local and regional deformation (Cruz-Mercado et al. 2011; Sánchez-Rivera et al. 2011). The bathymetric and sub-bottom profile across Challenger Knoll (Fig. 5.5) illustrates a domed seafloor structure, with well-defined, steep flanks (slope angle up to 20° at the western flank; 5° at the eastern flank). The lack of sub-parallel reflectors together with the presence of weak, irregular reflectors on the crest of the knoll suggest that the subsurface sediments are disturbed and chaotic compared with the surrounding seafloor. In general, free gas or fluids can cause blanking of acoustic reflectors in the sub-bottom profile (Judd and Hovland 1992; Tóth et al. 2015). The limited sub-bottom penetration depth (less than 10 m) in the projected flare area on the western flank (Fig. 5.5) might be due to the scattering of acoustic waves at the steep slope.

Many gas emission sites at Challenger Knoll, H2320 and H2327 were observed near the edges of the knolls. This observation is consistent with findings of Weber et al. (2014) in the northern GoM, suggesting that the pathways for fluid migration toward the seafloor could be provided by faults, which generally formed in the shallow sediments above the outer edges of diapirs (Hood et al. 2002). It is noteworthy that all active gas emission sites detected at Challenger Knoll during the time of this investigation were located on the western side (Fig. 5.2). This

might reflect the discontinuous development of migration pathways for the release of gas and fluids.

The bathymetric map of Challenger Knoll (Figs. 5.2a and 5.3a) illustrated small-scale morphological features on the knoll. These include depressions located in the northwestern area of the knoll ranging in size from tens to a few hundred meters (Fig. 5.3a). The seafloor backscatter map (Figs. 5.2b and 5.3b) further shows that high backscatter mainly occurred around the edges of the knoll and within the depressions. Visual seafloor observations also showed that darker patches, microbial mats, galatheid crabs, and clams (Fig. 5.6) may be restricted to the high seafloor backscatter areas close to the gas emission areas; however, further survey data would be needed to confirm this observation. The darker patches are likely underlain by cementation of seep carbonates that generates a hard substrate and might also contribute to high seafloor backscatter (Buerk et al. 2010; Gay et al. 2007). Previous studies have shown that presence of gas within sediments can be significant in transforming seafloor morphology (Koch et al. 2015; Naudts et al. 2006; Sahling et al. 2008b; Sultan et al. 2014). Figures 5.3a and 5.3b show that some gas emission sites were located at the depressions with high backscatter signatures. Therefore, the formation of these depressions may be related to hydrocarbon seepage.

Flare mapping (Fig. 5.4) showed that seafloor gas bubble emissions into the water column occurred at Challenger Knoll, H2327, and H2320 during the time of this study. The respective flares were visible in the water column from ~ 2600 mbsl to ~500 mbsl. The lack of flare detection deeper than 2600 m might be due to methodological limitations related to the relation of the resonance frequency of the gas bubbles with different sizes and the frequency of the echosounders (Medwin 1970; Weber et al. 2014). Gas bubbles causing these flares must originate from the seafloor in ~ 3600 m, which represent the deepest gas emission sites known in the GoM so far. Although gas bubble streams from the seafloor were not detected during the TV-sled survey, this was most probably due to methodological restrictions with images obtained in plain view and the limited seafloor coverage. In general, the presence of putative chemosynthetic clams (Figs. 5.6e and 5.6f) indicates that dissolved methane was present in shallow sediments in amounts sufficient to sustain chemosynthetic life. Because the visual seafloor survey did not fully cover the area where flares were observed, it is probable that further surveys would detect gas bubble emission sites and additional seep-related communities.

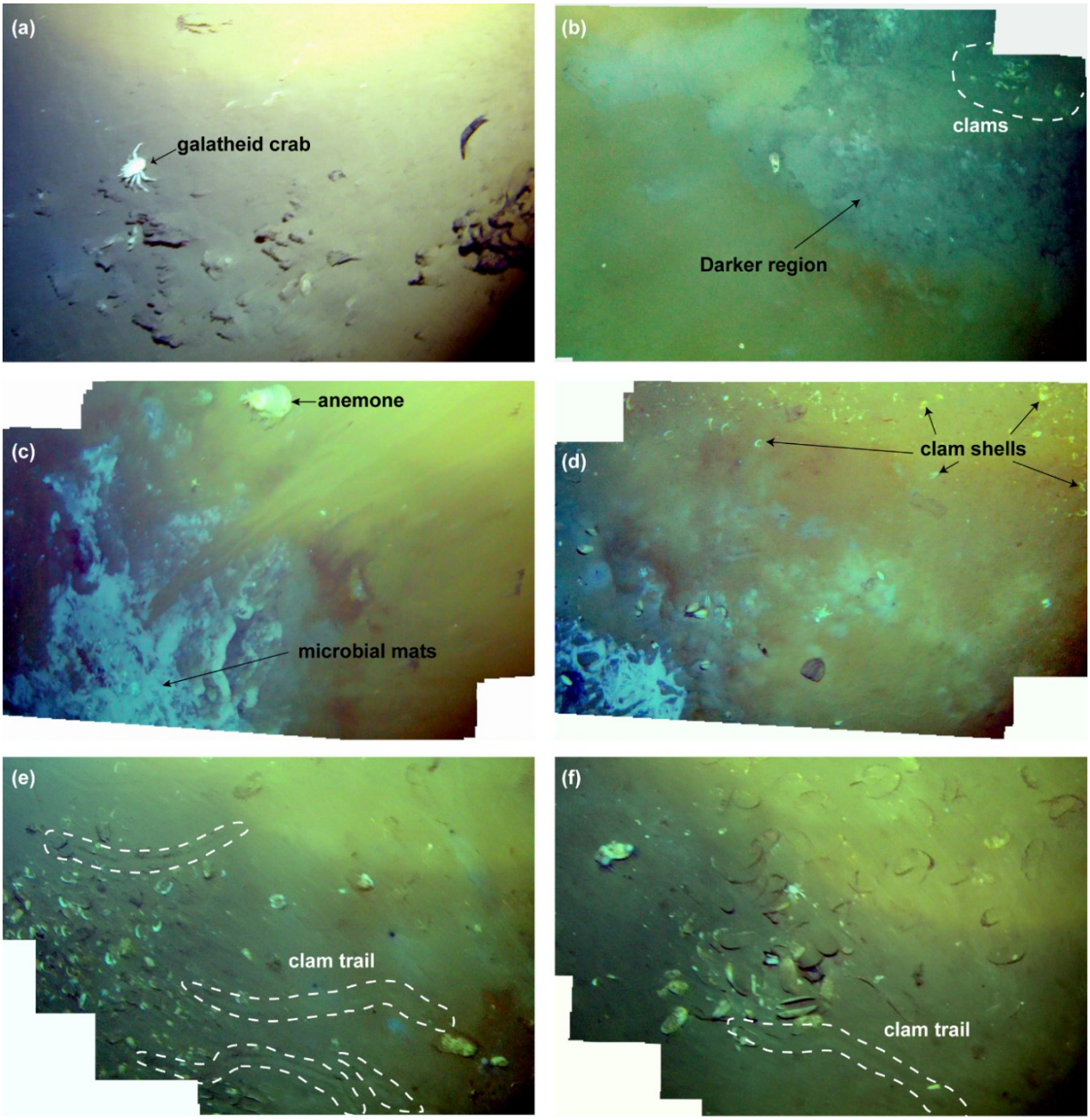


Fig. 5.6: Seafloor panorama images captured from time-lapse camera videos at Challenger Knoll along TV-sled survey lines: L1 (a, b), L2 (c, d) and L3 (e, f), for line locations see Fig. 5.3a. (a) A galatheid crab (arrow) on the carbonate-like rubble surrounded seafloor. (b) Clams (outlined in white, upper right edge) within a darker region likely underlain by authigenic carbonate. (c) An extensive whitish layer at seafloor interpreted to be microbial mats. (d) Clams are living in association with microbial mats appearing in the lower region, abundant clam shells are shown in the upper part of the image. (e) Field of clam shells and clam trails made by the movement of living clams. (f) Half-buried clam shells and a clam trail.

### 5.6.2 Hydrocarbon seepage difference between Sigsbee Knolls and Campeche Knolls

Based on the interpretation of geophysical data from previous studies in the southern and central GoM (Cruz-Mercado et al. 2011; Ewing et al. 1962; Ladd et al. 1976), Campeche Knolls and Sigsbee Knolls were believed to have developed from the same origin and are thought to have similar sedimentation histories. In both regions, salt tectonism led to main deformation events and was the primary topographic control (Bird et al. 2005; Cruz-Mercado et al. 2011; Garrison and Martin 1973; Worzel et al. 1968). As a result, both regions host extensive salt domes, are potentially associated with petroleum accumulation, and showed gas migration as well as seafloor discharge (e.g., Brüning et al. 2010; Ewing et al. 1962; Sahling et al. 2016; this study). Although it remains under-explored compared to the northern GoM, the southern Gulf has been known as a region with significant and widespread natural hydrocarbon seepage (MacDonald et al. 2015; Williams et al. 2006). Investigation of oil seepage and asphalt volcanism at the Chapopote Knoll showed that the region hosts seeps and chemosynthetic communities at greater water depths (Brüning et al. 2010; Ding et al. 2008; Ding et al. 2010; MacDonald et al. 2004; Marcon et al. 2018; Sahling et al. 2016; Schubotz et al. 2011b) Recently, Sahling et al. (2016) showed a variety of emission types that actively release hydrocarbons at the Campeche Knolls including gas bubble emissions, oil seepages, and asphalt extrusions, all of them supporting abundant chemosynthetic communities. However, fluid seepages confirmed by this study at the Sigsbee Knolls were limited to gas bubble emissions, while oil seepage and asphalt flows were not found.

In past studies, remote sensing of sea surface oil slicks in the southern GoM was successfully applied to locate active seafloor hydrocarbon seepage areas, like the Chapopote asphalt volcano (MacDonald et al. 2004), and numerous additional knolls and ridges in the Campeche Knolls area (Sahling et al. 2017; Sahling et al. 2016) and oil seeps in the southeastern Black Sea (Körber et al. 2014). Satellite evidence for the presence of oil slicks has been reported above all three knolls in the past (MacDonald et al. 2015) that were also surveyed in this study (Fig. 5.1).

Although the exact seafloor location of oil source(s) cannot be determined from these images, and oil slicks might have migrated, DSDP drilling demonstrated the presence of oil and gas within sediments at the top of the cap rock of Challenger Knoll (Ewing et al. 1969a), so oil generation in subsurface may be likely at the other diapirs as well. However, during the time of this study SAR images did not reveal the presence of significant sea surface oil slicks above any of the three knolls investigated. Moreover, no floating oil was seen on the sea surface and no indications for oil seepage were found during visual seafloor surveys. The presence of flares indicated that active hydrocarbon migration and gas emission were ongoing in spring 2015. However, the concurrent virtual absence of oil slicks suggested that oil discharge into the water above the Sigsbee Knolls would have to be an intermittent process.

## 5.7 Conclusions

The discovery and exploration of Challenger Knoll in 1969 illustrated the role of salt tectonism in the formation of the Sigsbee Knolls and demonstrated that source rock, migration, and capping structures could host petroleum reservoirs in the deep sea. The present study updates existing data in the region with modern instruments and techniques. Hydroacoustic flare

mapping showed that gas seepage occurred at the Sigsbee Knolls and documented the deepest gas emission areas of 3600 mbsl observed thus far known from the GoM. Seafloor locations around gas emission sites are characterized by high backscatter reflectance, microbial mats, and clams. The distribution of gas emission sites at Challenger Knoll is consistent with previous interpretation established for knolls in the Northern GoM that faults near the edges of salt diapirs provide effective fluid migration pathways.

Although the Sigsbee Knolls in the central GoM and Campeche Knolls in the southern GoM have a similar geologic history, distinct differences between these areas were found in the present study. The Campeche Knolls are characterized by various hydrocarbon seepage types including seafloor asphalt flows and oil discharge (Sahling et al. 2016). In contrast, only gas emissions were observed in the Sigsbee Knolls. This may indicate different types of hydrocarbon reservoirs in the Sigsbee Knoll area. Failure to detect surface oil slicks using satellite SAR in an area where they had previously been documented (MacDonald et al. 2004; MacDonald et al. 2015), and where petroleum migration had been confirmed, demonstrates oil discharges sufficient to form surface slicks can be an intermittent process in abyssal settings.

## 5.8 Acknowledgements

We sincerely appreciate the excellent cooperation from the captain and the crew of R/V Meteor during cruise M114. We are very grateful to the Mexican authorities for granting permission to collect the multidisciplinary data from Mexican national waters (permission of DGOPA: 02540/14 from 5 November 2014). Our sincere thanks go to, Jan-Derk Groeneveld, Tiago Biller, Nils Brückner and Stefanie Gaide (both MARUM) for their support on MBES data processing. We would like to thank the editor Dr. Gabriele Uenzelmann-Neben and two anonymous reviewers for their efforts and constructive comments that helped to significantly improve this manuscript. Cruise M114 was funded by the German Research Foundation (DFG – Deutsche Forschungsgemeinschaft) through the cruise proposal “Hydrocarbons in the southern Gulf of Mexico“. Additional funding was provided through the DFG-Research Center/Excellence Cluster “The Ocean in the Earth System”. C.-W. Hsu would like to thank the Deutscher Akademischer Austausch Dienst (DAAD) for providing a scholarship (program ID: 57048249). I.R. MacDonald acknowledges support from the Gulf of Mexico Research Initiative ECOGIG 2 consortium for participation in the M114 cruise.

# 6. Manuscript III: Extensive asphalt deposits at Mictlan Knoll

## Diversified hydrocarbon seepage at Mictlan asphalt volcano, southern Gulf of Mexico

Chieh-Wei Hsu*[,1], Yann Marcon[1], Miriam Römer[1], Paul Wintersteller[1], Thomas Pape[1], Ian MacDonlad[2], Markus Loher[1], Christian Ferreira[1], Gerhard Bohrmann[1]

**In preparation for submission**

[1]MARUM – Center for Marine Environmental Sciences and Department of Geosciences at the University of Bremen, Klagenfurter Str. 4, 28359 Bremen, Germany

[2]Department of Earth, Ocean and Atmospheric Science, Florida State University, Tallahassee, Florida 32306-4320, USA

*Corresponding author: Chieh-Wei Hsu
phone: +49 (0) 421/218 65055, e-mail: cwhsu@marum.de

Key words: Asphalt volcanism, hydroacoustics, hydrocarbon seepage, Campeche Knoll, methane flux

## 6.1 Abstract

Seepage of hydrocarbon gas and oil as well as asphalt deposits were investigated at Mictlan Knoll in the southern Gulf of Mexico (GoM). Recently, there has been an increasing interest in the investigation of submarine asphalt deposits, since asphalt volcanism was first introduced at Chapopote Knoll in 2004. Mictlan Knoll is considered to be an analog of Chapopote Knoll and is one of the sites which host the most active hydrocarbon system in the southern GoM. We used a multi-disciplinary approach including hydroacoustic surveys of the seafloor and water column and ROV-based visual observations to study the distribution and the seafloor manifestations of hydrocarbon seepage at Mictlan Knoll. Mictlan Knoll is characterized by a crater-like depression largely surrounded by an elevated rim feature. Numerous fresh asphalt deposits and oil seepages were found locally in the area extensive asphalt deposits area, in contrast to the findings of one main conduit of fresh asphalt flow in the Chapopote Knoll. Twenty-five flares indicative for gas bubble emission sites were detected, mostly on the rim. A gas bubble stream above a gas hydrate outcrop was quantified to release about 0.09 $x10^6$ mol $CH_4$/yr. The gas emission activity at this site was monitored by an autonomous scanning sonar device, indicating the activity is highly variable. The asphalt deposits were widely distributed in the depression. The relatively bumpy seafloor morphology in the northern depression suggested that an outflow of fresh asphalt below older surficial deposits may occur in this area. A large area of extensive asphalt deposits was correlated with a high backscatter area (~75,000 $m^2$) at the northeastern part of the depression. Our findings suggest that the Mictlan Knoll may host the most extensive asphalt deposits known so far in the GoM.

## 6.2 Introduction

Hydrocarbon seepages play an essential role in increasing habitat heterogeneity and alteration of seafloor morphology in the deep sea (Cordes et al. 2010; Sahling et al. 2008a). In addition to gas and oil seepage, submarine asphalt deposits, a distinct type of nature hydrocarbon seepage has been attracting considerable interest, since it was discovered at Chapopote Knoll in the southern GoM in 2003 during the R/V SONNE cruise SO 174. (Bohrmann and Schenck 2004). Consequently, the asphalt volcanism was introduced by MacDonald et al. (2004) due to the massive lava-like solidified asphalt deposits over the crater-like central depression of Chapopote Knoll. Recent visual seafloor observation conducted with optical mosaicking technique documented several asphalt flow units, illustrating distinct eruption phases of intensified asphalt flows at Chapopote Knoll (Marcon et al. 2018).

Besides Chapopote Knoll, asphalt deposits were observed at 10 further locations in the Campeche Knolls over the past two decades, based on visual seafloor observations (Bohrmann and Schenck 2004; Bohrmann et al. 2008; Sahling et al. 2017; Sahling et al. 2016). In the northern GoM, asphalt deposits at the seabed were discovered at two commercial hydrocarbon appraisal areas, at Puma (Weiland et al. 2008) and at Shenzi (Williamson et al. 2008). Worldwide, asphalt deposits have been reported from an increasing number of locations, including in the northern GoM, seven extinct asphalt volcanoes in the Santa Babara Basin (Valentine et al. 2010), more than 2000 asphalt mounds at the Angolan Margin, in the southern Congo fan (Jones et al. 2014) and in depths of 2652–2752 m, on the North São Paulo Plateau, off Brazil (Fujikura et al. 2017). Asphalt deposits in the GoM and Angolan Margin are associated with salt diapirism and in the Santa Barbara Basin and on the North São Paulo

Plateau are related to the compressional tectonics. These dynamic geological processes allow the migration of asphalt, oil and gas through the sediment to the seafloor and into water column (Ding et al. 2008; Fujikura et al. 2017; Jones et al. 2014; Keller et al. 2007; Valentine et al. 2010; Vernon and Slater 1963; Weiland et al. 2008; Williamson et al. 2008).

The asphalt deposits result from the extrusion of very heavy oil, which are then subject subsequent alteration due to loose volatile compounds, biodegradation, oxidation, which ultimately formed the fragmentation of the asphalt deposits (Brüning et al. 2010; Schubotz et al. 2011b). Asphalt deposits provide important habitats for dense and diverse communities of chemosynthetic fauna, particularly tubeworms and mussels (Jones et al. 2014; Sahling et al. 2016; Weiland et al. 2008). Microbiological investigations on symbionts of chemosynthetic animals from Chapopote expanded the limited range of substrates known to power chemosynthetic symbioses (Rubin-Blum et al. 2017).

The Campeche-Sigsbee salt province is located in the southern GoM (Fig. 6.1), comprising a hummocky seafloor morphology associated with the salt tectonism (Sánchez-Rivera et al. 2011). Its tectonic evolution corresponds to the regional deformation events affecting the sequences of salt deposition during the Jurassic age (Angeles-Aquino et al. 1994; Cruz-Mercado et al. 2011). This area is further characterized by the wide distribution of active hydrocarbon seepage, which originated from the abundant source rock deposition during the Late Jurassic time (Magoon et al. 2001). Widespread oil slicks at the sea surface have been reported from the satellite imagery (MacDonald et al. 2015; Suresh 2015; Williams et al. 2006). More than 200 flares indicative for gas bubble emissions in the water column has been detected during the R/V METEOR cruise M114 (Sahling et al. 2017). The spatial distribution of fluid release at the seafloor is suggested to be controlled by the shallow sediment deformation styles associated with the salt activity (Ding et al. 2010; Hsu et al. 2019).

This study sets out to investigate the diversified hydrocarbon seepage at the Mictlan Knoll in the Campeche-Sigsbee salt province. It describes the extent and the seafloor manifestations of the asphalt deposits and oil seepage using hydroacoustic datasets and optical seafloor surveys. The current active hydrocarbon seepage sites like fresh asphalt deposits, oil seepage and gas seepage are investigated. The distributions of different phases of hydrocarbon seepage give new insights into the mechanism of the subsurface hydrocarbon migration at the Mictlan Knoll and help to better understand asphalt seepage in the southern GOM.

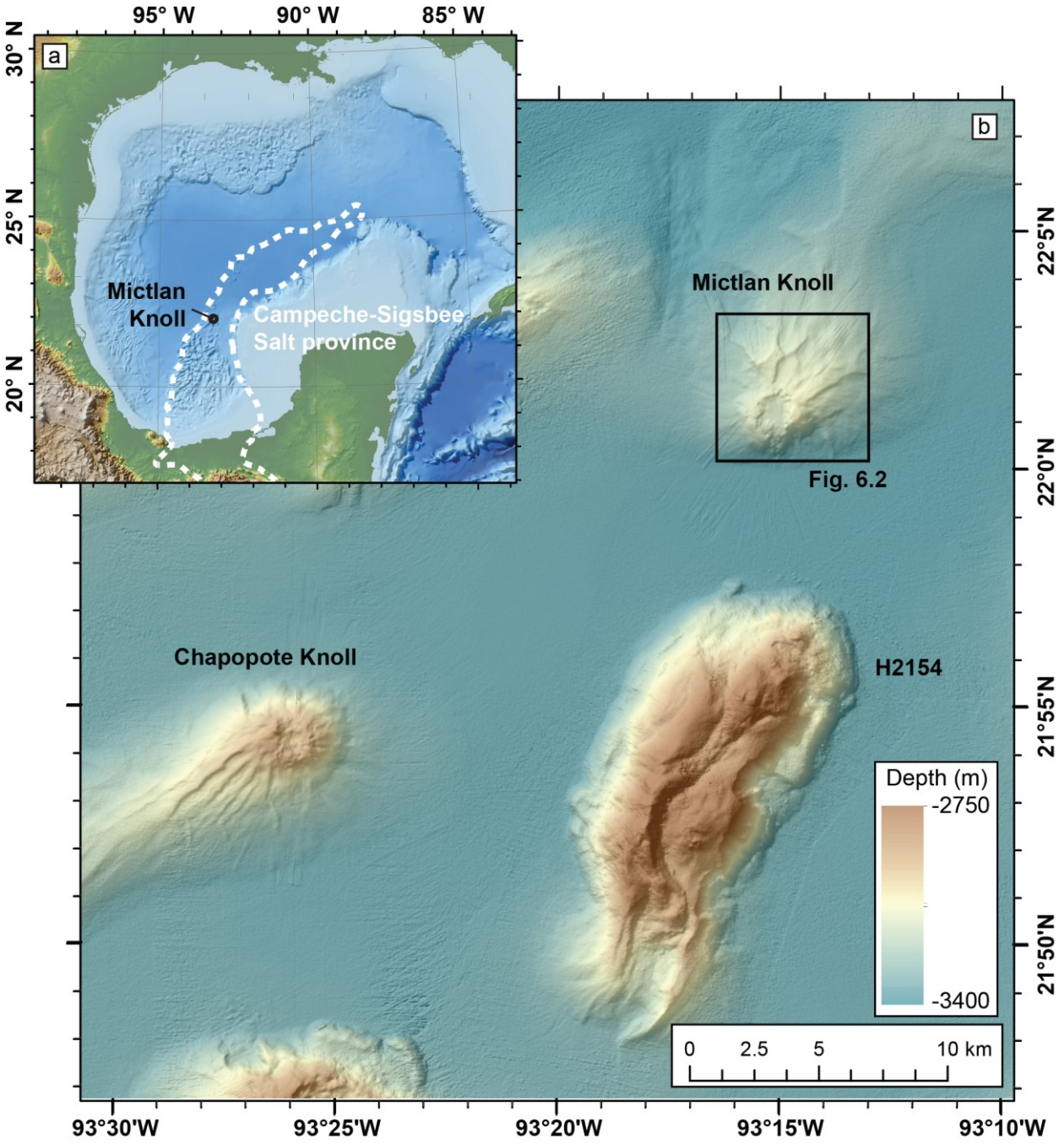


Fig. 6.1 Inset shows a map of Gulf of Mexico with bathymetry based on shaded GEBCO (General Bathymetric Chart of the Oceans). The study site, Mictlan Knoll, is located in the Campeche-Sigsbee salt province (dash white line) in the southern GoM. The larger map shows ship-based multibeam echosounder (MBES) bathymetry of central part of the Campeche-Sigsbee salt province with a grid cell size of 25 m obtained from R/V Meteor cruise M114. Mictlan Knoll is located ~20 km northeast off Chapopote Knoll and ~5 km north off the Knoll H2154.

## 6.3 Methods

### 6.3.1 Hydroacoustic mapping

Data and samples presented in this study were collected during R/V METEOR cruise M114, legs 1 and 2, in spring 2015 (Sahling et al. 2017). Bathymetry, backscatter and water column data were collected with the ship-based multibeam echosounder (MBES) Kongsberg EM122 (12 KHz) system as well as with a Kongsberg MBES EM2040 (300 KHz) system mounted on the autonomous underwater vehicle (AUV) MARUM-SEAL 5000. The bathymetry data were processed with the open-source package MB-System (Caress and Cheyes 2017). The AUV underwater navigation relied on the shipboard IXSEA Posidonia™ ultra short base line (USBL) positioning system and the data was processed with the MB-System navadjust tool. The AUV map demanded a final re-rectification concerning its absolute geo-referencing position. The ArcGIS™ internal georeferencing tools were utilized for this purpose. The MBES backscatter mosaic is a result of processing with the QPS Fledermaus™ FMGT package. Ship-based data was gridded to 25 meter resolution and AUV-based data to 1 meter resolution.

Water column data collected by ship-based and AUV-derived MBES system were conducted with the QPSFledermaus™ FM-Midwater software. The escape of gas from the seafloor causes high backscatter hydroacoustic anomalies in the water column echogram, which are known as ‘acoustic flares’ (Greinert et al. 2006; Naudts et al. 2006). The flare mapping was conducted to locate the gas emission sites in the study area using the AUV-derived data in order to maximize the accuracy.

### 6.3.2 Seafloor exploration

Optical surveys were conducted both with the deep-water remotely operated vehicle (ROV) MARUM Quest 4000 m and the MARUM TV-sled in order to provide ground truth visual seafloor observations of the Mictlan Knoll during M114.

ROV footage was recorded with a forward facing video camera INSITE PACIFIC ZEUS 3CCD HDTV, with 2.2 mega-pixel resolution at 59.94 Hz interlaced. Still images for the photomosaics were acquired with a downward-looking Prosilica GT 6600 camera. It is a full frame photo camera with 29 mega-pixel resolution and a 35mm CCD (12 bit per color) sensor. Image processing and mosaicking were conducted with the LAPM Tool (Marcon 2014; Marcon et al. 2013) using automatic and manual feature detection and matching. Mosaics images are geo-referenced and in the Geotiff format.

In addition, long-distant transect mapping of the Mictlan knoll was performed using a towed TV-sled, equipped with a OKTOPUS (SN 002) video-telemetry of and an Aquapix video time-lapse camera (VTLC). The sled was towed at a speed of about 0.2 - 0.5 knots near the seafloor. A rope with a 15 cm wide shackle was suspended 180 cm below the camera, helping the winch operator to adjust the distance of the sled to the seafloor.

All ROV USBL data were processed (filtering, smoothing, interpolation) using the NavCleaner programs by Marcon (2019). However, due to the failure of the USBL system during the TV-sled surveys, the locations of TV-sled observations were approximated based on ship position.

### 6.3.3 Gas samples

Samples of gas release from the seafloor were collected by the ROV with the gas bubble sampler (GBS) (Sahling et al. 2017). Measurements of gas bubble sizes were conducted with ImageJ (Rasband, W.S., ImageJ, U. S. National Institutes of Health, Bethesda, Maryland, USA, http://imagej.nih.gov/ij/, 1997-2014). The software was used to analyse the video sequences frame by frame. A funnel with a 16.2 cm open mouth was attached to the gas bubble sampler (GBS) and served as a reference for size and focal plane when measuring the bubbles. Only those bubbles rising at the same focal plane as a known size object were analyzed. The major $(a)$ and minor bubble axes $(b)$ were measured and the volume was calculated according to the assumption of a rotational ellipsoid with the equivalent spherical radius $(r_e)$ (Leifer and Patro 2002) (Eq. 6.1). The collected gas bubbles by the GBS were measured for their molecular composition according to the method by Pape et al. (2010).

$$r_e = (a^2 b)^{-3} \qquad \text{(Eq. 6.1)}$$

The calculated gas flux (in mL $min^{-1}$) is based on the average bubble volumes and the numbers of bubbles rising through the water column during the observation time. The volume flux was converted to mass flux (in mol $CH_4$ $min^{-1}$) based on the molecular composition of the gas considering the methane compressibility according to Römer et al. (2012b).

### 6.3.4 Temporal monitoring of bubble plumes

Time series of the gas emission activity at the seafloor was recorded by the autonomous scanning sonar module (ASSMO), which was first deployed on MARIA S. MERIAN cruise MSM15/2 (Bohrmann et al. 2011). The ASSMO is equipped with an IMAGENEX 881A scanning sonar located about 180 cm high above the seafloor in order to minimize bottom reflection. The instrument has a pressure housing, attached to the bottom of the frame, containing the battery and programming modules. The ASSMO was deployed next to an active bubble stream on Hydrate Hill on the 18th of March 2015, during ROV Dive 360. It was recovered four days later on the 22nd of March, during ROV dive 363. The sonar was programmed prior to the deployment with a detection range of 5 meters and a polar mode with a 360° scanning sector. It was set to scan for two minutes (4×360° rotations) every 30 minutes. The data was stored in the programming module within the format *.81a, and was replayed and analyzed with the IMAGENEX software.

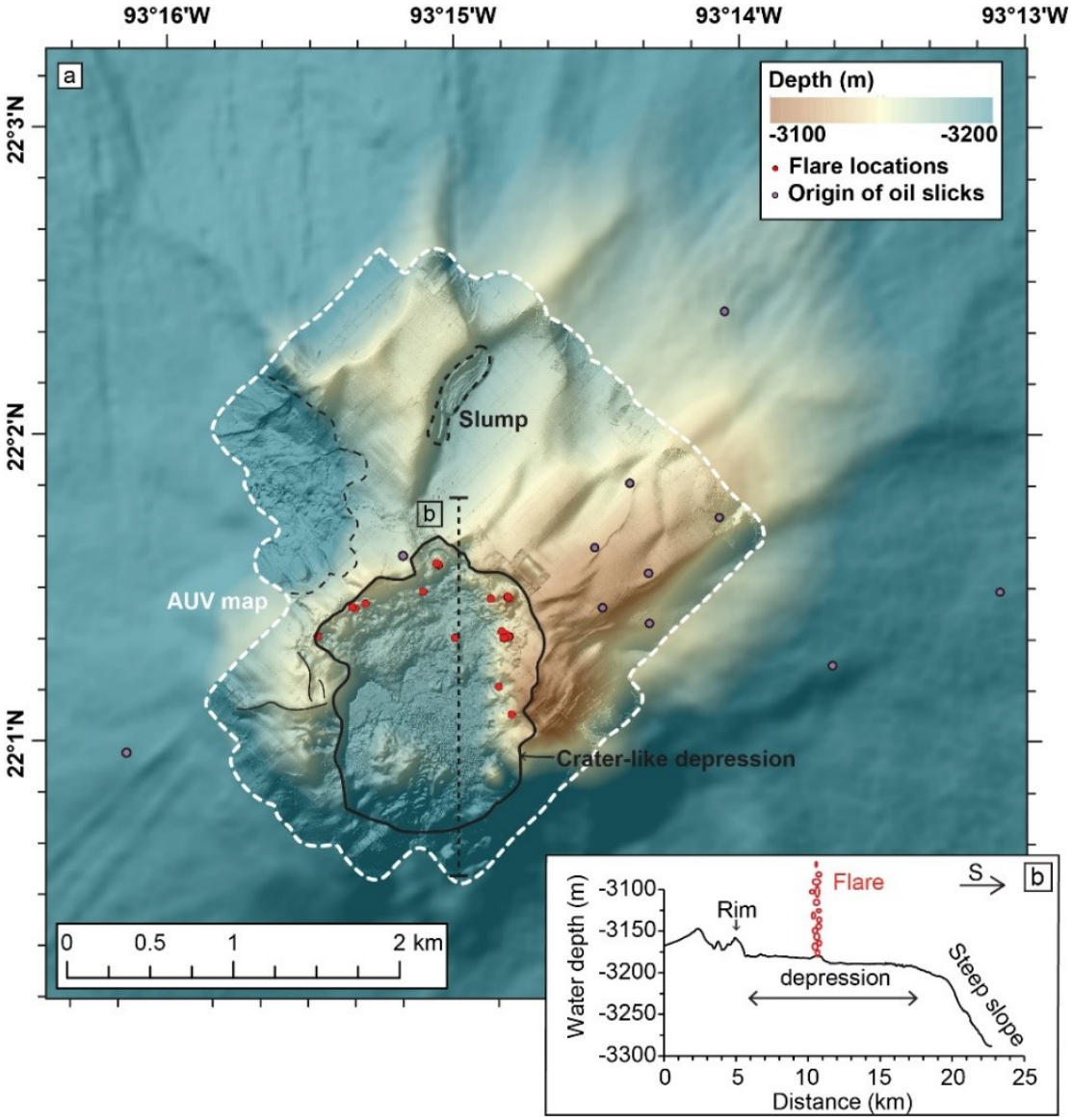


Fig. 6.2 (a) AUV-derived bathymetric map (outlined by white dash line) draped on ship-derived bathymetric map of the Mictlan Knoll and its surrounding area. The black line outlined a crater- like depression on the top of the knoll. The vertical projections of flare locations (red dots) were detected from AUV water column mapping. The origins of the sea surface oil slick locations (purple dots) are from the dataset reported by MacDonald et al. (2015) and Suresh (2015). The black dash lines outlined the area likely associated with the regional mass transport deposits. (b) The seafloor morphology profile crossing the depression of Mictlan Knoll in N-S direction illustrate that the depression was bounded to elevated rim features in the north and with an outlet to the south.

## 6.4 Results

### 6.4.1 Seafloor bathymetry and seafloor backscatter

Mictlan Knoll is an isolated sub-circular feature located in the central part of the Campeche-Sigsbee salt province (Fig. 6.1a), about ~20 km northeast off Chapopote Knoll (Fig. 6.1b) and 6 km north of Knoll H2154. Mictlan Knoll is ~7 km in diameter at the base and rises ~300 m

above the surrounding seafloor located at about 3300 m water depth (Fig. 6.1b). The high-resolution AUV bathymetry map covers an area of 9.3 km² (Fig. 6.2a) and reveals a large crater-like depression at the center of Mictlan Knoll.which stretches 1.8 km and 1 km in the NS and WE directions respectively, and several linear ridges outspreading around the depression (Fig. 6.2a). The depression is enclosed by an elevated rim, about 30 m high, to the West, North and East, but not towards the South where it is connected directly to the steep outer flank of the knoll (Fig. 6.2a and 2b). As shown in Fig. 6.2b, the highest point of the knoll is located to the north of the northern rim, at a maximum height of about 3150 mbsl. The water depth inside the depression gently increases from north (3180 mbsl) to south (3210 mbsl), where if sharply increases along the southern flank of the knoll down to the depth (~ 3300 m) of the surrounding seafloor. The radial ridges mainly occur in the northern as well as the northeastern top of the knoll, extending 2-3 km from the rim of the depression to the foot of the knoll. Most of them have a morphologically smooth transition from the crest to the flanks (Fig. 6.3) with a 5-10° slope angle. There is evidence of mass transportation and mass transport deposits around the top of the knolls. In particular, a distinct tongue-shape slump feature with a length 640 m and width 130 m is observed along a ridge, north of the knoll summit.

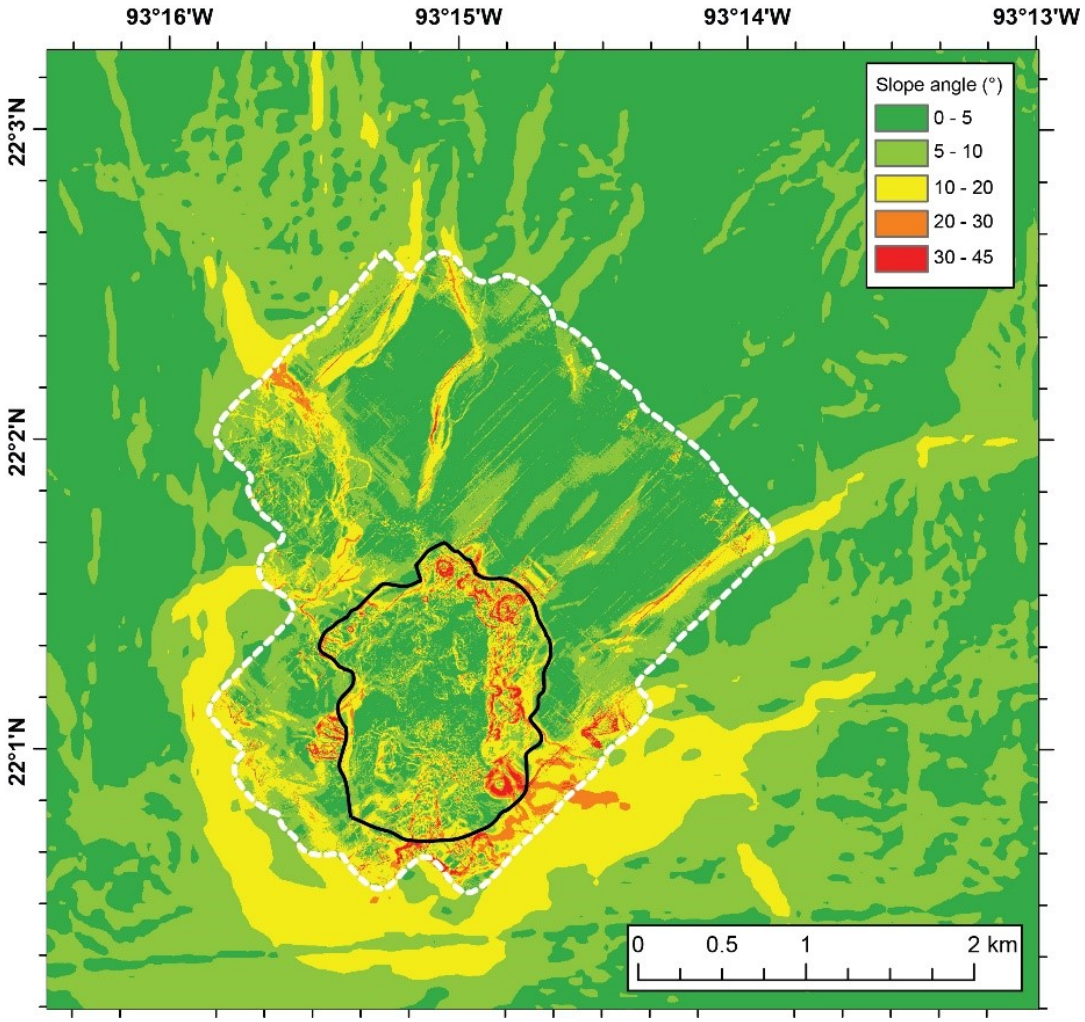


Fig. 6.3 AUV based slope map (outlined by white dash line) dapped on the ship based slope map of the Mictlan Knoll and its surrounding area, the extent shown in this map is identical to Fig. 6.2a. The slope angles were obtained by using the slope (Spatial Analyst) tool in the ArcGIS.

The seafloor morphology of the entire knoll is mostly smooth aside from the crater-like depression, which has a significantly rougher seafloor surface with numerous microstructures (Fig. 6.2a). The seafloor morphologies inside the depression are rather complex but can be divided into three zones based on differences in the observed seafloor morphology (divide by black dot lines in Fig. 6.4a): northern (zone 1), central (zone 2) and southern part (zone 3). Zone 1 is characterized by various doming features and a relatively bumpy seafloor morphology compared to the central part of the depression (zone 2). There is no significant variation of water depths within zone 2, which has a predominantely smooth surface. However, a rough seafloor surface is observed in the eastern side of zone 2. Zone 3 consists of two flat regions separated by a pronounced mound structure. The eastern side of zone 3 shows a more hummocky morphology with a rougher seafloor surface than the western side. A number of elevated features up to hundreds of meters in diameter and several small-scale depressions (meter to hundreds of meters in extent) can be seen along the rim of the depression.

According to the intensities of the seafloor backscatter reflectors, five categories of seafloor backscatter signatures have been made, including: high (> -33 dB), intermediate-high (-33 to -36 dB), intermediate (-36 to -38 dB), intermediate-low (-38 to -40 dB) and low (< -40 dB) backscatter (Fig. 6.4b). Apart from the depression, the seafloor backscatter signatures of Mictlan Knoll are generally homogenous with intermediate to intermediate-low backscatter signatures, which are similar to the surrounding abyssal seafloor. In the northeastern part of the depression, a distinct high backscatter area (high to intermediate-high) is observed as an oval-shape feature about 500 meters in length and 150 meters in width. High backscatter patches with more than hundred meters in diameter can also be found at the top of three mounds (outlined in red) (Fig. 6.4b). Further high backscatter patches with various shapes are also present, mainly located in the northern and the central part of the depression (Fig. 6.4b).

### 6.4.2 Seafloor observations

Visual seafloor mapping was conducted during three TV-sled surveys (GeoB19326-1, GeoB19341-1, and GeoB19347-1). The tracks surveyed the zones 1, 2 and 3 of the depression, as well as part of the rim area (Fig. 6.4a). The images show that asphalt deposits were extensively distributed inside the depression and around the eastern rim of the depression (Fig. 6.4a). Fig. 6.4b shows that the asphalt deposits are commonly associated with high and intermediate-high backscatter signatures. However, there are few exceptions, as the asphalt deposit areas at the north of the rim and in the western part of the depression are associated with intermediate backscatter signatures.

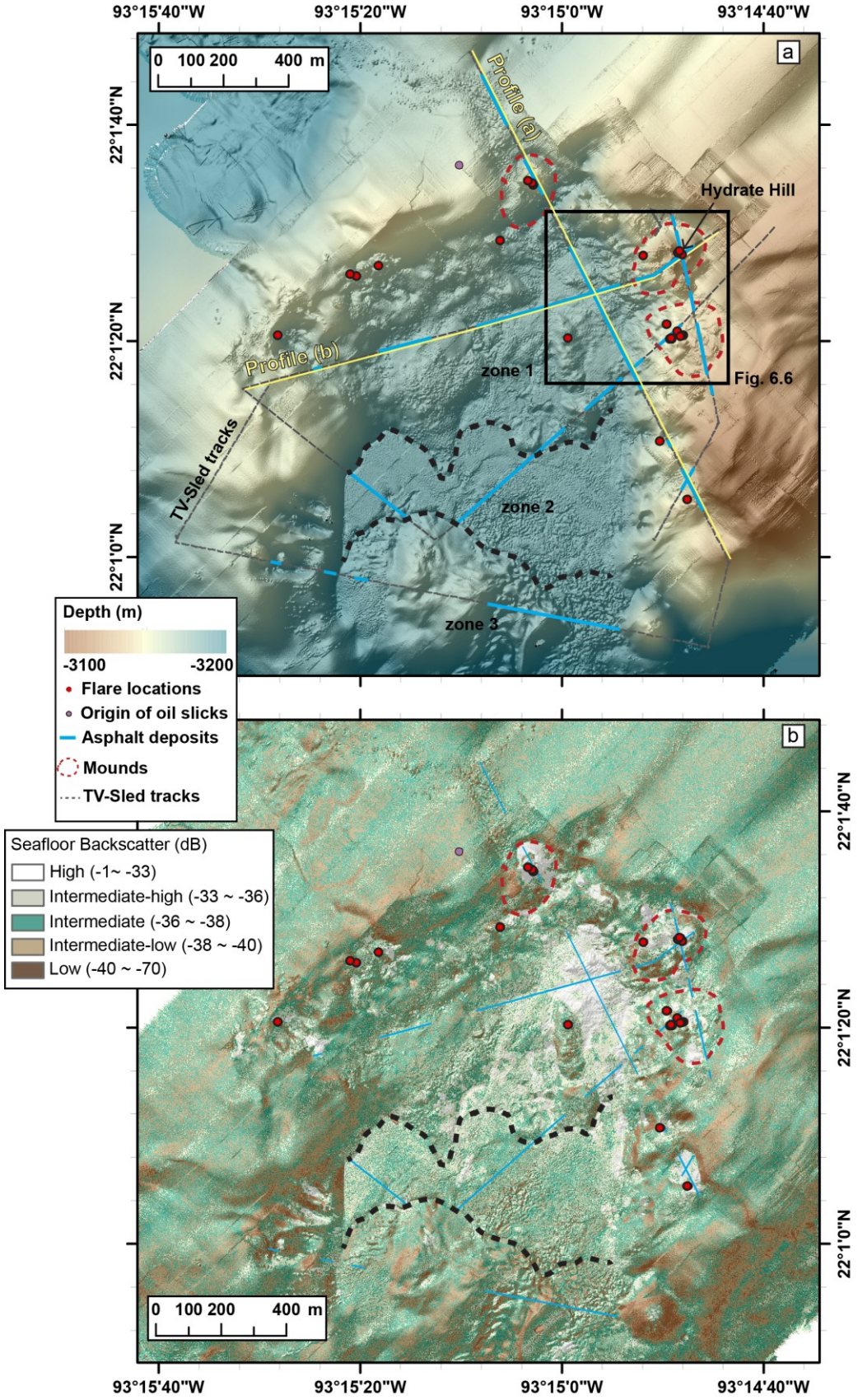


Fig. 6.4 (a) AUV-derived bathymetry focusing on the crater-like depression and its surrounding rim features of the Mictlan Knoll. According to the expressions of seafloor morphologies, the crater-like depression was divided into zone 1 (north), zone 2 (center), and zone 3 (south). The TV-sled tracks

(gray dash lines), vertical projections of flare locations (red dots) as well as the origins of the sea surface oil slick locations (purple dots) are shown. The solid blue lines indicate the regions where asphalt deposits were mapped during the TV-sled surveys. Black rectangle outlines the area investigated by ROV dives, corresponding to the area of Fig. 6.6a, b. Positions and orientations of TV-sled profiles across the depression of the knoll (yellow lines), shown in Fig. 6.5. (b) AUV-derived seafloor backscatter focusing on the crater-like depression and its surrounding rim features of the Mictlan Knoll. This map shows five categories from the high backscatter (-1~ -33 dB) to low backscatter (-40~ -70 dB).

Two profiles 5a and 5b illustrate the asphalt deposits mapped along with the seafloor morphology of the TV-sled tracks (Figure. 6.5a-b). A NW-SE profile (a) (Fig. 6.5a) started from the northern rim of the depression towards the eastern rim of the depression, crossing three flare sources. First, asphalt deposits were observed continuously for about 150 meters on the flat area north of the rim, then extensive asphalt deposits with tubeworm colonies covered the rim mound, on top of which flares were detected. In the middle of the profile (a), an area of extensive asphalt deposits extended about 400 meters, followed by hemipelagic sediments, until asphalt deposits appeared again within the depression and at the rim in the south. The location of the asphalt deposits along profile (a) correlates well with the areas of high and intermediate-high backscatter. A SW-NE profile (b) (Fig. 6.5b) started from the western rim of the depression across the zone 1 and ended at Hydrate Hill on the northeastern rim. Figure 6.5b shows two main areas of asphalt deposits, partially covered by sediments, and separated by 80 meters of thicker hemipelagic sediments (a total of over 600 meters in width) inside zone 1. At Hydrate Hill, the asphalt deposits extended from the southern flank to its top, where gas bubble streams have been observed.

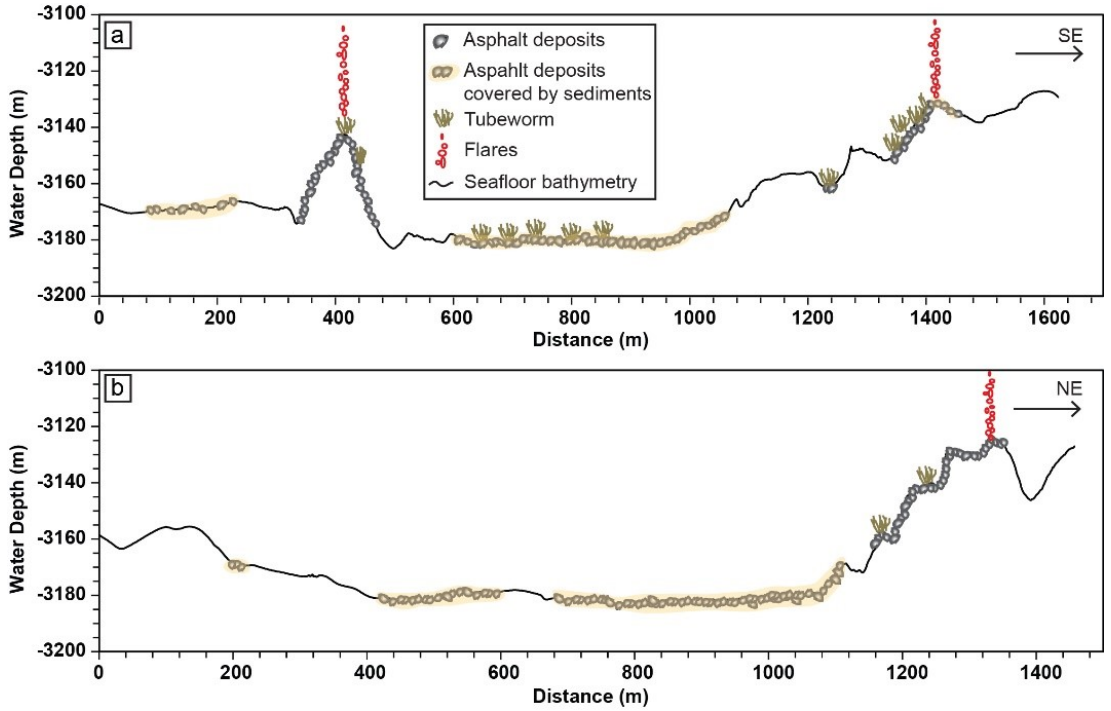


Fig. 6.5 (a) Schematic Profile a (location see Fig. 6.4a) along the TV-sled track illustrates the seafloor bathymetry and the visual seafloor observation from a NW-SE orientation. (b) Schematic Profile b (location see Fig. 6.4a) along the TV-sled track illustrates the seafloor bathymetry and the visual seafloor observation from a SW-NE orientation.

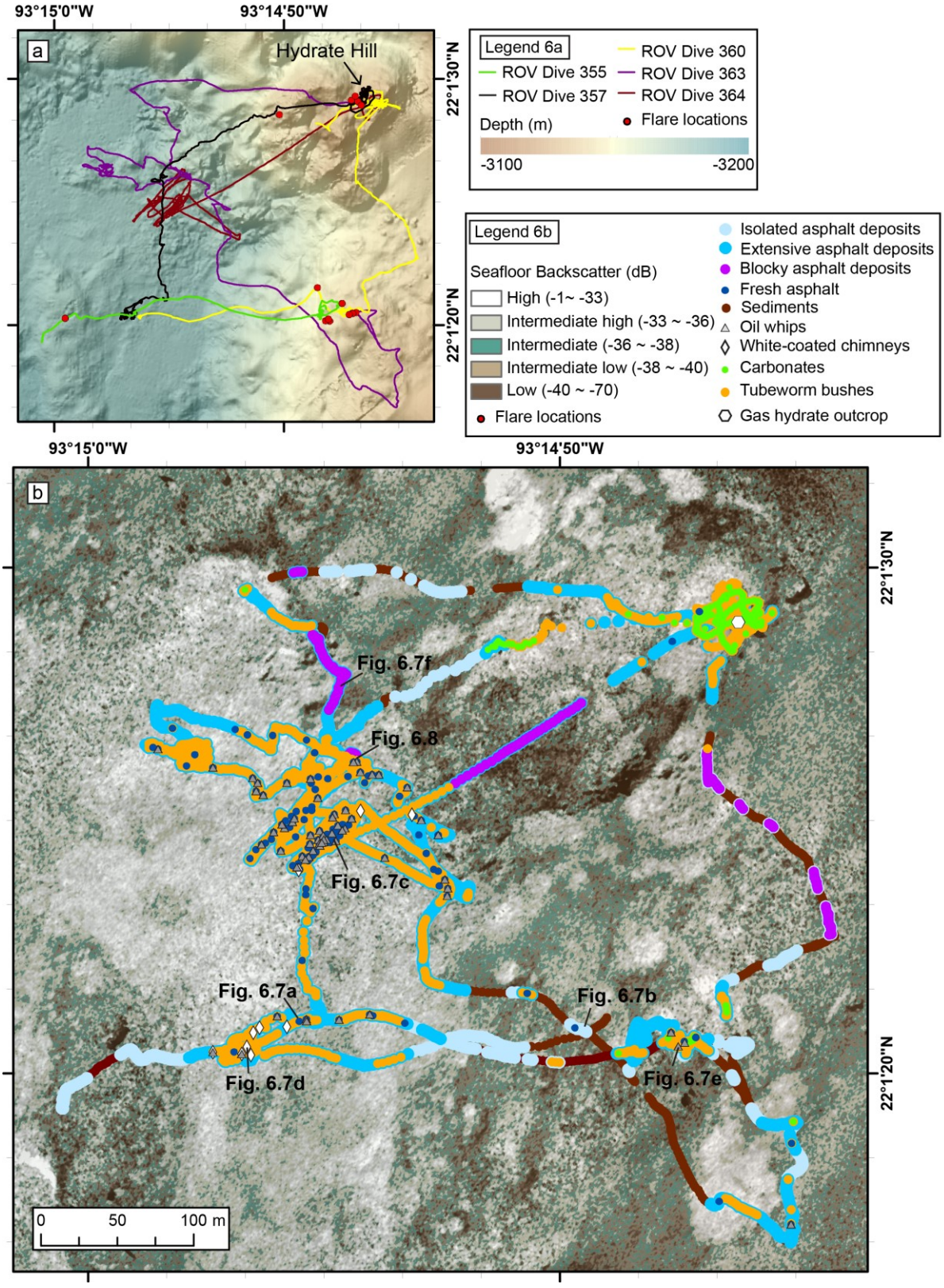


Fig. 6.6 (a) ROV QUEST dive tracks and vertical projections of flare locations plotted on AUV-based bathymetry. (b) Close-up of the AUV-derived seafloor backscatter focusing on the eastern part of zone 1. A detailed visual seafloor mapping illustrated the distributions of diversified hydrocarbon seepage which are indicated by symbols.

Detailed visual seafloor observations were conducted during five ROV dives and focused in the areas of the northeastern part of the depression and two mounds on the northeastern rim of the depression (Fig. 6.6a). ROV surveys aimed to investigate the asphalt deposits areas, which were revealed by the TV-sled surveys and to investigate three gas emission sites. Confirming the observations from TV-sled surveys, asphalt deposits were widely distributed at the seafloor in this area, except in some regions only covered by sediment in the surrounding of two main elevated features at the rim (Fig. 6.5b). However, the high-resolution images and videos acquired by the ROV allowed us to further categorize the seafloor facies into different groups including extensive asphalt deposits, isolated asphalt deposits, blocky asphalt, fresh asphalt, oil whips, white coated-chimneys, tubeworm bushes, carbonates, and sediments (Fig. 6.6b).

Most of the asphalt deposits co-occurred with tubeworms bushes (colonies of more than ten tubeworms were categorized as tubeworm bush) and covered by a thin layer of sediment. Areas with consecutive asphalt deposits at the seafloor are defined as extensive asphalt deposits (Fig. 6.7a). These areas were mainly located at the flat area inside the depression and at the top of the mounds (Fig. 6.6b). Isolated asphalt deposits (Fig. 6.7b) were characterized by asphalt deposits that occur as isolated patches surrounded by hemipelagic sediments at the seafloor. They were generally located at the transition area between the depression and the rim. Large solidified asphalt deposits are defined as blocky asphalt (Fig. 6.6f), which were found abundantly at the slope between the depression and Hydrate Hill and discontinuously distributed along the eastern rim of the depression. Relatively smooth asphalt deposits appearing to represent a fresh outflow (Fig. 6.7c) or relatively recent asphalt edifices (Fig. 6.7c) were classified into the group of fresh asphalt. Oil drops released from the seafloor were mainly observed from white-coated tubes (Fig. 6.7d) and from the viscous whip-shaped extrusion defined as oil whips (Fig. 6.7e). Abundance of fresh asphalt, oil whips and white-coated chimneys were observed in the area associated with extensive asphalt deposits inside the depression, only a few exceptions were found on the rim of the depression (Fig. 6.6b).

A mosaic was assembled from seafloor images at the flat area of the depression (location see Fig. 6.6a). It shows an area extensively covered by asphalt deposits (Fig. 6.8). The northwestern side of the mosaic shows an oval-shaped fresh asphalt flow, covered by white microbial mats. Various asphalt shapes, including fragmented asphalt, ropy asphalt, and domed asphalt can also be seen in the surrounding area of the fresh asphalt flow. Tubeworm bushes were partly buried by the fresh asphalt flow at its surroundings, and a few galatheid crabs were found grazing at surface of the fresh flow.

Hydrate Hill is a large gas hydrate outcrop about 50 cm wide and 100 cm high at the top of the mound, where a gas bubble stream was visually observed (Fig. 6.9a). The seafloor surface of Hydrate Hill was entirely covered by a dense population of vestimentiferan tubeworms and characterized by the presence of authigenic carbonates. No asphalt deposits were observed at the seafloor in the vicinity of Hydrate Hill.

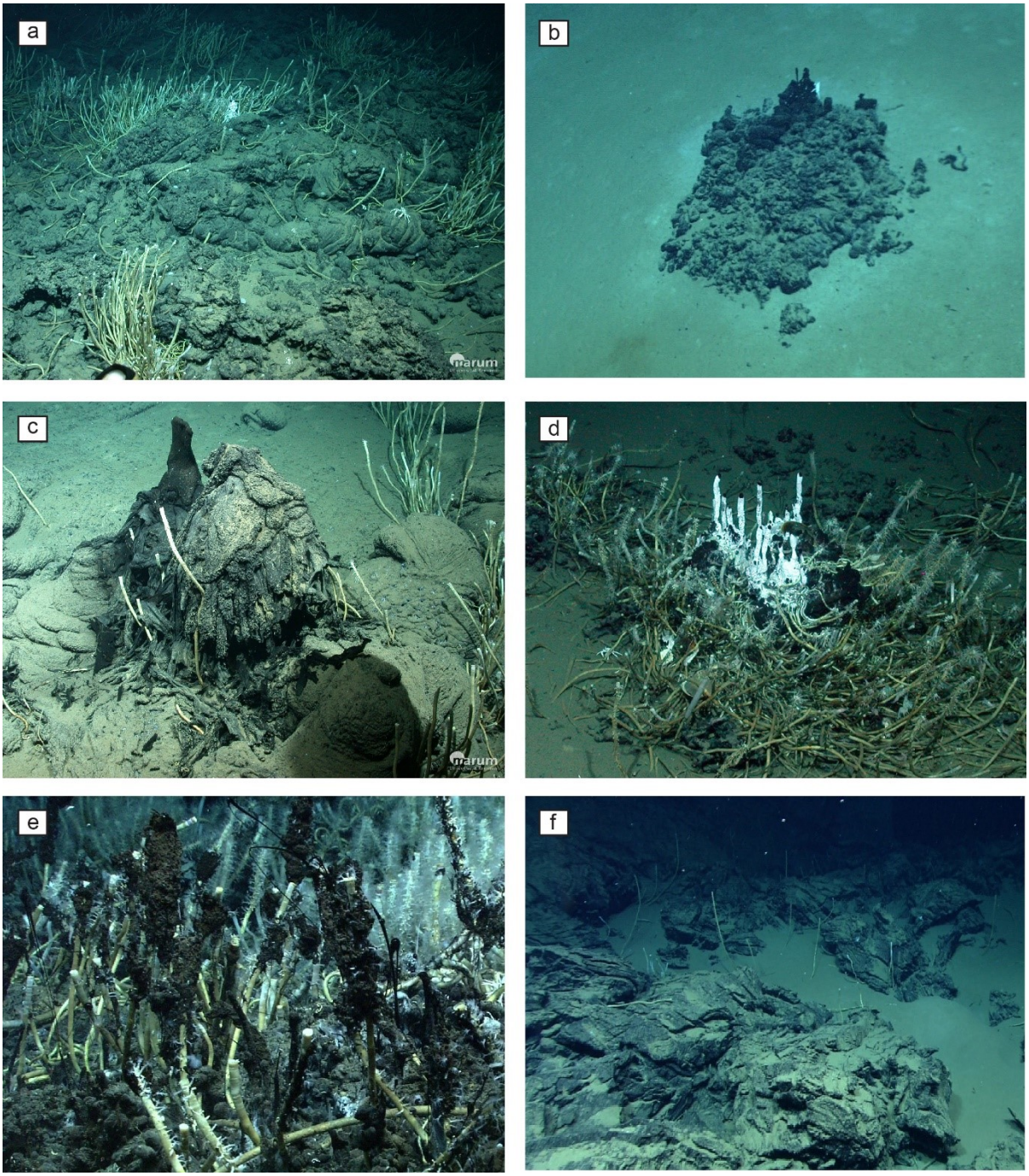


Fig. 6.7 Seafloor images captured from video camera mounted on ROV QUEST at Challenger Knoll along ROV surveys. The locations of the images are indicated in Fig. 6.6b (a) Extensive asphalt deposits with tubeworm bushes. (b) Isolated asphalt deposits surrounded by the hemipelagic sediment. (c) A fresh asphalt edifice extruded from the fresh asphalt flow. (d) Oil drops released from the white-coated chimneys which located on the top of the tubeworm bushes. (e) Viscous oil drops emanated from seafloor formed the whip-like features. (f) Large and extensive solidified blocky asphalt deposits.

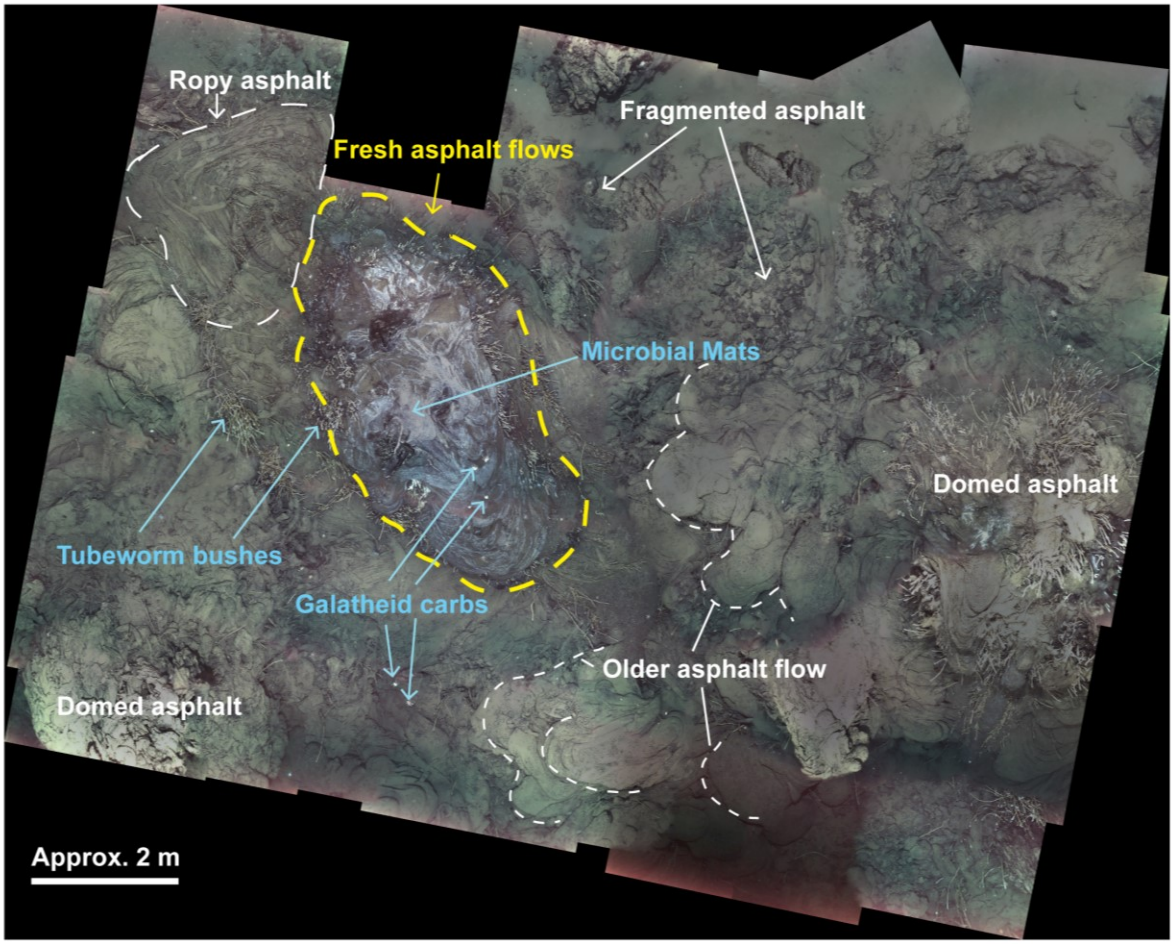


Fig. 6.8 Photomosaic of an extensive asphalt deposits site from ROV dive 363 (location see Fig. 6.6b). An oval-shaped of fresh asphalt flow was covered by the white microbial mats. Tubeworms bushes and few galatheid crabs were observed at or around the fresh asphalt flow. Fragmented asphalt, ropy asphalt, and a domed asphalt were observed adjacent to the fresh asphalt flow.

### 6.4.3 Gas emissions

Twenty-five flares were observed across the Mictlan Knoll at water depths between 3120 mbsl and 3178 mbsl (Fig. 6.2). With only one exception, all flare sources were distributed along the northern and eastern rim of the depression. Many flares along the rim (17 out of 24) were concentrated at the tops of three mounds. Only one flare was detected inside the depression. It was located at the top of an elevated feature in the eastern part of zone 3 (Fig. 6.3a). Most flares (22 of 25) were located in areas characterized by higher backscatter or intermediate-high backscatter (Fig. 6.3b). The remaining three flares were detected in areas of intermediate to low backscatter signatures; one was located inside the depression, the two others were located on the northern side of the rim.

One gas bubble stream was investigated during an ROV survey of “Hydrate Hill”, a mound located at the northeastern rim of the depression (Fig. 6.3a). Visual analysis of this bubble stream (Fig. 6.9b) resulted in a bubble size distribution that follows a Gaussian distribution with the average equivalent spherical radius of $r_e = 0.292 \pm 0.059$ cm (Fig. 6.10). A total of 67 bubbles were analyzed with maximum and minimum $r_e$ was 0.438 cm and 0.136 cm,

respectively. A total of 637 gas bubbles were emitting from the seafloor in 347 seconds, according to the duration of visual observation. The resulting bubble emission rate at this site was 1.84 bubbles per second. The average molecular composition of gas bubbles (expressed as the ratio of methane: ethane: propane: *i*-butane) is about 99.48%: 0.2%: 0.2%: 0.1%.

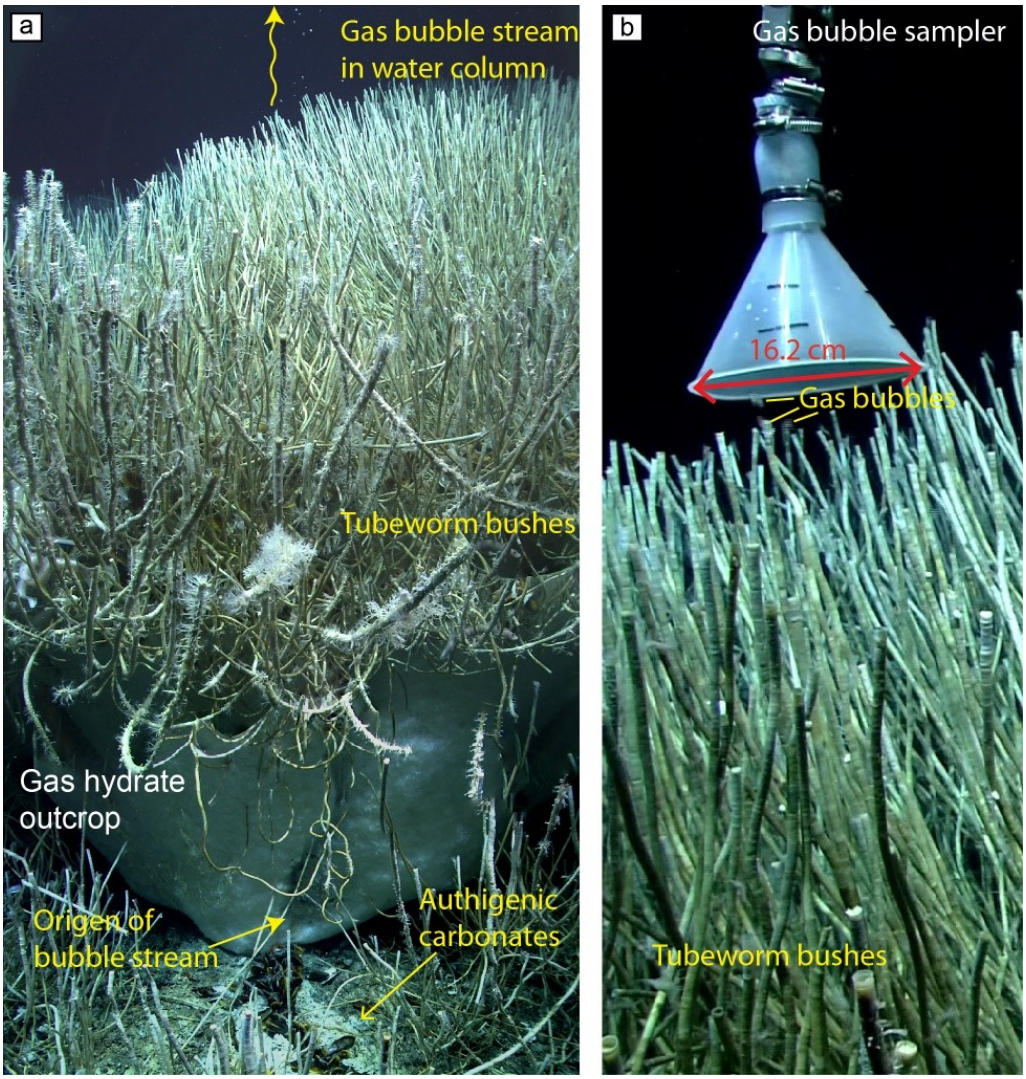


Fig. 6.9 (a) A gas hydrate outcrop is located at the Hydrate Hill (location see Fig. 6.4a). Authigenic carbonate layers were observed at the bottom of the gas hydrate. A dense of tubeworm bushes were colonized the top of the gas hydrate. A gas bubble stream was rising through the gas hydrate and the tubeworm bushes. (b) The gas bubbles were sampled by a gas bubble sampler (GBS) and analyzed for their molecular composition. Based on the imagery analysis, a total of 67 gas bubbles were measured for their sizes.

ASSMO was deployed between 1 and 2 meters away from a bubble plume site at the top of Hydrate Hill. The gas emission activity is represented by mean sonar backscatter value recorded by the sonar. A total of 652 datasets were analyzed for its activity from 18 March to 22 March 2015. The activities of gas emission are not consistent during the time of observation. The mean sonar backscatter values range from 6.2 to 84.5 (dB) during the time of deployment. The time series of gas emission activities is shown in Fig. 6.11. The moving average of gas emission activities was calculated illustrated as blue line in Fig. 6.11.

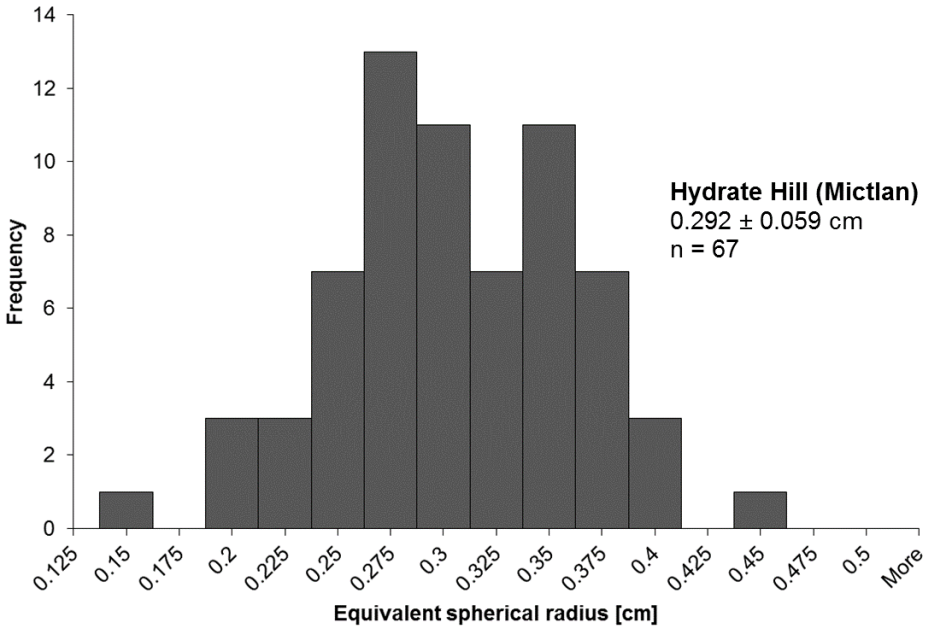


Fig. 6.10 Bubble size distributions of emanating bubbles at the Hydrate Hill showed a Gaussian-type distribution.

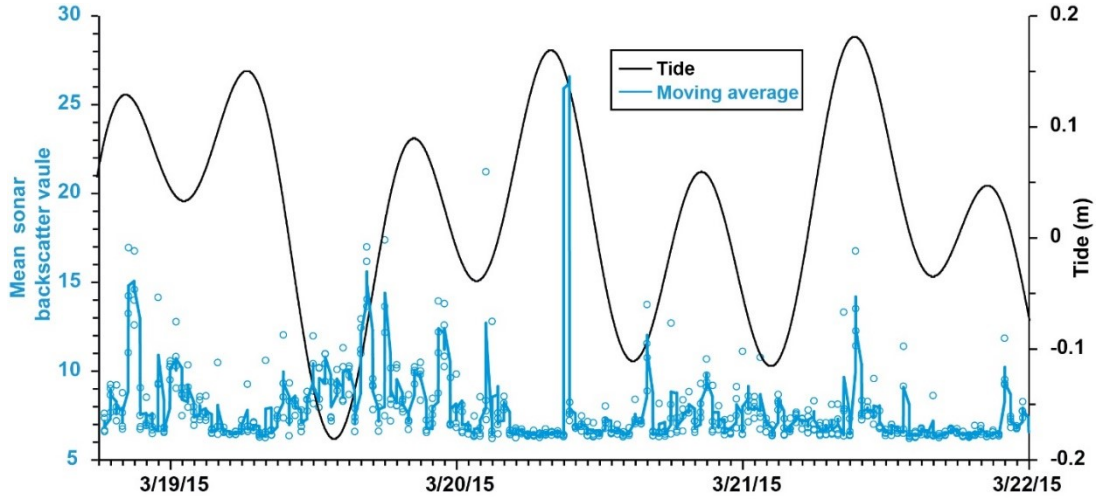


Fig. 6.11 Time series plot of the gas emission activities (open blue circles) with moving average (blue line) analyzed from the ASSMO deployment at Hydrate Hill over 77 hours combined with the extracted tidal data (black curve).

## 6.5 Discussion

### 6.5.1 Seafloor morphology

The seafloor morphology of Mictlan Knoll is a sub-circular knoll similar to Chapopote Knoll, characterized by the distinct crater-like depression at their top. Unlike the depression at Chapopote, which is fully enclosed within an elevated rim feature, the depression at the Mictlan Knoll is directly connected to the southern flank of the knoll. The depression (1.5 km wide, 60 meters deeper than the rim) at the Mictlan Knoll is larger and deeper than the depression (500 meters wide, 50 meters deeper than the rim) at the Chapopote Knoll (Ding et al. 2008). In addition, Mictlan Knoll and Chapopote Knoll are both located in the Campeche salt province where the salt features rise to very shallow depths (Salvador 1991b) associated with various regional deformation events (Cruz-Mercado et al. 2011; Sánchez-Rivera et al. 2011). The deformation history of Mictlan Knoll is likely to be analog to that of Chapopote Knoll, i.e. caused by an active salt feature piercing the sediments or by regional compression events mobilizing the buried salt feature (Ding et al. 2010). The hydrocarbon seepage in the deep GoM basin is associated with salt tectonic (Ding et al. 2010; Ewing et al. 1969a; Hsu et al. 2019). Although we do not have the seismic evidence for the salt features underneath the Mictlan Knoll, the presence of diversified hydrocarbon seepage in the Mictlan Knoll is likely to reflect the present salt activity in the subsurface.

Asphalt deposits have been observed in the depression at both Mictlan Knoll (Sahling et al. 2016) and Chapopote Knoll (Brüning et al. 2010; MacDonald et al. 2004). However, the area of extensive asphalt deposits in the northeastern part of the depression at Mictlan Knoll might reach up to 75,000 $m^2$, which is much larger than the main asphalt area (~2000 $m^2$) observed in the southwestern part of the depression at Chapopote Knoll (Brüning et al. 2010). Although recent work suggested that larger sediment-covered asphalt deposits may occur at Chapopote (Marcon et al. 2018), these findings indicate the Mictlan Knoll may host some of the largest asphalt deposits so far known in the southern GoM.

### 6.5.2 Seafloor manifestations of hydrocarbon seepage

Natural hydrocarbon seepage is a widespread process in the southern GoM. This has been evidenced by the presence of oil slicks from the satellite images (MacDonald et al. 2015; Suresh 2015; Williams et al. 2006) and the occurrence of chemosynthetic fauna, asphalt deposits, authigenic carbonates from visual seafloor observations at 12 sites (Sahling et al. 2016). While the previous studies only focused on the Chapopote asphalt volcano (Brüning et al. 2010; MacDonald et al. 2004; Marcon et al. 2018), this study sets investigates the detailed hydrocarbon seepage distribution at Mictlan Knoll as another asphalt volcano in the Campeche Knolls.

The Mictlan asphalt deposits cannot be classified into distinct flow units as it was done at Chapopote (Brüning et al. 2010; Marcon et al. 2018), where the youngest asphalt flow units tend to cover older flow units. Although our observations at Mictlan encompass a much larger area than what was described at Chapopote, the Mictlan image surveys in the depression showed relatively rough asphalt deposits, partially covered by sediments and in parts densely populated with tubeworms (Fig. 6.4). Tubeworms are generally considered to have relatively

slow growth rates (Fisher et al. 1997), for example, 2 meters long of vestimentiferan tubeworm from the continental slope of northern GoM required ~ 200 years to grow (Bergquist et al. 2000). Therefore, the presence of abundant tubeworm communities suggests that the Mictlan asphalt deposits are older than the youngest asphalt units of Chapopote (Marcon et al. 2018), where the tubeworm communities were relatively rarely observed.

Furthermore, unlike at Chapopote, we did not observe such dense and extensive microbial mats or fresh asphalt pools at Mictlan, making it difficult to precisely identify the location of the main asphalt outflow conduit (Marcon et al. 2018). However, the most active area seems to be located near the northeast of the depression (eastern part of zone 1), where one intermediately dense microbial mat (Fig. 6.8), as well as numerous oil whips and white-coated chimneys were observed (Fig. 6.5b). Oil whips and white chimneys infer that existing deposits still contain mobilized lighter asphalt in their core, which is leaking out (Brüning et al. 2010; Sahling et al. 2016), indicating that the fresh asphalt from below is piercing out and slowly seeping through the overlying deposits.

The high backscatter patch in zone 1 corresponds to where the asphalt deposits are extensive and heavily colonized with tubeworms (Fig. 6.5b). Because of their need for hard substratum (Boetius 2005; Cordes et al. 2009), tubeworms are known to be associated with high backscatter areas (Marcon et al. 2014). This is caused by the fact that tubeworms occur on the hard substratum (usually carbonates) and not by the tubes themselves, which tend to slightly lower the overall backscatter (Sen et al. 2016). Tubeworms are known to grow very slowly (Bergquist et al. 2000; Fisher et al. 1997) and their high abundance indicates that these deposits are relatively old. Old asphalt deposits tend to be more fragmented and harder than fresh deposits due to the loss of relative lighter compounds (Brüning et al. 2010; Marcon et al. 2018; Schubotz et al. 2011a). This is further supported by the images, which show that the surface of the asphalt deposits in those areas is rough and does not exhibit smooth features typical of fresh asphalt (Marcon et al. 2018). Finally, the occurrence of tubeworms in the high backscatter area of zone 1 indicates that hydrocarbon seepage below the surficial deposits is still active, or at least that the core of the deposits still contains sufficient light hydrocarbons to fuel chemosynthetic life.

The lower backscatter areas within the crater-like depression (zones 1-3) (Fig. 6.3b) seem to be covered by thin sediments (likely over asphalt) and by isolated, non-continuous asphalt deposits. The sediment covered asphalt deposits have been observed in a broad area in the lower backscatter area of zone 1 (Fig. 6.4b) and may be the reason for the relatively lower seafloor backscatter in this area. This finding may reveal that there may be more asphalt deposits covered by sediments, which cannot be observed at the seafloor surface. Indeed, the bumpy seafloor morphologies observed in zone 1 may be caused by outflows of fresh asphalt below the old deposits. By contrast, the relative smoothness of zones 2 and 3 may indicate the absence of asphalt outlets underlying the asphalt deposits. Sediment-covered asphalt deposits are more likely to be older than the deposits present in the high backscatter patch of zone 1. Indeed, the lesser occurrence of tubeworms shown by the video surveys indicates that the supply of hydrogen sulfide and, hence of light hydrocarbon from below the surface is too low to sustain chemosynthetic life. Areas devoid of tubeworms are likely inactive in terms of hydrocarbon seepage.

### 6.5.3 Distribution and quantification of gas emission

Gas emissions sites were mostly located at the rim of the crater-like depression of the Mictlan Knoll (Fig. 6.3). In addition, many of them were concentrated on the top of the three mounds from the eastern rim. These findings show that there is effective hydrocarbon migration pathways in the subsurface along the rim of the crater-like depression. Therefore, free gases can transport upward through fractures or conduits in the subsurface and release from the seafloor surface into the water column. This is analogous to the gas releasing at the ring fault structure from mud volcanoes. During the extrusion of mud and fluids through the plumbing system of a mud volcano, the material loss in the subsurface can cause the formation of caldera-like crater surrounding by inward-dipping ring faults (Loher et al. 2018b; Loher et al. 2018c; Mazzini et al. 2009; Planke et al. 2003). These ring faults have been suggested to act as potential fluid migration pathways forming upward branching fluid discharge at deep sea mud volcanoes (Loher et al. 2018c). However, the Mictlan Knoll is not a mud volcano, and the formation of the depression cannot be constrained yet. Ding et al. (2008) suggested that the similar crater-like depression at Chapopote Knoll could be caused by regional normal faulting, or by sediment collapse after fluid release. Therefore, we suggest that the formation of crater-like depression at the Mictlan Knoll can be considered as a result of the material loss in the subsurface. This mechanism is similar to the formation of the caldera-like crater of a mud volcano. Therefore, the inward-dipping ring faults might also be found in the subsurface along the rim of the depression at Mictlan Knoll and provide effective migration pathways for gas emissions.

No gas emission sites were observed within the area of extensive asphalt deposits inside the depression of Mictlan Knoll during our survey. This finding may be due to the fact that extensive asphalt deposits in the subsurface reduce the permeability in the sediments and prohibit vertical migration of gas bubbles (Ding et al. 2008). Therefore, the gases tend to migrate laterally and release from the seafloor at the edge of asphalt fields, i.e. at the rim of the depression. These results further support the gas migration model proposed by Ding et al. (2008) at Chapopote Knoll. They suggest that a thick layer of solid asphalt deposits can lead to form an effective seal that prevents the vertical gas migration in the asphalt field and induce the lateral migration of gas bubbles to the edge of the asphalt field.

In order to estimate the gas bubble volume contributing from the gas bubble stream above the Hydrate Hill to the hydrosphere, the sizes of the gas bubble and the frequency of gas bubble emission were considered. Assuming that gas emission rate is constant (1.84 bubbles per second) and the size of all gas bubbles is equal to average measured bubble size ($r_e = 0.292$ cm), a total volume emitting of 11.5 ml/ min is calculated. This volume can be converted to the mass output which account for a methane release from this emission site: 0.09 x$10^6$ mol $CH_4$/yr. This amount of methane flux is one to two orders of magnitude lower than other gas bubble streams quantified in the GoM. For example, bubble plumes at GC185 and GC600 in the northern GoM were found to emit respectively 0.24 x$10^6$ mol $CH_4$/yr and 0.45 x$10^6$ mol $CH_4$/yr (Johansen et al. 2017; Leifer and MacDonald 2003) and single gas bubbles streams at Tsanyao Yang Knoll were estimated to emit from 0.48 to 4.06 x$10^6$mol $CH_4$/yr (Römer et al. 2019).

However, the gas emission activity at the Hydrate Hill is not steady, and the ASSMO data show that the seepage is very variable even over a short period of time (77 hours). Correlation with

the tide is not evident based on the available data (Fig. 6.11). Several significant peaks seem to coincide with high tide, unlike what was observed in other places (Hsu et al. 2013; Römer et al. 2016), where elevated pressure is believed to reduce sediment transmissivity and, hence, reduce the bubble outflow. It could be due to the fact that the added pressure on the system flushes the gas out of the asphalt towards the rim of the volcano, temporarily increasing the effluxes. However, more analyses would be necessary to test this hypothesis. Alternatively, asphalt dynamics may likely influence the gas seepage.

## 6.6 Conclusions

The distribution of diversified hydrocarbon seepage from the seafloor, including gas seepage, oil seepage, asphalt deposits and gas hydrate at Mictlan Knoll is reported. In this study, we combined the visual seafloor observations with high resolution of AUV-based bathymetry and seafloor backscatter to illustrate the seafloor manifestation of the hydrocarbon seepage at Mictlan Knoll.

Mictlan Knoll hosts the largest area of extensive asphalt deposits known so far in the GoM. The asphalt deposits are widely distributed and mostly constrained within the crater-like depression and inner flanks of the rim. Our seafloor observations suggest that at high backscatter area (75,000 $m^2$) of zone 1 was covered by extensive asphalt deposits. Numerous fresh asphalt and oil seepage (from white chimneys and oil whips) were found and further fuel the chemosynthetic communities such as tubeworms in this area. In contrast to the high backscatter area, the remaining part of zone 1 is characterized by relatively lower backscatter possibly caused by the presence of soft sediments on top of the asphalt deposits. The bumpy seafloor morphologies observed in this area are interpreted as outflows of fresh asphalt below the older surficial deposits. Zone 2 and zone 3 are areas covered with old asphalt deposits that flowed downslope from zone 1. The surface of zone 3 is slightly rougher and more fractured than that of zone 2, likely because of a steeper slope (Fig. 6.3 and 6.4a), which causes old deposits to crack.

The gas emission sites were generally located at the rim of the depression, and there is no gas emission site within the extensive asphalt area. These findings indicate that the asphalt deposits in the subsurface formed an effective seal that prevents vertical gas migration. Thus, the gas or lighter hydrocarbons migrate laterally towards the rim where the gases migrate upward along fractures and release in the water column. These findings are in accordance with the distribution of gas emission sites at Chapopote Knoll.

Mictlan Knoll is believed to be an analog to Chapopote Knoll, and have a similar deformation history associated with salt tectonism and asphalt volcanism. If a fresh asphalt flow would pierce through the old surficial deposits of Mictlan Knoll, then we might observe a scenery like at the main asphalt field of Chapopote Knoll, with smooth flow deposits on top, few to no tubeworms and large microbial mats. However, according to our observations at Mictlan Knoll, the younger asphalt flows did not break through the older deposits sufficiently to cover them up. The numerous fresh asphalt, oil whips and white chimneys were widely spread in the extensive asphalt area at Mictlan Knoll. This finding indicates that the fresh asphalt flows are localized with smaller scales than the main asphalt flow observed in Chapopote Knoll.

### 6.7 Acknowledgements

We sincerely appreciate the excellent cooperation from the captain and the crew of R/V METEOR during cruise M114 as well as the professional assistance of the scientific and technical operating teams of the ROV 'MARUM Quest 4000m' and AUV 'MARUM Seal'. We are very grateful to the Mexican authorities for granting permission to collect the multidisciplinary data from Mexican national waters (permission of DGOPA: 02540/14 from 5 November 2014). Our sincere thanks go to Marta Torres (Oregon State University) and Patrizia Geprägs (MARUM) for their contribution on the geochemical data analysis. Additional thanks go to, Jan-Derk Groeneveld, Tiago Biller, Nils Brückner and Stefanie Gaide (both MARUM) for their support on MBES data processing. Cruise M114 was funded by the German Research Foundation (DFG – Deutsche Forschungsgemeinschaft) through the cruise proposal "Hydrocarbons in the southern Gulf of Mexico". Additional funding was provided through the DFG-Research Center/Excellence Cluster "The Ocean in the Earth System". C.-W. Hsu would like to thank the Deutscher Akademischer Austausch Dienst (DAAD) for providing a scholarship (program ID: 57048249). I.R. MacDonald acknowledges support from the Gulf of Mexico Research Initiative ECOGIG 2 consortium for participation in the M114 cruise.

# 7. Conclusions and outlook

This cumulative dissertation investigated the different hydrocarbon systems associated with numerous seafloor structures in the Campeche-Sigsbee salt province, the southern Gulf of Mexico (GoM). The entire work aims to characterize the distribution of hydrocarbon seepage in this area through detailed seafloor mapping. The distribution pattern of the gas bubble emission sites from the entire study area to the individual structures was summarized in this work. At Challenger Knoll and Mictlan Knoll, the seafloor manifestations of the hydrocarbon seeps were illustrated by visual seafloor observations. All datasets presented in this work were acquired during the research cruise: RV METEOR cruise M114 visiting the southern GoM in 2015. A systematic hydroacoustic survey for active gas bubble emission sites was first reported in the southern GoM and documented the deepest gas emissions at Challenger Knoll sourcing at ~3600 mbsl observed thus far known from the GoM. The seafloor investigations revealed that the Mictlan Knoll hosts different types of hydrocarbon seepage in a large area (~75,000 $m^2$) of extensive asphalt deposits.

The aim of the first manuscript in this work was to gain a better understanding of the hydrocarbon seepage system influenced by salt tectonism, including the seafloor structures, distribution of seep sites, and hydrocarbon migration pathways by characterizing the active gas emissions at the Campeche-Sigsbee salt province. The second manuscript of this work focus on the distributions and characteristics of hydrocarbon seepage at Challenger Knoll. The goal was to determine the current activities of hydrocarbon seepage and potentially unravel the mechanism of hydrocarbon migration in the subsurface. The third manuscript sets out to deepen the knowledge on the processes which led to the formation of various seep structures associated with asphalt volcanism at the Mictlan Knoll by integrating seafloor mapping with visual seafloor observations.

Gas emission sites distributed widely in an area of ~19,600 $km^2$ from the Campeche-Sigsbee salt province in the southern GoM. A total of 209 flares indicative for gas emission sites were detected in the water column through a systematic hydroacoustic survey in this area. The gas emission sites occur mainly at the location associated with positive seafloor structures (e.g., knolls and ridges) rather than at the abyssal plain. A detailed bathymetry map revealed that this salt province has a complex seafloor morphology, which is composed of numerous knolls and ridges. According to the similarity of seafloor morphology, more than 40 individual seafloor structures were categorized into four principle structure types: Chapopote-type knolls, Flat-topped-type knolls, Furrow-type ridges, and Asymmetric-type ridges. The formation of these seafloor structures is believed to be caused by different regional deformation events associated with the salt tectonism. The shallow sediment deformation styles significantly control the processes of hydrocarbon migration in the subsurface. By integrating the results from seafloor mapping with the distribution of gas emission sites, conceptual models for gas seepage processes are proposed for each of the four structures. (1) Chapopote-type knolls: gas emission sites are generally located along the rim of the central crater-like depression. This phenomenon may be caused by the formation of inward-dipping ring faults during the development of the crater-like depression. These faults are considered to provide effective pathways for gas migration in the sediment. In addition, asphalt deposits (e.g., Chapopote Knoll and Mictlan Knoll) and gas hydrates in the subsurface are proposed to have created a temporary seal, causing lateral fluid migration so that fluids migrate upward and toward the rim of the crater-like depression. (2) Flat-topped type knolls: gas emission sites are generally

distributed around the edges of the knolls (e.g., Challenger Knoll). The gas migration pathways are highly constrained by the underlying salt in the subsurface. The underlying salt in the subsurface of the knoll prevents the vertical gas migration and induces lateral gas migration to the edge of the knoll. The gas emissions at the edge of the knoll are suggested to be associated with the vertical fluid migration pathways provided by the salt-sediment interface or the faults formed above the edges of the salt diapir. (3) Furrow-type ridges: gas emission sites are distributed primarily along the crests or furrow-like depressions. The seafloor morphology of this type suggests that it is related to the fault systems, which could form the effective conduits to allow hydrocarbons to migrate to the seafloor. (4) Asymmetric-type ridges: gas emission sites occur at the top of the crest or the chaotic flanks. Vertical fluid migration pathways are constrained by the underlying salt and the thickness of the sediment. These findings indicate that the shallow sediment deformation styles significantly control the processes of hydrocarbon migration in the subsurface.

Sigsbee Knolls and Campeche Knolls share a similar geologic history. However, there are still significant differences between these two areas. The seafloor structures in the Sigsbee Knolls are mainly comprised of individual flat-top knolls. In the Campeche knolls, the seafloor structures are much more complex. Our results suggested that there may be different types of hydrocarbon reservoirs in these two areas. In contrast to the findings of various types of hydrocarbon seepage (asphalt deposits, gas, and oil seepage) in the Campeche Knolls, only gas emissions were observed in the Sigsbee Knolls. Surface oil slicks have been reported previously form studies in the Sigsbee Knolls. However, neither satellite imagery nor ship-based observations detected floating oil during the M114 cruise. This suggests that oil seepage is an intermittent process in the Sigsbee abyssal settings.

In a final study, the distribution of different types of hydrocarbon seepage at Mictlan Knoll was investigated. A detailed seafloor mapping and visual seafloor observation revealed the seafloor manifestations of diverse hydrocarbon seepage and suggested that the Mictlan Knoll hosts the largest area of extensive asphalt deposits known so far in the southern GoM. Asphalt deposits are widely distributed within the crater-like depression. The various seafloor morphologies at different region inside the depression, representing the processes which led to the asphalt flow are complex. The bumpy seafloor morphologies in the northern part of the depression may be caused by the outflows of fresh asphalt below the older surficial deposits. Instead of forming the main asphalt flow structures like at the Chapopote Knoll, numerous smaller scales of fresh asphalt and oil seeps were observed in the extensive asphalt deposits area at the Mictlan Knoll. This indicates that the younger flows did not break through the older deposits sufficiently to cover them up. The gas emission sites were generally located at the rim of the crater-like depression. This finding further supports the conceptual model of the first manuscript. No gas emission sites are located within the area of extensive asphalt deposits, and this may be due to the asphalt deposits in the subsurface that formed an effective seal preventing vertical gas migration. The distributions and seafloor manifestations of diverse hydrocarbon seepage enhanced the understanding of asphalt volcanism in the southern GoM.

Overall, the findings and the results presented in this work are not only restricted to the southern GoM but also provide a deeper insight into the knowledge of various hydrocarbon seepage systems and their interaction with salt tectonism. The occurrence of hydrocarbon seepage in the Campeche-Sigsbee salt province is highly controlled by the geological and

morphological settings. This phenomenon has also been reported in many other regions. The conceptual models proposed in this study will be of broad use to the understanding of hydrocarbon migration associated with salt tectonism. Detailed seafloor mapping integrated with visual seafloor observation thoroughly examine the occurrences and the extent of hydrocarbon seeps at Mictlan Knoll. These findings contribute to existing knowledge of submarine asphalt deposits by providing a detailed investigation of diverse hydrocarbon seepage at Mictlan Knoll where different asphalt facies were documented. However, this work has thrown up many questions in need of further investigation. Further seismic studies could be conducted to determine the subsurface structures and to fully understand the implications of geological control on the occurrences of hydrocarbon seepage. Moreover, additional drilling-based research should be carried out to establish the sequence, thickness, and nature of asphalt deposits.

## References:

Aharon P (1994) Geology and Biology of Modern and Ancient Submarine Hydrocarbon Seeps and Vents - an Introduction. Geo-Marine Letters 14:69-73. https://doi:10.1007/Bf01203716.

Aharon P, Fu BS (2000) Microbial sulfate reduction rates and sulfur and oxygen isotope fractionations at oil and gas seeps in deepwater Gulf of Mexico. Geochim Cosmochim Ac 64:233-246. https://doi:10.1016/S0016-7037(99)00292-6.

Allen AA, Schlueter RS, Mikolaj PG (1970) Natural oil seepage at coal oil point, santa barbara, california. Science 170:974-977. https://doi:10.1126/science.170.3961.974.

Andreassen K et al. (2017) Massive blow-out craters formed by hydrate-controlled methane expulsion from the Arctic seafloor. Science 356:948-952. https://doi:10.1126/science.aal4500.

Andresen KJ (2012) Fluid flow features in hydrocarbon plumbing systems: What do they tell us about the basin evolution? Mar Geol 332:89-108. https://doi:10.1016/j.margeo.2012.07.006.

Andresen KJ, Huuse M, Schødt NH, Clausen LF, Seidler L (2011) Hydrocarbon plumbing systems of salt minibasins offshore Angola revealed by three-dimensional seismic analysis. AAPG bulletin 95:1039-1065. https://doi:10.1306/12131010046.

Angeles-Aquino F, Reyes-Nunez J, Quezada-Muneton J, Meneses-Rocha J (1994) Tectonic evolution, structural styles, and oil habitat in Campeche sound, Mexico. Transactions of the Gulf Association of Geological Societies 44:53-62.

Augustin JM, LeSuave R, Lurton X, Voisset M, Dugelay S, Satra C (1996) Contribution of the multibeam acoustic imagery to the exploration of the sea-bottom. Marine Geophysical Researches 18:459-486. https://doi:10.1007/Bf00286090.

Bergquist DC, Williams FM, Fisher CR (2000) Longevity record for deep-sea invertebrate. Nature 403:499. https://doi:10.1038/35000647.

Bernard BB, Brooks JM, Sackett WM (1976) Natural gas seepage in the Gulf of Mexico. Earth and Planetary Science Letters 31:48-54. https://doi:10.1016/0012-821X(76)90095-9.

Berndt C (2005) Focused fluid flow in passive continental margins. Philos Trans A Math Phys Eng Sci 363:2855-2871. https://doi:10.1098/rsta.2005.1666.

Berndt C, Mienert J, Vanneste M, Bünz S (2005) Gas hydrate dissociation and sea-floor collapse in the wake of the Storegga Slide, Norway. In: Norwegian Petroleum Society Special Publications, vol 12. pp 285-292, Elsevier. https://doi:10.1016/S0928-8937(05)80055-4.

Bird DE, Burke K, Hall SA, Casey JF (2005) Gulf of Mexico tectonic history: Hotspot tracks, crustal boundaries, and early salt distribution. AAPG bulletin 89:311-328. https://doi:10.1306/10280404026.

BOEM (2018) BOEM Northern Gulf of Mexico Deepwater Bathymetry Grid from 3D Seismic. https://www.boem.gov/Gulf-of-Mexico-Deepwater-Bathymetry/.

Boetius A (2005) Microfauna–macrofauna interaction in the seafloor: lessons from the tubeworm. PLOS biology 3:e102. https://doi:10.1371/journal.pbio.0030102.

Bohrmann G et al. (2011) Report and preliminary results of RV Maria S. Merian cruise MSM 15/2, Istanbul (Turkey)-Piraeus (Greece): 10 May-2 June 2010. Origin and structure of methane, gas hydrates and fluid flows in the Black Sea. Berichte aus dem Fachbereich Geowissenschaften der Universität Bremen, 278. Department of Geosciences, Bremen University.

Bohrmann G, Greinert J, Suess E, Torres M (1998) Authigenic carbonates from the Cascadia subduction zone and their relation to gas hydrate stability. Geology 26:647-650. https://doi:10.1130/0091-7613(1998)026<0647:Acftcs>2.3.Co;2.

Bohrmann G et al. (2003) Mud volcanoes and gas hydrates in the Black Sea: new data from Dvurechenskii and Odessa mud volcanoes. Geo-Marine Letters 23:239-249. https://doi:10.1007/s00367-003-0157-7.

Bohrmann G, Schenck S (2004) RV SONNE cruise report SO174, OTEGA II, Balboa− Corpus Christi− Miami (1 October− 12 November, 2003). GEOMAR report 117.

Bohrmann G et al. (2008) Report and preliminary results of R/V Meteor Cruise M67/2a and 2b, Balboa - Tampico - Bridgetwon, 15 March - 24 April, 2006. Fuid seepage in the Gulf of Mexico. Berichte aus dem Fachbereich Geowissenschaften der Universität Bremen, 263. Department of Geosciences, Bremen University.

Bohrmann G, Torres ME (2006) Gas hydrates in marine sediments. In: Marine Geochemistry. Schulz HD, Zabel M (eds), pp 481-512, Springer. https://doi:10.1007/3-540-32144-6_14.

Bowman SA (2011) Regional seismic interpretation of the hydrocarbon prospectivity of offshore Syria. GeoArabia 16:95-124.

Brekke C, Solberg AHS (2005) Oil spill detection by satellite remote sensing. Remote Sensing of Environment 95:1-13. https://doi:10.1016/j.rse.2004.11.015.

Brewer PG, Paull C, Peltzer ET, Ussler W, Rehder G, Friederich G (2002) Measurements of the fate of gas hydrates during transit through the ocean water column. Geophys Res Lett 29:38-31-38-34. https://doi:10.1029/2002gl014727.

Brown HE, Holbrook WS, Hornbach MJ, Nealon J (2006) Slide structure and role of gas hydrate at the northern boundary of the Storegga Slide, offshore Norway. Mar Geol 229:179-186. https://doi:10.1016/j.margeo.2006.03.011.

Brüning M, Sahling H, MacDonald IR, Ding F, Bohrmann G (2010) Origin, distribution, and alteration of asphalts at Chapopote Knoll, Southern Gulf of Mexico. Mar Petrol Geol 27:1093-1106. https://doi:10.1016/j.marpetgeo.2009.09.005.

Bryant WR, Lugo J, Cordova C, Salvador A (1991) Physiography and bathymetry. The Gulf of Mexico Basin: Boulder, Geological Society of America, Decade of North American Geology, v J:13-30.

Buerk D, Klaucke I, Sahling H, Weinrebe W (2010) Morpho-acoustic variability of cold seeps on the continental slope offshore Nicaragua: Result of fluid flow interaction with sedimentary processes. Mar Geol 275:53-65. https://doi:10.1016/j.margeo.2010.04.007.

Bünz S, Polyanov S, Vadakkepuliyambatta S, Consolaro C, Mienert J (2012) Active gas venting through hydrate-bearing sediments on the Vestnesa Ridge, offshore W-Svalbard. Mar Geol 332–334:189-197. https://doi:http://dx.doi.org/10.1016/j.margeo.2012.09.012.

Caress DW, Cheyes DN (2017) MB-System: Mapping the Seafloor. https://www.mbari.org/products/research-software/mb-system.

Cartwright J, Huuse M, Aplin A (2007) Seal bypass systems. AAPG bulletin 91:1141-1166. https://doi:10.1306/04090705181.

Claypool GE, Kaplan IR (1974) The origin and distribution of methane in marine sediments. In: Natural gases in marine sediments. Kaplan IR (ed), pp 99-139, Springer, Boston, MA. https://doi:10.1007/978-1-4684-2757-8_8.

Claypool GE, Kvenvolden KA (1983) Methane and Other Hydrocarbon Gases in Marine Sediment. Annual Review of Earth and Planetary Sciences 11:299-327. https://doi:10.1146/annurev.ea.11.050183.001503.

Clennell MB, Judd A, Hovland M (2000) Movement and accumulation of methane in marine sediments: Relation to gas hydrate systems. In: Natural Gas Hydrate. pp 105-122, Springer. https://doi:10.1007/978-94-011-4387-5_9.

Colbo K, Ross T, Brown C, Weber T (2014) A review of oceanographic applications of water column data from multibeam echosounders. Estuarine, Coastal and Shelf Science 145:41-56. https://doi:10.1016/j.ecss.2014.04.002.

Collet JF, Bardwell JC (2002) Oxidative protein folding in bacteria. Molecular microbiology 44:1-8. https://doi:10.1046/j.1365-2958.2002.02851.x.

Cook J (2014) Natural Oil Seeps. Woods Hole Oceanographic Institution, https://www.whoi.edu/multimedia/natural-oil-seeps/.

Cordes EE, Bergquist DC, Fisher CR (2009) Macro-ecology of Gulf of Mexico cold seeps. Annual Review of Marine Science 1:143-168. https://doi:10.1146/annurev.marine.010908.163912.

Cordes EE et al. (2010) The influence of geological, geochemical, and biogenic habitat heterogeneity on seep biodiversity. Marine Ecology 31:51-65. https://doi:10.1111/j.1439-0485.2009.00334.x.

Cruz-Mercado MÁ et al. (2011) Salt provinces in the Mexican portion of the Gulf of Mexico structural characterization and evolutionary model. Gulf Coast Association of Geological Societies Transactions 61:93–103.

Damuth JE (1980) Use of high-frequency (3.5–12 kHz) echograms in the study of near-bottom sedimentation processes in the deep-sea: a review. Mar Geol 38:51-75. https://doi:10.1016/0025-3227(80)90051-1.

Daneshgar Asl S, Dukhovskoy DS, Bourassa M, MacDonald IR (2017) Hindcast modeling of oil slick persistence from natural seeps. Remote sensing of environment 189:96-107. https://doi:10.1016/j.rse.2016.11.003.

De Beukelaer S, MacDonald I, Guinnasso Jr N, Murray J (2003) Distinct side-scan sonar, RADARSAT SAR, and acoustic profiler signatures of gas and oil seeps on the Gulf of Mexico slope. Geo-Marine Letters 23:177-186. https://doi:10.1007/s00367-003-0139-9.

Derkachev AN et al. (2015) Manifestation of carbonate-barite mineralization around methane seeps in the Sea of Okhotsk (the western slope of the Kuril Basin). Oceanology 55:390-399. https://doi:10.1134/S0001437015030029.

Didyk BM, Simoneit BR (1989) Hydrothermal oil of Guaymas Basin and implications for petroleum formation mechanisms. Nature 342:65. https://doi:10.1038/342065a0.

Dillon WP, Danforth W, Hutchinson D, Drury R, Taylor M, Booth J (1998) Evidence for faulting related to dissociation of gas hydrate and release of methane off the southeastern United States. Geological Society, London, Special Publications 137:293-302. https://doi:10.1144/GSL.SP.1998.137.01.23.

Dimitrov LI (2002) Mud volcanoes—the most important pathway for degassing deeply buried sediments. Earth-Science Reviews 59:49-76. https://doi:https://doi.org/10.1016/S0012-8252(02)00069-7.

Ding F, Spiess V, Brüning M, Fekete N, Keil H, Bohrmann G (2008) A conceptual model for hydrocarbon accumulation and seepage processes around Chapopote asphalt site, southern Gulf of Mexico: From high resolution seismic point of view. J Geophys Res-Sol Ea 113. https://doi:10.1029/2007jb005484.

Ding F, Spiess V, MacDonald IR, Brüning M, Fekete N, Bohrmann G (2010) Shallow sediment deformation styles in north-western Campeche Knolls, Gulf of Mexico and their controls on the occurrence of hydrocarbon seepage. Mar Petrol Geol 27:959-972. https://doi:10.1016/j.marpetgeo.2010.01.014.

Dissanayake AL, Gros J, Socolofsky SA (2018) Integral models for bubble, droplet, and multiphase plume dynamics in stratification and crossflow. Environmental Fluid Mechanics. https://doi:10.1007/s10652-018-9591-y.

Dupré S et al. (2008) High-resolution mapping of large gas emitting mud volcanoes on the Egyptian continental margin (Nile Deep Sea Fan) by AUV surveys. Marine Geophysical Researches 29:275-290. https://doi:10.1007/s11001-009-9063-3.

Dupré S et al. (2015) Tectonic and sedimentary controls on widespread gas emissions in the Sea of Marmara: Results from systematic, shipborne multibeam echo sounder water column imaging. Journal of Geophysical Research: Solid Earth 120:2891-2912. https://doi:10.1002/2014JB011617.

Eichhubl P, Greene HG, Maher N (2002) Physiography of an active transpressive margin basin: high-resolution bathymetry of the Santa Barbara basin, Southern California continental borderland. Mar Geol 184:95-120. https://doi:10.1016/S0025-3227(01)00280-8.

Ewing JI, Worzel JL, Ewing M (1962) Sediments and oceanic structural history of the Gulf of Mexico. Journal of Geophysical Research 67:2509-2527. https://doi:10.1029/JZ067i006p02509.

Ewing M, Ericson DB, Heezen BC (1958) Sediments and Topography of the Gulf of Mexico: Typical Modern Basins. AAPG Special Volumes SP 18: Habitat of Oil:995-1053.

Ewing M et al. (1969a) Site 2. Initial reports of the Deep Sea Drilling Project 1:84-111. https://doi:10.2973/dsdp.proc.1.102.1969.

Ewing M et al. (1969b) Site 3. Initial reports of the Deep Sea Drilling Project 1:112-178. https://doi:10.2973/dsdp.proc.1.103.1969.

Ewing M, Worzel JL, Burk CA (1969c) Introduction. Initial Reports of the Deep Sea Drilling Project 1:3-9. https://doi:10.2973/dsdp.proc.1.intro.1969.

Fisher CR, Urcuyo IA, Simpkins MA, NIx E (1997) Life in the Slow Lane: Growth and Longevity of Cold-seep Vestimentiferans. Marine Ecology 18:83-94. https://doi:10.1111/j.1439-0485.1997.tb00428.x.

Fleischer P, Orsi T, Richardson M, Anderson A (2001) Distribution of free gas in marine sediments: a global overview. Geo-Marine Letters 21:103-122. https://doi:10.1007/s003670100072.

Floodgate GD, Judd AG (1992) The Origins of Shallow Gas. Cont Shelf Res 12:1145-1156. https://doi:10.1016/0278-4343(92)90075-U.

Forwick M, Baeten NJ, Vorren TO (2009) Pockmarks in Spitsbergen fjords. Norwegian Journal of Geology 89:65-77.

Fujikura K et al. (2017) Discovery of asphalt seeps in the deep Southwest Atlantic off Brazil. Deep Sea Research Part II: Topical Studies in Oceanography 146:35-44. https://doi:10.1016/j.dsr2.2017.04.002.

Galimov EM (1988) Sources and Mechanisms of Formation of Gaseous Hydrocarbons in Sedimentary-Rocks. Chemical Geology 71:77-95. https://doi:10.1016/0009-2541(88)90107-6.

Garcia-Pineda O, MacDonald I, Zimmer B, Shedd B, Roberts H (2010) Remote-sensing evaluation of geophysical anomaly sites in the outer continental slope, northern Gulf of Mexico. Deep-Sea Res Pt Ii 57:1859-1869. https://doi:10.1016/j.dsr2.2010.05.005.

Garrison LE, Martin RG (1973) Geologic structures in the Gulf of Mexico basin. vol 773. US Government Printing Office, Washington. https://doi:10.3133/pp773.

Gaullier V, Bellaiche G (1998) Near-bottom sedimentation processes revealed by echo-character mapping studies, northwestern Mediterranean basin. AAPG bulletin 82:1140-1155.

Gay A, Lopez M, Berndt C, Seranne M (2007) Geological controls on focused fluid flow associated with seafloor seeps in the Lower Congo Basin. Mar Geol 244:68-92. https://doi:10.1016/j.margeo.2007.06.003.

Gay A, Lopez M, Cochonat P, Sermondadaz G (2004) Polygonal faults-furrows system related to early stages of compaction – upper Miocene to recent sediments of the

Lower Congo Basin. Basin Research 16:101-116. https://doi:10.1111/j.1365-2117.2003.00224.x.

Gontz AM, Belknap DF, Kelley JT (2002) Seafloor features and characteristics of the Black Ledges area, Penobscot Bay, Maine, USA. Journal of Coastal Research 36:333-339. https://doi:10.2112/1551-5036-36.sp1.333.

Graue K (2000) Mud volcanoes in deepwater Nigeria. Mar Petrol Geol 17:959-974. https://doi:10.1016/S0264-8172(00)00016-7.

Greinert J, Artemov Y, Egorov V, De Batist M, McGinnis D (2006) 1300-m-high rising bubbles from mud volcanoes at 2080m in the Black Sea: Hydroacoustic characteristics and temporal variability. Earth and Planetary Science Letters 244:1-15. https://doi:10.1016/j.epsl.2006.02.01.

Greinert J, Klaucke I, Gimpel P Side-scan sonar investigations and hydroacoustic 'bubble' quantification in an area of surface-near gas hydrate occurrences: recent studies from Hydrate Ridge, offshore Oregon. In: OCEANS '02 MTS/IEEE, 29-31 Oct. 2002 2002. pp 1143-1147 vol.1142. https://doi:10.1109/OCEANS.2002.1192127

Gros J, Reddy CM, Nelson RK, Socolofsky SA, Arey JS (2016) Simulating Gas–Liquid−Water Partitioning and Fluid Properties of Petroleum under Pressure: Implications for Deep-Sea Blowouts. Environmental Science & Technology 50:7397-7408. https://doi:10.1021/acs.est.5b04617.

Gros J et al. (2017) Petroleum dynamics in the sea and influence of subsea dispersant injection during Deepwater Horizon. Proc Natl Acad Sci U S A 114:10065-10070. https://doi:10.1073/pnas.1612518114.

Haffert L et al. (2013) Fluid evolution and authigenic mineral paragenesis related to salt diapirism – The Mercator mud volcano in the Gulf of Cadiz. Geochim Cosmochim Ac 106:261-286. https://doi:10.1016/j.gca.2012.12.016.

Harding TP, Lowell JD (1979) Structural styles, their plate-tectonic habitats, and hydrocarbon traps in petroleum provinces. AAPG bulletin 63:1016-1058.

Heeschen KU, Trehu AM, Collier RW, Suess E, Rehder G (2003) Distribution and height of methane bubble plumes on the Cascadia Margin characterized by acoustic imaging. Geophys Res Lett 30. https://doi:10.1029/2003gl016974.

Hensen C et al. (2015) Strike-slip faults mediate the rise of crustal-derived fluids and mud volcanism in the deep sea. Geology 43:339-342. https://doi:10.1130/G36359.1.

Hood KC, Wenger L, Gross O, Harrison S (2002) Hydrocarbon systems analysis of the northern Gulf of Mexico: Delineation of hydrocarbon migration pathways using seeps and seismic imaging. Surface exploration case histories: Applications of geochemistry, magnetics, and remote sensing: AAPG Studies in Geology 48:25-40

Hornafius JS, Quigley D, Luyendyk BP (1999) The world's most spectacular marine hydrocarbon seeps (Coal Oil Point, Santa Barbara Channel, California): Quantification of emissions. J Geophys Res-Oceans 104:20703-20711. https://doi:10.1029/1999jc900148.

Hovland M, Gardner JV, Judd A (2002) The significance of pockmarks to understanding fluid flow processes and geohazards. Geofluids 2:127-136. https://doi:10.1046/j.1468-8123.2002.00028.x.

Hovland M, Judd A (1988) Seabed pockmarks and seepages: Impact on geology, biology and the marine environment. Graham & Trotman Ltd., London.

Hovland M, Judd AG, Burke RA (1993) The Global Flux of Methane from Shallow Submarine Sediments. Chemosphere 26:559-578. https://doi:10.1016/0045-6535(93)90442-8.

Hovland M, Judd AG, King LH (1984) Characteristic features of pockmarks on the North Sea Floor and Scotian Shelf. Sedimentology 31:471-480. https://doi:10.1111/j.1365-3091.1984.tb01813.x.

Hovland M, Svensen H (2006) Submarine pingoes: Indicators of shallow gas hydrates in a pockmark at Nyegga, Norwegian Sea. Mar Geol 228:15-23. https://doi:10.1016/j.margeo.2005.12.005.

Hovland M, Talbot MR, Qvale H, Olaussen S, Aasberg L (1987) Methane-Related Carbonate Cements in Pockmarks of the North-Sea. J Sediment Petrol 57:881-892. https://doi:10.1306/212F8C92-2B24-11D7-8648000102C1865D.

Hsu C-W, MacDonald IR, Römer M, Pape T, Sahling H, Wintersteller P, Bohrmann G (2019) Characteristics and hydrocarbon seepage at the Challenger Knoll in the Sigsbee Basin, Gulf of Mexico. Geo-Marine Letters 39:391-399. https://doi:10.1007/s00367-019-00595-x.

Hsu SK, Wang SY, Liao YC, Yang TYF, Jan S, Lin JY, Chen SC (2013) Tide-modulated gas emissions and tremors off SW Taiwan. Earth and Planetary Science Letters 369:98-107. https://doi:10.1016/j.epsl.2013.03.013.

Hudec MR, Jackson MPA (2007) Terra infirma: Understanding salt tectonics. Earth-Science Reviews 82:1-28. https://doi:10.1016/j.earscirev.2007.01.001.

IPCC (2013) Climate Change 2013: The Physical Science Basis. Contribution of Working Group I to the Fifth Assessment Report of the Intergovern- mental Panel on Climate Change, Technical Summary, edited by T. F. Stocker et al., pp. 33–118, Cambridge Univ. Press, Cambridge, U. K.

Ivanov A, Gobulov B, Zatyagalova B (2007) On Oil and Gas Seeps and Underground Fluid Discharges in the Southern Caspian Based on Space Radar Data. Earth Exploration from Space 2:62-81.

Jackson MPA, Talbot CJ (1986) External Shapes, Strain Rates, and Dynamics of Salt Structures. Geological Society of America Bulletin 97:305-323. https://doi:10.1130/0016-7606(1986)97<305:Essrad>2.0.Co;2.

Jatiault R, Dhont D, Loncke L, Dubucq D (2017) Monitoring of natural oil seepage in the Lower Congo Basin using SAR observations. Remote Sensing of Environment 191:258-272. https://doi:10.1016/j.rse.2017.01.031.

Johansen C, Todd AC, MacDonald IR (2017) Time series video analysis of bubble release processes at natural hydrocarbon seeps in the Northern Gulf of Mexico. Mar Petrol Geol 82:21-34. https://doi:10.1016/j.marpetgeo.2017.01.014.

Jones DOB, Walls A, Clare M, Fiske MS, Weiland RJ, O'Brien R, Touzel DF (2014) Asphalt mounds and associated biota on the Angolan margin. Deep-Sea Res Pt I 94:124-136. https://doi:10.1016/j.dsr.2014.08.010.

Judd A, Hovland M (2009) Seabed fluid flow: the impact on geology, biology and the marine environment. Cambridge University Press.

Judd AG, Hovland M (1992) The evidence of shallow gas in marine sediments. Cont Shelf Res 12:1081-1095. https://doi:10.1016/0278-4343(92)90070-Z.

Keller EA, Duffy M, Kennett JP, Hill T (2007) Tectonic geomorphology and hydrocarbon induced topography of the mid-Channel Anticline, Santa Barbara Basin, California. Geomorphology 89:274-286. https://doi:10.1016/j.geomorph.2006.12.006.

Kennicutt II MC, Brooks JM, Denoux GJ (1988) Leakage of deep, reservoired petroleum to the near surface on the Gulf of Mexico continental slope. Marine Chemistry 24:39-59. https://doi:10.1016/0304-4203(88)90005-9.

Khilyuk LF, Robertson Jr JO, Endres B, Chilingarian G (2000) Gas migration: events preceding earthquakes. Gulf Publishing Company, Houston, Texas.

King LH, MacLean B (1970) Pockmarks on the Scotian shelf. Geological Society of America Bulletin 81:3141-3148.

Klapp SA, Murshed MM, Pape T, Klein H, Bohrmann G, Brewer PG, Kuhs WF (2010) Mixed gas hydrate structures at the Chapopote Knoll, southern Gulf of Mexico. Earth and Planetary Science Letters 299:207-217. https://doi:10.1016/j.epsl.2010.09.001.

Kleinberg R, Flaum C, Griffin D, Brewer P, Malby G, Peltzer E, Yesinowski J (2003) Deep sea NMR: Methane hydrate growth habit in porous media and its relationship to hydraulic permeability, deposit accumulation, and submarine slope stability. Journal of Geophysical Research: Solid Earth 108. https://doi:10.1029/2003JB002389.

Koch S et al. (2015) Gas-controlled seafloor doming. Geology 43:571-574. https://doi:10.1130/G36596.1.

Kopf AJ (2002) Significance of mud volcanism. Rev Geophys 40:2-1-2-52. https://doi:10.1029/2000rg000093.

Körber J-H, Sahling H, Pape T, dos Santos Ferreira C, MacDonald I, Bohrmann G (2014) Natural oil seepage at kobuleti ridge, eastern Black Sea. Mar Petrol Geol 50:68-82. https://doi:10.1016/j.marpetgeo.2013.11.007.

Kvenvolden K (1998) A primer on the geological occurrence of gas hydrate. Geological Society, London, Special Publications 137:9-30. https://doi:doi.org/10.1144/GSL.SP.1998.137.01.02.

Kvenvolden KA (1988) Methane hydrate—a major reservoir of carbon in the shallow geosphere? Chemical geology 71:41-51. https://doi:10.1016/0009-2541(88)90104-0.

Kvenvolden KA (1993) Gas Hydrates - Geological Perspective and Global Change. Rev Geophys 31:173-187. https://doi:10.1029/93rg00268.

Kvenvolden KA, Cooper CK (2003) Natural seepage of crude oil into the marine environment. Geo-Marine Letters 23:140-146. https://doi:10.1007/s00367-003-0135-0.

Kvenvolden KA, McMenamin MA (1980) Hydrates of natural gas: a review of their geologic occurrence. vol 825. U.S. Geol. Surv. Circular.

Kvenvolden KA, Rogers BW (2005) Gaia's breath - global methane exhalations. Mar Petrol Geol 22:579-590. https://doi:10.1016/j.marpetgeo.2004.08.004.

Ladd JW, Buffler RT, Watkins JS, Worzel JL, Carranza A (1976) Deep seismic reflection results from the Gulf of Mexico. Geology 4:365-368. https://doi:10.1130/0091-7613(1976)4<365:DSRRFT>2.0.CO;2.

Le Pichon X, Kobayashi K, Crew K-NS (1992) Fluid venting activity within the eastern Nankai Trough accretionary wedge: A summary of the 1989 Kaiko-Nankai results. Earth and Planetary Science Letters 109:303-318. https://doi:10.1016/0012-821X(92)90094-C.

Leifer I (2010) Characteristics and scaling of bubble plumes from marine hydrocarbon seepage in the Coal Oil Point seep field. J Geophys Res-Oceans 115. https://doi:10.1029/2009jc005844.

Leifer I (2015) Seabed bubble flux estimation by calibrated video survey for a large blowout seep in the North Sea. Mar Petrol Geol 68:743-752. https://doi:10.1016/j.marpetgeo.2015.08.032.

Leifer I, MacDonald I (2003) Dynamics of the gas flux from shallow gas hydrate deposits: interaction between oily hydrate bubbles and the oceanic environment. Earth and Planetary Science Letters 210:411-424. https://doi:10.1016/S0012-821x(03)00173-0.

Leifer I, Patro RK (2002) The bubble mechanism for methane transport from the shallow sea bed to the surface: A review and sensitivity study. Cont Shelf Res 22:2409-2428. https://doi:10.1016/S0278-4343(02)00065-1.

Loher M, Ceramicola S, Wintersteller P, Meinecke G, Sahling H, Bohrmann G (2018a) Mud volcanism in a canyon: Morphodynamic evolution of the active Venere mud volcano and its interplay with Squillace Canyon, Central Mediterranean. Geochemistry, Geophysics, Geosystems 19:356-378. https://doi:10.1002/2017GC007166.

Loher M et al. (2018b) Seafloor sealing, doming, and collapse associated with gas seeps and authigenic carbonate structures at Venere mud volcano, Central Mediterranean. Deep-Sea Res Pt I 137:76-96. https://doi:10.1016/j.dsr.2018.04.006.

Loher M et al. (2018c) Mud extrusion and ring-fault gas seepage – upward branching fluid discharge at a deep-sea mud volcano. Scientific Reports 8:6275. https://doi:10.1038/s41598-018-24689-1.

Loncke L, Gaullier V, Bellaiche G, Mascle J (2002) Recent depositional patterns of the Nile deep-sea fan from echo-character mapping. AAPG bulletin 86:1165-1186.

Lurton X, Lamarche G (2015) Backscatter measurements by seafloor-mapping sonars. Guidelines and recommendations. http://geohab.org/wp-content/uploads/2014/05/BSWGREPORT-MAY2015.pdf

MacDonald IR et al. (2004) Asphalt volcanism and chemosynthetic life in the Campeche Knolls, Gulf of Mexico. Science 304:999-1002. https://doi:10.1126/science.1097154.

MacDonald IR et al. (2015) Natural and unnatural oil slicks in the Gulf of Mexico. J Geophys Res Oceans 120:8364-8380. https://doi:10.1002/2015JC011062.

Macdonald IR, Guinasso NL, Ackleson SG, Amos JF, Duckworth R, Sassen R, Brooks JM (1993) Natural Oil-Slicks in the Gulf-of-Mexico Visible from Space. J Geophys Res-Oceans 98:16351-16364. https://doi:10.1029/93jc01289.

MacDonald IR, Leifer I, Sassen R, Stine P, Mitchell R, Guinasso N (2002) Transfer of hydrocarbons from natural seeps to the water column and atmosphere. Geofluids 2:95-107. https://doi:10.1046/j.1468-8123.2002.00023.x.

Macdonald IR, Reilly JF, Guinasso NL, Brooks JM, Carney RS, Bryant WA, Bright TJ (1990) Chemosynthetic Mussels at a Brine-Filled Pockmark in the Northern Gulf of Mexico. Science 248:1096-1099. https://doi:10.1126/science.248.4959.1096.

MacDonald IR, Sager WW, Peccini MB (2003) Gas hydrate and chemosynthetic biota in mounded bathymetry at mid-slope hydrocarbon seeps: Northern Gulf of Mexico. Mar Geol 198:133-158. https://doi:10.1016/S0025-3227(03)00098-7.

Magoon LB, Hudson TL, Cook HE (2001) Pimienta-Tamabra (!)--A Giant Supercharged Petroleum System in the Southern Gulf of Mexico, Onshore and Offshore Mexico. In: The Western Gulf of Mexico Basin: Tectonics, Sedimentary Basins, and Petroleum Systems, vol Memoir 75. Bartolini C, Buffler RT, Cantú-Chapa A (eds), pp 83-125, AAPG, Tulsa Oklahoma.

Makogon YF, Trebin F, Trofimuk A, Tsarev V, Cherskii N Detection of natural gas deposits in solid (gas hydrate) state. In: Dokl. Akad. Nauk SSSR, 1971. vol 203. p l97l.

Marcon Y LAPMv2: An improved tool for underwater large-area photo-mosaicking. In: 2014 Oceans-St. John's, 2014. IEEE, pp 1-10. https://doi:10.1109/OCEANS.2014.7003185

Marcon Y (2019) NavCleaner for processing USBL, DVL and hybrid dive tracks. https://doi:10.1594/PANGAEA.905245.

Marcon Y, Ondréas H, Sahling H, Bohrmann G, Olu K (2014) Fluid flow regimes and growth of a giant pockmark. Geology 42:63-66. https://doi:10.1130/G34801.1.

Marcon Y, Sahling H, Bohrmann G (2013) LAPM: a tool for underwater large-area photo-mosaicking. Geosci Instrum Meth 2:189-198. https://doi:10.5194/gi-2-189-2013.

Marcon Y, Sahling H, MacDonald IR, Wintersteller P, Ferreira CD, Bohrmann G (2018) SLOW VOLCANOES The Intriguing Similarities Between Marine Asphalt and Basalt Lavas. Oceanography 31:194-205. https://doi:10.5670/oceanog.2018.202.

Masoudi R, Tohidi B, Danesh A, Todd AC, Anderson R, Burgass RW, Yang JH (2005) Measurement and prediction of gas hydrate and hydrated salt equilibria in aqueous ethylene glycol and electrolyte solutions. Chemical Engineering Science 60:4213-4224. https://doi:10.1016/j.ces.2005.02.056.

Matthews MD (1996) Hydrocarbon migration-A view from the top. In: Hydrocarbon Migration and Its Near-Surface Expression, vol Memoir 66. Schumacher D, Abrams MA (eds), pp 139-155, Amer. Assoc. Petrol. Geol., Tulsa, Oklahoma.

Mau S et al. (2017) Widespread methane seepage along the continental margin off Svalbard - from Bjornoya to Kongsfjorden. Sci Rep 7:42997. https://doi:10.1038/srep42997.

Mau S, Valentine DL, Clark JF, Reed J, Camilli R, Washburn L (2007) Dissolved methane distributions and air-sea flux in the plume of a massive seep field, Coal Oil Point, California. Geophys Res Lett 34. https://doi:10.1029/2007GL031344.

Mayer LA (2006) Frontiers in seafloor mapping and visualization. Marine Geophysical Researches 27:7-17. https://doi:10.1007/s11001-005-0267-x.

Mazumdar A et al. (2009) Shallow gas charged sediments off the Indian west coast: Genesis and distribution. Mar Geol 267:71-85. https://doi:10.1016/j.margeo.2009.09.005.

Mazzini A, Etiope G (2017) Mud volcanism: An updated review. Earth-Science Reviews 168:81-112. https://doi:https://doi.org/10.1016/j.earscirev.2017.03.001.

Mazzini A, Svensen H, Planke S, Guliyev I, Akhmanov G, Fallik T, Banks D (2009) When mud volcanoes sleep: insight from seep geochemistry at the Dashgil mud volcano, Azerbaijan. Mar Petrol Geol 26:1704-1715. https://doi:10.1016/j.marpetgeo.2008.11.003.

McConnell DR, Kendall BA Images of the base of gas hydrate stability, Northwest Walker Ridge, Gulf of Mexico. In: Offshore Technology Conference, 2002. Offshore Technology Conference. https://doi:doi.org/10.4043/14103-MS

McGinnis DF, Greinert J, Artemov Y, Beaubien S, Wüest A (2006) Fate of rising methane bubbles in stratified waters: How much methane reaches the atmosphere? Journal of Geophysical Research: Oceans (1978–2012) 111. https://doi:10.1029/2005JC003183.

Medwin H (1970) In-Situ Acoustic Measurements of Bubble Populations in Coastal Ocean Waters. Journal of Geophysical Research 75:599-611. https://doi:10.1029/JC075i003p00599.

Medwin H, Clay C (1998) Fundamentals of Acoustical Oceanography Academic. New York.

Milkov A (2000) Worldwide distribution of submarine mud volcanoes and associated gas hydrates. Mar Geol 167:29-42. https://doi:10.1016/S0025-3227(00)00022-0.

Miller DJ et al. (2015) Natural gas hydrates in the Rio Grande Cone (Brazil): A new province in the western South Atlantic. Mar Petrol Geol 67:187-196. https://doi:10.1016/j.marpetgeo.2015.05.012.

Mitchell GA, Orange DL, Gharib JJ, Kennedy P (2018) Improved detection and mapping of deepwater hydrocarbon seeps: optimizing multibeam echosounder seafloor backscatter acquisition and processing techniques. Mar Geophys Res 39:323-347. https://doi:10.1007/s11001-018-9345-8.

Mitchell NC (1993) A model for attenuation of backscatter due to sediment accumulations and its application to determine sediment thicknesses with GLORIA sidescan sonar. Journal of Geophysical Research: Solid Earth 98:22477-22493. https://doi:10.1029/93jb02217.

Moore C (1999) Seeps give a peek into plumbing. Am Assoc Pet Geol Expl 99:22-23.

Moore JC, Orange D, Kulm LD (1990) Interrelationship of fluid venting and structural evolution: Alvin observations from the frontal accretionary prism, Oregon. Journal of

Geophysical Research: Solid Earth 95:8795-8808. https://doi:10.1029/JB095iB06p08795.

Moore JC, Vrolijk P (1992) Fluids in accretionary prisms. Rev Geophys 30:113-135. https://doi:10.1029/92RG00201.

Naehr TH, Birgel D, Bohrmann G, MacDonald IR, Kasten S (2009) Biogeochemical controls on authigenic carbonate formation at the Chapopote “asphalt volcano”, Bay of Campeche. Chemical Geology 266:390-402. https://doi:10.1016/j.chemgeo.2009.07.002.

NAS (2003) Oil in the sea III: inputs, fates, and effects. National Academy of Sciences, National Academy Press, Washington, DC.

Naudts L, Greinert J, Artemov Y, Beaubien SE, Borowski C, De Batist M (2008) Anomalous sea-floor backscatter patterns in methane venting areas, Dnepr paleo-delta, NW Black Sea. Mar Geol 251:253-267. https://doi:10.1016/j.margeo.2008.03.002.

Naudts L, Greinert J, Artemov Y, Staelens P, Poort J, Van Rensbergen P, De Batist M (2006) Geological and morphological setting of 2778 methane seeps in the Dnepr paleo-delta, northwestern Black Sea. Mar Geol 227:177-199. https://doi:10.1016/j.margeo.2005.10.005.

Nikolovska A, Sahling H, Bohrmann G (2008) Hydroacoustic methodology for detection, localization, and quantification of gas bubbles rising from the seafloor at gas seeps from the eastern Black Sea. Geochem Geophy Geosy 9. https://doi:10.1029/2008gc002118.

NOAA (2017) Active asphalt seep discovered in the Northern Gulf of Mexico. Okeanos Explorer, December 17. https://oceanexplorer.noaa.gov/okeanos/explorations/ex1711/logs/dec17/welcome.html.

Olu-Le Roy K et al. (2004) Cold seep communities in the deep eastern Mediterranean Sea: composition, symbiosis and spatial distribution on mud volcanoes. Deep Sea Research Part I: Oceanographic Research Papers 51:1915-1936. https://doi:10.1016/j.dsr.2004.07.004.

Orange DL, Breen NA (1992) The effects of fluid escape on accretionary wedges 2. Seepage force, slope failure, headless submarine canyons, and vents. Journal of Geophysical Research: Solid Earth 97:9277-9295. https://doi:10.1029/92JB00460.

Orange DL, Yun J, Maher N, Barry J, Greene G (2002) Tracking California seafloor seeps with bathymetry, backscatter and ROVs. Cont Shelf Res 22:2273-2290. https://doi:10.1016/S0278-4343(02)00054-7.

Panieri G et al. (2017) An integrated view of the methane system in the pockmarks at Vestnesa Ridge, 79°N. Mar Geol 390:282-300. https://doi:10.1016/j.margeo.2017.06.006.

Pape T, Bahr A, Klapp SA, Abegg F, Bohrmann G (2011) High-intensity gas seepage causes rafting of shallow gas hydrates in the southeastern Black Sea. Earth and Planetary Science Letters 307:35-46. https://doi:10.1016/j.epsl.2011.04.030.

Pape T et al. (2010) Molecular and isotopic partitioning of low-molecular-weight hydrocarbons during migration and gas hydrate precipitation in deposits of a high-flux seepage site. Chemical Geology 269:350-363. https://doi:10.1016/j.chemgeo.2009.10.009.

Paull C et al. (2015) Active mud volcanoes on the continental slope of the Canadian Beaufort Sea. Geochemistry, Geophysics, Geosystems 16:3160-3181. https://doi:10.1002/2015GC005928.

Paull CK et al. (1984) Biological Communities at the Florida Escarpment Resemble Hydrothermal Vent Taxa. Science 226:965-967. https://doi:10.1126/science.226.4677.965.

Paull CK, Normark WR, Ussler W, Caress DW, Keaten R (2008) Association among active seafloor deformation, mound formation, and gas hydrate growth and accumulation within the seafloor of the Santa Monica Basin, offshore California. Mar Geol 250:258-275. https://doi:https://doi.org/10.1016/j.margeo.2008.01.011.

Paull CK et al. (2007) Origin of pingo-like features on the Beaufort Sea shelf and their possible relationship to decomposing methane gas hydrates. Geophys Res Lett 34. https://doi:10.1029/2006GL027977.

Paull CK, Ussler W, Dillon WP (2000) Potential role of gas hydrate decomposition in generating submarine slope failures. In: Natural Gas Hydrate. pp 149-156, Springer. https://doi:10.1007/978-94-011-4387-5_12.

Pindell JL (1994) Evolution of the Gulf of Mexico and the Caribbean. In: Caribbean geology: an introduction. Donovan SK, Jackson TA (eds), pp 13-39, The University of the West Indies Publishers' Association, Jamaica.

Planke S, Svensen H, Hovland M, Banks D, Jamtveit B (2003) Mud and fluid migration in active mud volcanoes in Azerbaijan. Geo-Marine Letters 23:258-268. https://doi:10.1007/s00367-003-0152-z.

Praeg D, Ceramicola S, Barbieri R, Unnithan V, Wardell N (2009) Tectonically-driven mud volcanism since the late Pliocene on the Calabrian accretionary prism, central Mediterranean Sea. Mar Petrol Geol 26:1849-1865. https://doi:10.1016/j.marpetgeo.2009.03.008.

Prior DB, Doyle EH, Kaluza MJ (1989) Evidence for sediment eruption on deep sea floor, Gulf of Mexico. Science 243:517-519. https://doi:10.1126/science.243.4890.517.

Ranero CR et al. (2008) Hydrogeological system of erosional convergent margins and its influence on tectonics and interplate seismogenesis. Geochem Geophy Geosy 9. https://doi:10.1029/2007gc001679.

Rasband WS (1997-2016) ImageJ, U. S. National Institutes of Health, Bethesda, Maryland, USA, https://imagej.nih.gov/ij/.

Rehder G, Brewer PW, Peltzer ET, Friederich G (2002) Enhanced lifetime of methane bubble streams within the deep ocean. Geophys Res Lett 29. https://doi:10.1029/2001gl013966.

Rehder G, Leifer I, Brewer PG, Friederich G, Peltzer ET (2009) Controls on methane bubble dissolution inside and outside the hydrate stability field from open ocean field

experiments and numerical modeling. Marine Chemistry 114:19-30. https://doi:10.1016/j.marchem.2009.03.004.

Rice DD, Claypool GE (1981) Generation, accumulation, and resource potential of biogenic gas. AAPG Bulletin 65:5-25.

Roberts KS, Stewart SA, Davies RJ, Evans RJ (2011) Sector collapse of mud volcanoes, Azerbaijan. Journal of the Geological Society 168:49-60. https://doi:10.1144/0016-76492010-115.

Rogers JN, Kelley JT, Belknap DF, Gontz A, Barnhardt WA (2006) Shallow-water pockmark formation in temperate estuaries: a consideration of origins in the western gulf of Maine with special focus on Belfast Bay. Mar Geol 225:45-62. https://doi:10.1016/j.margeo.2005.07.011.

Römer M et al. (2019) Amount and Fate of Gas and Oil Discharged at 3400 m Water Depth From a Natural Seep Site in the Southern Gulf of Mexico. Frontiers in Marine Science 6. https://doi:10.3389/fmars.2019.00700.

Römer M, Riedel M, Scherwath M, Heesemann M, Spence GD (2016) Tidally controlled gas bubble emissions: A comprehensive study using long-term monitoring data from the NEPTUNE cabled observatory offshore Vancouver Island. Geochemistry, Geophysics, Geosystems 17:3797-3814. https://doi:10.1002/2016GC006528.

Römer M, Sahling H, Pape T, Bahr A, Feseker T, Wintersteller P, Bohrmann G (2012a) Geological control and magnitude of methane ebullition from a high-flux seep area in the Black Sea—the Kerch seep area. Mar Geol 319:57-74. https://doi:10.1016/j.margeo.2012.07.005.

Römer M, Sahling H, Pape T, Bohrmann G, Spieß V (2012b) Quantification of gas bubble emissions from submarine hydrocarbon seeps at the Makran continental margin (offshore Pakistan). Journal of Geophysical Research: Oceans (1978–2012) 117. https://doi:10.1029/2011jc007424.

Römer M, Sahling H, Pape T, dos Santos Ferreira C, Wenzhöfer F, Boetius A, Bohrmann G (2014a) Methane fluxes and carbonate deposits at a cold seep area of the Central Nile Deep Sea Fan, Eastern Mediterranean Sea. Mar Geol 347:27-42. https://doi:10.1016/j.margeo.2013.10.011.

Römer M et al. (2014b) First evidence of widespread active methane seepage in the Southern Ocean, off the sub-Antarctic island of South Georgia. Earth and Planetary Science Letters 403:166-177. https://doi:10.1016/j.epsl.2014.06.036.

Rowan MG, Lawton TF, Giles KA, Ratliff RA (2003) Near-salt deformation in La Popa basin, Mexico, and the northern Gulf of Mexico: A general model for passive diapirism. AAPG bulletin 87:733-756.

Roy S, Senger K, Noormets R, Hovland M (2012) Pockmarks in the fjords of western Svalbard and their implications on gas hydrate dissociation. EGU General Assembly Conference Abstracts 14:8960-8960.

Rubin-Blum M et al. (2017) Short-chain alkanes fuel mussel and sponge Cycloclasticus symbionts from deep-sea gas and oil seeps. Nat Microbiol 2:17093. https://doi:10.1038/nmicrobiol.2017.93.

Ryu B-J, Riedel M, Kim J-H, Hyndman RD, Lee Y-J, Chung B-H, Kim I-S (2009) Gas hydrates in the western deep-water Ulleung Basin, East Sea of Korea. Mar Petrol Geol 26:1483-1498. https://doi:10.1016/j.marpetgeo.2009.02.004.

Sahling H et al. (2017) R/V METEOR Cruise Report M114, Natural hydrocarbon seepage in the southern Gulf of Mexico, Kingston - Kingston, 12 February - 28 March 2015 vol 315. Berichte, MARUM – Zentrum für Marine Umweltwissenschaften, Fachbereich Geowissenschaften, Universität Bremen.

Sahling H et al. (2009) Vodyanitskii mud volcano, Sorokin trough, Black Sea: Geological characterization and quantification of gas bubble streams. Mar Petrol Geol 26:1799-1811. https://doi:10.1016/j.marpetgeo.2009.01.010.

Sahling H et al. (2008a) Pockmarks in the Northern Congo Fan area, SW Africa: Complex seafloor features shaped by fluid flow. Mar Geol 249:206-225. https://doi:10.1016/j.margeo.2007.11.010.

Sahling H et al. (2016) Massive asphalt deposits, oil seepage, and gas venting support abundant chemosynthetic communities at the Campeche Knolls, southern Gulf of Mexico. Biogeosciences 13:4491-4512. https://doi:10.5194/bg-13-4491-2016.

Sahling H et al. (2008b) Fluid seepage at the continental margin offshore Costa Rica and southern Nicaragua. Geochem Geophy Geosy 9. https://doi:10.1029/2008gc001978.

Sahling H, Rickert D, Lee RW, Linke P, Suess E (2002) Macrofaunal community structure and sulfide flux at gas hydrate deposits from the Cascadia convergent margin, NE Pacific. Marine Ecology Progress Series 231:121-138. https://doi:10.3354/meps231121.

Sahling H et al. (2014) Gas emissions at the continental margin west of Svalbard: mapping, sampling, and quantification. Biogeosciences 11:6029-6046. https://doi:10.5194/bg-11-6029-2014.

Salvador A (1991a) Origin and development of the Gulf of Mexico basin. In: The Gulf of Mexico Basin. pp 389-444, Geological Society of America, Washington, DC.

Salvador A (1991b) Triassic-Jurassic. In: The Gulf of Mexico Basin. pp 131-180, Geological Society of America, Washington, DC.

Sánchez-Rivera RS et al. (2011) Tectonic evolution of the South Gulf Salt Province in the Gulf of Mexico. Gulf Coast Association of Geological Societies Transactions 61:421-427.

Sauter EJ et al. (2006) Methane discharge from a deep-sea submarine mud volcano into the upper water column by gas hydrate-coated methane bubbles. Earth and Planetary Science Letters 243:354-365. https://doi:10.1016/j.epsl.2006.01.041.

Schmale O, Greinert J, Rehder G (2005) Methane emission from high-intensity marine gas seeps in the Black Sea into the atmosphere. Geophys Res Lett 32:n/a-n/a. https://doi:10.1029/2004GL021138.

Schmuck E, Paull C (1993) Evidence for gas accumulation associated with diapirism and gas hydrates at the head of the Cape Fear Slide. Geo-Marine Letters 13:145-152. https://doi:10.1007/BF01593187.

Schneider von Deimling J, Brockhoff J, Greinert J (2007) Flare imaging with multibeam systems: Data processing for bubble detection at seeps. Geochemistry, Geophysics, Geosystems 8. https://doi:10.1029/2007GC001577.

Schneider von Deimling J, Rehder G, Greinert J, McGinnnis DF, Boetius A, Linke P (2011) Quantification of seep-related methane gas emissions at Tommeliten, North Sea. Cont Shelf Res 31:867-878. https://doi:http://dx.doi.org/10.1016/j.csr.2011.02.012.

Schoell M (1988) Multiple Origins of Methane in the Earth. Chemical Geology 71:1-10. https://doi:10.1016/0009-2541(88)90101-5.

Schubotz F, Lipp JS, Elvert M, Hinrichs KU (2011a) Stable carbon isotopic compositions of intact polar lipids reveal complex carbon flow patterns among hydrocarbon degrading microbial communities at the Chapopote asphalt volcano. Geochim Cosmochim Ac 75:4399-4415. https://doi:10.1016/j.gca.2011.05.018.

Schubotz F et al. (2011b) Petroleum degradation and associated microbial signatures at the Chapopote asphalt volcano, Southern Gulf of Mexico. Geochim Cosmochim Ac 75:4377-4398. https://doi:10.1016/j.gca.2011.05.025.

Sen A, Ondréas H, Gaillot A, Marcon Y, Augustin J-M, Olu K (2016) The use of multibeam backscatter and bathymetry as a means of identifying faunal assemblages in a deep-sea cold seep. Deep Sea Research Part I: Oceanographic Research Papers 110:33-49. https://doi:10.1016/j.dsr.2016.01.005.

Serié C, Huuse M, Schodt NH (2012) Gas hydrate pingoes: Deep seafloor evidence of focused fluid flow on continental margins. Geology 40:207-210. https://doi:10.1130/G32690.1.

Shakhova N et al. (2015) The East Siberian Arctic Shelf: towards further assessment of permafrost-related methane fluxes and role of sea ice. Philos Trans A Math Phys Eng Sci 373:20140451. https://doi:10.1098/rsta.2014.0451.

Shaub FJ, Buffler RT, Parsons JG (1984) Seismic stratigraphic framework of deep central Gulf of Mexico Basin. AAPG Bulletin 68:1790-1802

Shipley T, Gahagan L, Johnson K, Davis M (2005) Seismic Data Center, University of Texas Institute for Geophysics. http://www.ig.utexas.edu/sdc/. Accessed October 23 2013

Skarke A, Ruppel C, Kodis M, Brothers D, Lobecker E (2014) Widespread methane leakage from the sea floor on the northern US Atlantic margin. Nat Geosci 7:657-661. https://doi:10.1038/Ngeo2232.

Sloan ED (1998) Gas hydrates: review of physical/chemical properties. Energ Fuel 12:191-196. https://doi:10.1021/ef970164+.

Solomon EA, Kastner M, MacDonald IR, Leifer I (2009) Considerable methane fluxes to the atmosphere from hydrocarbon seeps in the Gulf of Mexico. Nat Geosci 2:561-565. https://doi:10.1038/Ngeo574.

Stolper D et al. (2014) Formation temperatures of thermogenic and biogenic methane. Science 344:1500-1503. https://doi:10.1126/science.1254509.

Stolper DA et al. (2015) Distinguishing and understanding thermogenic and biogenic sources of methane using multiply substituted isotopologues. Geochim Cosmochim Ac 161:219-247. https://doi:10.1016/j.gca.2015.04.015.

Suess E (2014) Marine cold seeps and their manifestations: geological control, biogeochemical criteria and environmental conditions. International Journal of Earth Sciences 103:1889-1916. https://doi:10.1007/s00531-014-1010-0.

Suess E (2018) Marine Cold Seeps: Background and Recent Advances. Hydrocarbons, Oils and Lipids: Diversity, Origin, Chemistry and Fate:1-21. https://doi:10.1007/978-3-319-54529-5_27-1.

Suess E et al. (2001) Sea floor methane hydrates at Hydrate Ridge, Cascadia Margin. In: Natural Gas Hydrates: Occurrence, Distribution, and Detection, vol 124. Geophysical Monograph Series, Paull CK, Dillon WP (eds), pp 87-98, AGU, Washington, D. C. https://doi:10.1029/GM124p0087.

Sultan N et al. (2014) Pockmark formation and evolution in deep water Nigeria: Rapid hydrate growth versus slow hydrate dissolution. J Geophys Res-Sol Ea 119:2679-2694. https://doi:10.1002/2013jb010546.

Suresh G (2015) Offshore Oil Seepage Visible from Space: a Synthetic Aperture Radar (SAR) Based Automatic Detection, Mapping and Quantification System. Staats-und Universitätsbibliothek Bremen.

Torres ME et al. (2002) Fluid and chemical fluxes in and out of sediments hosting methane hydrate deposits on Hydrate Ridge, OR, I: Hydrological provinces. Earth and Planetary Science Letters 201:525-540. https://doi:10.1016/S0012-821x(02)00733-1.

Tóth Z, Spiess V, Keil H (2015) Frequency dependence in seismoacoustic imaging of shallow free gas due to gas bubble resonance. J Geophys Res-Sol Ea 120:8056-8072. https://doi:10.1002/2015jb012523.

Tryon MD, Brown KM, Torres ME (2002) Fluid and chemical flux in and out of sediments hosting methane hydrate deposits on Hydrate Ridge, OR, II: Hydrological processes. Earth and Planetary Science Letters 201:541-557. https://doi:https://doi.org/10.1016/S0012-821X(02)00732-X.

Ussler III W, Paull CK, Boucher J, Friederich G, Thomas D (2003) Submarine pockmarks: a case study from Belfast Bay, Maine. Mar Geol 202:175-192. https://doi:10.1016/S0025-3227(03)00261-5.

Valentine DL et al. (2010) Asphalt volcanoes as a potential source of methane to late Pleistocene coastal waters. Nat Geosci 3:345-348. https://doi:10.1038/Ngeo848.

Vernon JW, Slater RA (1963) Submarine Tar Mounds, Santa Barbara County, California: GEOLOGICAL NOTES. AAPG Bulletin 47:1624-1627.

Vis GJ (2017) Geology and seepage in the NE Atlantic region. Geol Soc Spec Publ 447:443-455. https://doi:10.1144/Sp447.16.

Wang BB, Socolofsky SA (2015) On the bubble rise velocity of a continually released bubble chain in still water and with crossflow. Phys Fluids 27:103301. https://doi:10.1063/1.4932176.

Wang BB, Socolofsky SA, Breier JA, Seewald JS (2016) Observations of bubbles in natural seep flares at MC 118 and GC 600 using in situ quantitative imaging. J Geophys Res-Oceans 121:2203-2230. https://doi:10.1002/2015jc011452.

Warren JK (2017) Salt usually seals, but sometimes leaks: Implications for mine and cavern stabilities in the short and long term. Earth-science reviews 165:302-341. https://doi:10.1016/j.earscirev.2016.11.008.

Weber TC, Mayer L, Jerram K, Beaudoin J, Rzhanov Y, Lovalvo D (2014) Acoustic estimates of methane gas flux from the seabed in a 6000 $km^2$ region in the Northern Gulf of Mexico. Geochemistry, Geophysics, Geosystems 15:1911-1925. https://doi:10.1002/2014gc005271.

Wei JG et al. (2015) Gas hydrate distributions in sediments of pockmarks from the Nigerian margin - Results and interpretation from shallow drilling. Mar Petrol Geol 59:359-370. https://doi:10.1016/j.marpetgeo.2014.09.013.

Weiland RJ, Adams GP, McDonald RD, Rooney TC, Wills LM Geological and biological relationships in the Puma appraisal area: from salt diapirism to chemosynthetic communities. In: Offshore Technology Conference, 2008.

White GW (1980) Permian-Triassic Continental Reconstruction of the Gulf of Mexico-Caribbean Area. Nature 283:823-826. https://doi:10.1038/283823a0.

Whiticar MJ (1999) Carbon and hydrogen isotope systematics of bacterial formation and oxidation of methane. Chemical Geology 161:291-314. https://doi:https://doi.org/10.1016/S0009-2541(99)00092-3.

Williams AK, Lawrence GM, King M (2006) Exploring for deepwater petroleum systems with satellite SAR (Synthetic Aperture RADAR). Fact or Fiction? Comparing results from two of today's hotspots (Congo and Santos) with two of tomorrow's (Campeche and Cariaco) (2 Poster), Adapted from poster presentation of the AAPG Annual Convention, Houston.

Williamson SC, Zois N, Hewitt AT Integrated site investigation of seafloor features and associated fauna, Shenzi Field, Deepwater Gulf of Mexico. In: Offshore Technology Conference, 2008.

Worzel JL et al. (1970) Site 88. Initial reports of the Deep Sea Drilling Project 10:55. https://doi:10.2973/dsdp.proc.10.105.1973.

Worzel JL, Leyden R, Ewing M (1968) Newly discovered diapirs in Gulf of Mexico. AAPG Bulletin 52:1194-1203.

Yefremova AG, Zhizchenko BP (1974) Occurrence of crystal hydrates of gases in the sediments of modern marine basins. Doklady Akademii Nauk SSSR 214:1179-1181.

## Acknowledgments

First of all, I would like to thank my adviser Prof. Dr. Gerhard Bohrmann for his support and encouragement, which determined me to go on with my Ph.D study in Germany. I am grateful for the opportunities you have provided to expand my vision of science. Furthermore, your academic achievement and the spirit of hard work are considered a model of excellence, for me to pursue. I would also like to express my gratitude to Dr. Heiko Sahling. You brought enlightenment to my journey of pursuing the Ph.D., and always guided me with patience and timely support when I met difficulties or felt frustrated. In addition, I would like to appreciate the inspiration and the kindly company from Dr. Miriam Römer, which have motivated me to finish this thesis. Thanks Dr. Thomas Pape for always carefully reading my manuscripts as well as offering suggestions which have improved the manuscripts significantly. I am grateful to Dr. Yann Marcon for his important contribution to the discussion about this thesis. Thanks to Dr. Ian MacDonald in the United States for providing critical insights into the Gulf of Mexico and a tremendous help in writing the manuscripts. Thanks to Paul Wintersteller, Christian dos Santos Ferreira for their enthusiastic and enduring support to seafloor mapping.

Thanks to all the people in Prof. Bohrmann's working group, because of you, I have a pleasant and full of laughter working environment. I want to thank my dear and excellent friend, Dr. Markus Loher, for being a companion to you, it is my honor and pride. Dr. Patrizia Geprägs, Dr. Susan Mau, Janice Malnati, Eberhard Kopiske, Tingting Wu, Jaingong Wei, Yi-Ting Tseng, Mechthild Doll, and Victoria Kürzinger thank you for sharing your time, knowledge, and experience with me during the cruise and in the office. Sincere thanks to Angelika Rinkel and Greta Ohling for always taking care of my family and me in many aspects.

Thanks to my former adviser Dr. Saulwood Lin for his support on my way to Ph.D., and encourage me from time to time, so that I could pass the challenge again and again, and have the motivation to move forward.

Thanks to the Lord, in the journey of my study over the past few years, all the environment is full of your goodwill. There are still many people to thank, and I cannot express my thanks to all of you in this short paragraph. I will go to you and express my gratitude to you, individually. Finally, this thesis is dedicated to my most beloved family, thank you for your support, in particular, the sacrifice of my wife, Jo-Yun Hsu.

# 論文致謝

首先我要感謝我指導教授 Prof. Dr. Gerhard Bohrmann 的支持以及鼓勵，使我能夠勇敢的來到德國追尋我的博士學位。感激你所提的機會使我擴大更寬且更深的科學視野，你的學術涵養以及勤奮的工作精神將成為我所追尋的標竿。我也要對 Dr. Heiko Sahling 至上我最高的謝意，你就像我的啟蒙老師般，細心地將我引入博士之路，並在我困難徬徨的時候不厭其煩地提供協助，你的門總是為我敞開。我要特別感謝 Dr. Miriam Römer 不吝嗇地分享你的想法並耐心的陪著我一同完成這篇論文。感謝 Dr. Thomas Pape 總是謹慎仔細的閱讀並給我的文章許多建議。非常感激 Dr. Yann Marcon 對論文討論提供了重要的貢獻。感謝遠在美國的 Dr. Ian MacDonald 提供了許多對於墨西哥灣的專家見解，並在文章的寫作上提供了許多的幫助。感谢 Paul Wintersteller, Christian dos Santos Ferreira 總是熱情地且持續地對 seafloor mapping 支持與幫助。

感謝所有在工作團隊的人，因為你們我們有一個愉悅且充滿歡笑的工作環境。我要感謝我親愛且優秀的朋友 Dr. Markus Loher，能成為與你的學習同伴，是我的榮幸與驕傲。Dr. Patrizia Geprägs, Dr. Susan Mau，Janice Malnati，Eberhard Kopiske, Tingting Wu, Jaingong Wei, Yi-Ting Tseng, Mechthild Doll 以及 Victoria Kürzinger 感謝你們在技術上，知識上，航次中以及實驗室中的貢獻，並且讓我總是在忙碌之餘有你們的歡笑點綴。誠摯的感謝 Angelika Rinkel 和 Greta Ohling，總是關心我的生活以及在各種生活瑣事上提供協助。

感謝我在台大的指導教授林曉武老師，在我追尋博士之路上的扶持，不時對我關心以及鼓勵，使我在困頓之時，有再次往前的動力。

感謝主，在我這幾年的學習旅程中一路的引領，所有的環境都滿了你的美意。要感謝的人還有很多，無法在這短短的篇幅裡道盡，我會親自向你們一一地道謝。最後，謹將此論文獻給我最摯愛的家人，感謝你們毫無怨尤的支持，以及我的妻子徐若芸的犧牲奉獻。

# Appendix

## A1. Cruise participation

The following gives an overview of all the cruises which I participated during the time of my PhD study.

| Date | Vessel/ cruise no. | Study area | Chief Scientists | Tasks |
|---|---|---|---|---|
| 12/08/16 -07/09/16 | FS MARIA S. MERIAN/ MSM57-2 | Spitsbergen Continental Margin | Prof. Dr. Gerhard Bohrmann | Hydroacoustic, IR imaging of sediment cores, sediment core imaging, GIS manager |
| 29/07/16 -12/08/16 | FS MARIA S. MERIAN/ MSM57-1 | Vestnesa Ridge | Prof. Dr. Gerhard Bohrmann | DIS system, hydroacoustic, IR imaging of sediment cores, sediment core imaging, GIS manager |
| 25/08/15 -08/09/15 | FS HEINCKE/ HE450 | Norwegian Sea, Svalbard | Prof. Dr. Gerhard Bohrmann | Water column imaging, seafloor mapping, GIS manager |
| 01/03/15 -28/03/15 | FS METEOR/ M114-2 | Southern Gulf of Mexico | Prof. Dr. Gerhard Bohrmann | TV-Sled survey, water column imaging, ROV dives |
| 12/02/15 -26/02/15 | FS RV METEOR M114-1 | Southern Gulf of Mexico | Dr. Heiko Sahling | TV-Sled survey, water column imaging, AUV dives |

## A2. Co-author papers

# Amount and fate of gas and oil discharged at 3400 m water depth from a natural seep site in the Southern Gulf of Mexico

**Miriam Römer[1*], Chieh-Wei Hsu[1], Markus Loher[1], Ian MacDonald[2], Christian dos Santos Ferreira[1], Thomas Pape[1], Susan Mau[1], Gerhard Bohrmann[1], Heiko Sahling[†]**

[1] MARUM – Center for Marine Environmental Sciences and Department of Geosciences, University of Bremen, Klagenfurter Str.4, DE-28359 Bremen, Germany

[2] Department of Earth, Ocean and Atmospheric Science, Florida State University, Tallahassee, Florida 32306-4320, USA

[†]Deceased April 23, 2018

*** Correspondence:**
Miriam Römer
mroemer@marum.de

**Keywords: Methane seepage, oil release, gas bubbles, Campeche Knolls, Southern Gulf of Mexico**



**Abstract**

This multi-disciplinary study of the hydrocarbon seepage system at Tsanyao Yang Knoll in the southern Gulf of Mexico illustrates the amount and fate of hydrocarbons (mainly oil and methane) emanating from the seafloor structure and rising through a 3400 m water column. Tsanyao Yang Knoll forms part of the Campeche Knolls and was found to be one of the most active seepage structures at such an exceptional depth. Combining ship-based and AUV-based hydroacoustic mapping with direct seafloor observations and investigations, which used a TV-sled and a ROV with gas and water sampling devices provided an integrated view for the various transport pathways of hydrocarbons from the seafloor to the sea surface. In total, 32 acoustic 'flares', indicative of gas bubble emission sites, were detected emanating from depressions on top of the knoll. Most of the emission sites were concentrated in two depressions that comprised a main seep field. An estimated volume of 550–4650 litres of hydrocarbons per hour (or 8300-70 600 mol $CH_4$ per hour) are released in the form of gas bubbles, which dissolve almost entirely during their rise in the water column. However, echograms showed gas anomalies to about 500 meters below sea surface and some bubbles were seen to burst at the sea surface. Concentrations of dissolved methane were highly elevated (~30 000 nmol/L) directly above the seafloor emission site, but decreased to background concentrations (3–5 nmol/L) within the lowermost 100 m. Smaller volume flow rates of oil also escaped from the seafloor, rose to the sea surface and generated natural oil slicks visible from the ship and in satellite images. This study shows that hydrocarbon seepage at ~3400 m water depth can be followed to the sea surface. However, most of the methane dissolves in deeper waters, whereas oil reaches the sea surface.

# Origin and transformation of light hydrocarbons ascending at an active pockmark on Vestnesa Ridge, Arctic Ocean

**T. Pape[1], S. Bünz[2], W.-L. Hong[2,3], M.E. Torres[4], M. Riedel[5], G. Panieri[2], A. Lepland[2,3], C.W. Hsu[1], P. Wintersteller[1], K. Wallmann[5], C. Schmidt[5], H. Yao[2], and G. Bohrmann[1]**

[1]Affiliation for author 1. MARUM – Center for Marine Environmental Sciences and Department of Geosciences, University of Bremen, Germany

[2]Affiliation for author 2. CAGE – Centre for Arctic Gas Hydrate, Environment and Climate, Department of Geosciences, UiT - The Arctic University of Norway, Tromsø, Norway

[3]Affiliation for author 3. now at: Geological Survey of Norway, Trondheim, Norway

[4]Affiliation for author 4. College of Earth Ocean and Atmospheric Sciences, Oregon State University, Corvallis, OR, USA

[5]Affiliation for author 5. GEOMAR – Helmholtz Centre for Ocean Research, Kiel, Germany

Corresponding author: Thomas Pape (tpape@marum.de)

**Key Points:**

- Drilling with the sea floor drill rig MeBo70 revealed two major hydrocarbon sources beneath a pockmark at the crest of Vestnesa Ridge
- Thermogenic methane likely formed at depths >800 m below seafloor ascends through faults and leads to hydrate formation and seafloor emission
- Methane is transformed into dissolved inorganic carbon at all sites investigated with highest rates observed at active seafloor emission sites

This article has been accepted for publication and undergone full peer review but has not been through the copyediting, typesetting, pagination and proofreading process which may lead to differences between this version and the Version of Record. Please cite this article as doi: 10.1029/2018JB016679

nature COMMUNICATIONS

ARTICLE

DOI: 10.1038/s41467-017-02550-9 OPEN

# Gas hydrate dissociation off Svalbard induced by isostatic rebound rather than global warming

Klaus Wallmann[1], M. Riedel[1], W.L. Hong[2,3], H. Patton[3], A. Hubbard[3,4], T. Pape[5], C.W. Hsu[5], C. Schmidt[1], J.E. Johnson[6], M.E. Torres[7], K. Andreassen[3], C. Berndt[1] & G. Bohrmann[5]

Methane seepage from the upper continental slopes of Western Svalbard has previously been attributed to gas hydrate dissociation induced by anthropogenic warming of ambient bottom waters. Here we show that sediment cores drilled off Prins Karls Foreland contain freshwater from dissociating hydrates. However, our modeling indicates that the observed pore water freshening began around 8 ka BP when the rate of isostatic uplift outpaced eustatic sea-level rise. The resultant local shallowing and lowering of hydrostatic pressure forced gas hydrate dissociation and dissolved chloride depletions consistent with our geochemical analysis. Hence, we propose that hydrate dissociation was triggered by postglacial isostatic rebound rather than anthropogenic warming. Furthermore, we show that methane fluxes from dissociating hydrates were considerably smaller than present methane seepage rates implying that gas hydrates were not a major source of methane to the oceans, but rather acted as a dynamic seal, regulating methane release from deep geological reservoirs.

[1] GEOMAR Helmholtz Centre for Ocean Research Kiel, Wischhofstr. 1-3, Kiel 24148, Germany. [2] Geological Survey of Norway, N-7022 Trondheim, Norway. [3] CAGE Centre for Arctic Gas Hydrate Research, Environment and Climate, Department of Geosciences, UiT—The Arctic University of Norway, Tromsø N-9037, Norway. [4] Department of Geography & Earth Science, Aberystwyth University, Wales SY23 3DB, UK. [5] MARUM—Center for Marine Environmental Sciences and Department of Geosciences, University of Bremen, Klagenfurter Str., Bremen 28359, Germany. [6] Department of Earth Sciences, University of New Hampshire, 56 College Rd., Durham, NH 03824-3589, USA. [7] College of Oceanic and Atmospheric Sciences, Oregon State University, 104 Ocean Admin Building, Corvallis, OR 97331-5503, USA. Correspondence and requests for materials should be addressed to K.W. (email: kwallmann@geomar.de)

Contents lists available at ScienceDirect

Deep-Sea Research Part I

journal homepage: www.elsevier.com/locate/dsri

# Formation and preservation of authigenic pyrite in the methane dominated environment

Lan-Feng Fan[a], Saulwood Lin[a,*], Chieh-Wei Hsu[a], Yi-Ting Tseng[a], Tsanyao Frank Yang[b], Kuo-Ming Huang[c]

[a] Institute of Oceanography, National Taiwan University, No. 1, Section 4, Roosevelt Rd., Taipei 106, Taiwan
[b] Department of Geosciences, National Taiwan University, No. 1, Section 4, Roosevelt Road, Taipei 106, Taiwan
[c] Chien-Hsin University of Science and Technology, Taiwan

ARTICLE INFO

*Keywords:*
Pyrite
Methane
Anaerobic methane oxidation
Sulfate reduction
Authigenic mineral

ABSTRACT

Sulfate reduction could go through dissimilatory sulfate reduction and anaerobic methane oxidation couple with sulfate reduction (AOM-SR) with pyrite the end product. While AOM-SR is an important process in oxidizing methane and limiting methane entering the ocean, there is limited information available regarding pyrite formation and preservation under methane dominated environment. The purpose of this study is to report pyrite formation and preservation at a methane dominated environment, the YuanAn Ridge, where methane seeps have been observed, and to evaluate how would that differ from typical anoxic environment. Pore water methane, sulfate, dissolved sulfide, barium, and sediment pyrite, barium/Al ratio and organic carbon in sediments were analyzed from sediments collected by piston cores on board the R/V Ocean Researcher I (OR-I) from the study environment.

The results showed methane flux is controlling pyrite formation in this methane dominated environment. Pyrite concentration is linearly correlated with methane flux with exceptions to shallower sulfate methane transition zone (SMTZ) sites where methane could have vent directly to the overlying water and contribute less to the pyrite formation. The more methane entering the SMTZ, the more pyrite formed and preserved in the sulfate methane transition zone sediments. Authigenic pyrite from dissimilatory sulfate reduction is a small fraction of the pyrite found in the methane dominant and low in organic carbon environment, with majority of pyrite derived from AOM-SR.

Large spatial variations on rate of sulfate reduction, pyrite and methane concentrations were observed in the studied area sediments. Depth of sulfate methane transition zone varied between 1 and 14 m and is a log function of methane flux. Pore water sulfate profiles displayed three different types, linear, concave up and down, indicating methane flux have varied in time.

Pyrite burial efficiency is high, approximately 50% of sulfate entering the SMTZ were preserved in sediments as pyrite. This efficiency of sulfate reduction through AOM-SR is much higher than pyrite formation from dissimilatory sulfate reduction in normal marine sediments. The AOM-SR and pyrite formation occurred at depth within the SMTZ favor a higher degree of pyrite preservation. Time require for the pyrite formation is about 4400 years in the YAR sediments, based on diffusion model calculation of barium sulfate precipitation.

## 1. Introduction

Organic matter oxidation through sulfate reduction and methane oxidation through anaerobic methane oxidation are two of the most important diagenetic processes involving carbon and sulfur cycle. The top-down rain rates of organic matter settling on the sea floor control rates of sulfate reduction and subsequently the pyrite formation in sediments. Formation of pyrite is therefore, usually, directly controlled by dissimilatory sulfate reduction in marine sediments. Pyrite could also be produced as a major end product during anaerobic methane oxidation coupled with sulfate reduction (AOM-SR) (Borowski et al., 2013; Peckmann and Thiel, 2004). Similar to dissimilatory sulfate reduction in typical normal marine sediment, dissolved sulfide from AOM-SR could react with iron oxide in sediments in forming pyrite. This bottom-up migration of methane over pyrite formation may differ from that of the top-down organic matter dissimilatory sulfate reduction pyrite.

* Corresponding author.
*E-mail address:* swlin@ntu.edu.tw (S. Lin).

https://doi.org/10.1016/j.dsr.2018.07.004
Received 15 March 2018; Received in revised form 30 June 2018; Accepted 3 July 2018

SCIENTIFIC REPORTS

OPEN

Received: 17 June 2016
Accepted: 17 January 2017
Published: 23 February 2017

# Widespread methane seepage along the continental margin off Svalbard - from Bjørnøya to Kongsfjorden

S. Mau[1], M. Römer[1], M. E. Torres[2], I. Bussmann[3], T. Pape[1], E. Damm[3], P. Geprägs[1], P. Wintersteller[1], C.-W. Hsu[1], M. Loher[1] & G. Bohrmann[1]

**Numerous articles have recently reported on gas seepage offshore Svalbard, because the gas emission from these Arctic sediments was thought to result from gas hydrate dissociation, possibly triggered by anthropogenic ocean warming. We report on findings of a much broader seepage area, extending from 74° to 79°, where more than a thousand gas discharge sites were imaged as acoustic flares. The gas discharge occurs in water depths at and shallower than the upper edge of the gas hydrate stability zone and generates a dissolved methane plume that is hundreds of kilometer in length. Data collected in the summer of 2015 revealed that 0.02–7.7% of the dissolved methane was aerobically oxidized by microbes and a minor fraction (0.07%) was transferred to the atmosphere during periods of low wind speeds. Most flares were detected in the vicinity of the Hornsund Fracture Zone, leading us to postulate that the gas ascends along this fracture zone. The methane discharges on bathymetric highs characterized by sonic hard grounds, whereas glaciomarine and Holocene sediments in the troughs apparently limit seepage. The large scale seepage reported here is not caused by anthropogenic warming.**

Methane is, after water vapor and $CO_2$, the most abundant greenhouse gas on Earth. When averaged over a 100 yr timescale, the warming effect of methane per unit mass is 28 times higher than that of $CO_2$[1]. Methane is produced in oceanic sediments either by methanogens at temperatures typically below ~80 °C, or through the breakdown of organic molecules at higher temperatures[2,3]. Buoyancy and pressure gradients can drive gas advection to shallower sediments where methane can be consumed via anaerobic oxidation of methane (AOM)[4] at the sulfate-methane transition zone and aerobic methane oxidation at the sediment surface[5]. Methane can also be sequestered within a cage of water molecules, in a gas hydrate structure, stable under the low temperature and high pressure conditions that define the gas hydrate stability zone[6].

If the upward methane flux is not fully exhausted by these processes, methane is emitted to the ocean either dissolved in the venting fluids or, in case of over-saturation, as gas bubbles[7]. As the bubbles ascend through the water column, a fraction of the methane gas dissolves[8], generating patches of high methane concentration[9]. When the gas discharge is persistent and vigorous, it leads to the formation of large dissolved methane plumes. The dissolved methane is diluted by mixing with the surrounding ocean water and it is further oxidized by aerobic methanotrophs. Only in cases where dissolved methane reaches the surface-mixed layer in concentrations above saturation, can it be transferred to the atmosphere via sea-air gas exchange[10]. At present, the oceanic methane source to the atmosphere is very small (2–10%)[11], as it is limited to emissions from vigorous and shallow seeps (<100 m)[1,7,8]. There is, however, an ongoing controversy regarding the methane discharge from sediments during warming events throughout Earth's history[12,13], as a temperature increase could potentially destabilize gas hydrates and liberate vast quantities of methane. Such a mechanism has been proposed to explain the seepage observed offshore Svalbard[14].

[1]MARUM – Center for Marine Environmental Sciences and Department of Geosciences, University of Bremen, Klagenfurter Str., 28359 Bremen, Germany. [2]College of Oceanic and Atmospheric Sciences, Oregon State University, 104 Ocean Admin Building, Corvallis, Oregon 97331–5503, USA. [3]Alfred Wegener Institute Helmholtz Centre for Polar and Marine Research, Am Handelshafen 12, 27570 Bremerhaven, Germany. Correspondence and requests for materials should be addressed to S.M. (email: smau@marum.de)

Biogeosciences, 13, 4491–4512, 2016
www.biogeosciences.net/13/4491/2016/
doi:10.5194/bg-13-4491-2016


Biogeosciences Open Access EGU

# Massive asphalt deposits, oil seepage, and gas venting support abundant chemosynthetic communities at the Campeche Knolls, southern Gulf of Mexico

**Heiko Sahling[1,2], Christian Borowski[2,3], Elva Escobar-Briones[4], Adriana Gaytán-Caballero[4], Chieh-Wei Hsu[1], Markus Loher[2], Ian MacDonald[5], Yann Marcon[6], Thomas Pape[1,2], Miriam Römer[1,2], Maxim Rubin-Blum[3], Florence Schubotz[2], Daniel Smrzka[7], Gunter Wegener[2,3], and Gerhard Bohrmann[1,2]**

[1]Department of Geosciences at the University of Bremen, Klagenfurter Str., 28359 Bremen, Germany
[2]MARUM Center for Marine Environmental Sciences, Leobener Str., 28359 Bremen, Germany
[3]Max-Planck Institute for Marine Microbiology, Celsiusstr. 1, 28359 Bremen, Germany
[4]Universidad Nacional Autónoma de México, Instituto de Ciencias del Mar y Limnología, A. P. 70-305 Ciudad Universitaria, 04510 Mexico City, México
[5]Florida State University, P.O. Box 3064326, Tallahassee, FL 32306, USA
[6]Alfred Wegener Institute Helmholz Centre for Polar and Marine Research, HGF-MPG Group for Deep Sea Ecology and Technology, Am Handelshafen 12, 27570 Bremerhaven, Germany
[7]Center for Earth Sciences, University of Vienna, Althanstr. 14, 1090 Vienna, Austria

*Correspondence to:* Heiko Sahling (hsahling@marum.de)

Received: 17 March 2016 – Published in Biogeosciences Discuss.: 24 March 2016
Revised: 29 June 2016 – Accepted: 19 July 2016 – Published: 11 August 2016

**Abstract.** Hydrocarbon seepage is a widespread process at the continental margins of the Gulf of Mexico. We used a multidisciplinary approach, including multibeam mapping and visual seafloor observations with different underwater vehicles to study the extent and character of complex hydrocarbon seepage in the Bay of Campeche, southern Gulf of Mexico. Our observations showed that seafloor asphalt deposits previously only known from the Chapopote Knoll also occur at numerous other knolls and ridges in water depths from 1230 to 3150 m. In particular the deeper sites (Chapopopte and Mictlan knolls) were characterized by asphalt deposits accompanied by extrusion of liquid oil in form of whips or sheets, and in some places (Tsanyao Yang, Mictlan, and Chapopote knolls) by gas emission and the presence of gas hydrates in addition. Molecular and stable carbon isotopic compositions of gaseous hydrocarbons suggest their primarily thermogenic origin. Relatively fresh asphalt structures were settled by chemosynthetic communities including bacterial mats and vestimentiferan tube worms, whereas older flows appeared largely inert and devoid of corals and anemones at the deep sites. The gas hydrates at Tsanyao Yang and Mictlan Knolls were covered by a 5-to-10 cm-thick reaction zone composed of authigenic carbonates, detritus, and microbial mats, and were densely colonized by 1–2 m-long tube worms, bivalves, snails, and shrimps. This study increased knowledge on the occurrences and dimensions of asphalt fields and associated gas hydrates at the Campeche Knolls. The extent of all discovered seepage structure areas indicates that emission of complex hydrocarbons is a widespread, thus important feature of the southern Gulf of Mexico.

## 1 Introduction

Asphalt volcanism in the Campeche Knolls, southern Gulf of Mexico (GoM) has been described as a distinct form of natural hydrocarbon seepage (MacDonald et al., 2004). Heavy oil is extruded and forms lava-like flows that cover $\sim 100$ to $\sim 1000\,m^2$ of abyssal knolls and ridges (Brüning et al., 2010). The flows consist of high-density oil with an abundant asphaltene fraction (MacDonald et al., 2004) with a terpane composition similar to what has been reported from some crude oils in the Bay of Campeche (Scholz-Böttcher

**Published by Copernicus Publications on behalf of the European Geosciences Union.**

## Versicherung an Eides Statt / *Affirmation in lieu of an oath*

**gem. § 5 Abs. 5 der Promotionsordnung vom 18.06.2018 /**
***according to § 5 (5) of the Doctoral Degree Rules and Regulations of 18 June, 2018***

Ich / I, Chieh-Wei, Hsu/ Stuhrer Str. 47, 28197 Bremen/ 3026325
(Vorname / First *Name*, Name / *Name*, Anschrift / *Address*, ggf. Matr.-Nr. / *student ID no., if applicable)*

versichere an Eides Statt durch meine Unterschrift, dass ich die vorliegende Dissertation selbständig und ohne fremde Hilfe angefertigt und alle Stellen, die ich wörtlich dem Sinne nach aus Veröffentlichungen entnommen habe, als solche kenntlich gemacht habe, mich auch keiner anderen als der angegebenen Literatur oder sonstiger Hilfsmittel bedient habe und die zu Prüfungszwecken beigelegte elektronische Version (PDF) der Dissertation mit der abgegebenen gedruckten Version identisch ist. / *With my signature I affirm in lieu of an oath that I prepared the submitted dissertation independently and without illicit assistance from third parties, that I appropriately referenced any text or content from other sources, that I used only literature and resources listed in the dissertation, and that the electronic (PDF) and printed versions of the dissertation are identical.*

Ich versichere an Eides Statt, dass ich die vorgenannten Angaben nach bestem Wissen und Gewissen gemacht habe und dass die Angaben der Wahrheit entsprechen und ich nichts verschwiegen habe. / *I affirm in lieu of an oath that the information provided herein to the best of my knowledge is true and complete.*

Die Strafbarkeit einer falschen eidesstattlichen Versicherung ist mir bekannt, namentlich die Strafandrohung gemäß § 156 StGB bis zu drei Jahren Freiheitsstrafe oder Geldstrafe bei vorsätzlicher Begehung der Tat bzw. gemäß § 161 Abs. 1 StGB bis zu einem Jahr Freiheitsstrafe oder Geldstrafe bei fahrlässiger Begehung. / *I am aware that a false affidavit is a criminal offence which is punishable by law in accordance with § 156 of the German Criminal Code (StGB) with up to three years imprisonment or a fine in case of intention, or in accordance with § 161 (1) of the German Criminal Code with up to one year imprisonment or a fine in case of negligence.*

Breme. 16.03.2020. Chieh-Wei Hsu

Ort / *Place*, Datum / *Date* — Unterschrift / *Signature*